

# **Thermal Analysis of a Vaporization Source for Inorganic Coatings**

Brian Vincent Nutter

Thesis submitted to the Faculty of the  
Virginia Polytechnic Institute and State University  
in partial fulfillment of the requirements for the degree of

MASTER OF SCIENCE

in

Mechanical Engineering

Dr. Brian Vick, Chair

Dr. Thomas E. Diller

Dr. Douglas J. Nelson

8 December 2000

Blacksburg, Virginia

**Key words:** Numerical Methods, Coatings, Heat Transfer Analysis,  
Interface Conductivity

Copyright 2000, Brian Vincent Nutter

# **Thermal Analysis of a Vaporization Source for Inorganic Coatings**

by

Brian Vincent Nutter

Dr. Brian Vick, Chair

Mechanical Engineering

## **(ABSTRACT)**

A thermal analysis of a conventional vaporization source by finite difference methods, including experimental validation, is presented. Such a system is common to industries whose chief concern is the precipitation of inorganic coatings. Both the physical and the model systems are comprised of a number of layers, or strata, arranged in a rectangular configuration. The model strata represent the component and deposition materials of the physical vaporization source. The symmetry and simplistic geometry of the operational source permit the use of a two-dimensional model, thereby neglecting gradients in the third dimension. The production unit, as well as the numerical model, experience various modes of heat transfer, including radiation, convection, conduction, internal generation, and phase change. Moreover, the system inputs are time-dependent.

The numerical model is subsequently compared to and validated against both simplistic case studies and the physical production system. Data collected from the operational deposition source is examined and analyzed in comparison to corresponding information generated by the numerical model. Sufficient agreement between the data sets encourages the utilization of the numerical model as a practical indicator of the subject system's behavior.

Finally, recommendations for modifications to the physical vaporization source, yielding practical improvements in temperature uniformity, are evaluated based on the predictions of the validated numerical model. The goal is the attainment of an ideally uniform temperature distribution that would correspond to highly desirable performance of the process vaporization system.

# Acknowledgments

As I begin, I wish to thank the members of my advisory committee: Dr. Douglas Nelson, Dr. Thomas Diller, and Dr. Brian Vick. I express my sincere appreciation to Dr. Vick for his patience, guidance, interest, and friendship throughout the completion of this work. I have thoroughly enjoyed the opportunity to work closely with such an insightful educator and engineer.

I offer my appreciation to my employer, unnamed to maintain confidentiality, who afforded both the foundation and the opportunity to conduct this research. In addition, I wish to thank the many colleagues who have toiled in the practical development of the equipment on which this study is based.

I extend my earnest thanks to my parents, C.J. and Doris, for their hard work, sacrifices, and perseverance in affording the opportunities to obtain my undergraduate and graduate degrees. I am forever indebted to them for their love, guidance, support, generosity, and kindness throughout the course of my life. I cherish my mother and father as both parents and friends.

I wish to thank my parents-in-law, Carolyn and Bobby Rakes, for their love, encouragement, and support during my graduate endeavors. Their friendship and faith have bolstered my resolve and refreshed my perspectives. I am most thankful to have such a wonderful family.

I thank my brother, Brandon, for the countless deeds of fraternity and friendship he has gladly offered to facilitate the pursuit of this goal in my life. From loaning computer hardware to late night motherboard replacements, his support has been unwavering. Brandon's faith and confidence in my abilities are most flattering. I am fortunate to count such a talented engineer as my brother, my colleague, and my friend.

Finally, I wish to extend my heartfelt gratitude to the woman who fulfilled my dreams of happiness. Throughout my graduate research, my wife, Leslie, has given endlessly of herself to perpetuate my success. Advocating computer upgrades, proofreading until 5 a.m., pushing me when I needed a boost, Leslie has been in the trenches ensuring that the dirty work is accomplished and that the details are impeccable. Her amazing patience, infallible confidence in me, and immeasurable love have given me every opportunity to succeed. For these, and the many other gifts she offers unselfishly, I am forever grateful. I look forward to a lifetime of joy spent with Leslie.

Thank each of you for your many and significant contributions to this work.

# Table of Contents

<b>Chapter 1.0</b>	<b>Introduction.....</b>	<b>1</b>
1.1	Motivation.....	1
1.2	Objectives .....	2
<b>Chapter 2.0</b>	<b>Background .....</b>	<b>4</b>
2.1	Thin Film Technology .....	4
2.2	Vacuum Coating Processes .....	7
2.2.1	<i>Sputtering</i> .....	7
2.2.2	<i>Low-Pressure Chemical Vapor Deposition</i> .....	8
2.2.3	<i>Physical Vapor Deposition</i> .....	10
2.2.4	<i>Metallizing</i> .....	10
2.2.5	<i>Technology of Interest: Conventional Evaporation</i> .....	12
2.2.6	<i>Electron Beam Evaporation</i> .....	13
2.2.7	<i>Reactive Evaporation</i> .....	14
2.3	Heat Transfer Phenomena.....	15
2.3.1	<i>Conductive Heat Transfer</i> .....	16
2.3.2	<i>Convective Heat Transfer</i> .....	16
2.3.3	<i>Radiative Heat Transfer</i> .....	17
2.3.4	<i>Internal Heat Generation</i> .....	18
2.3.5	<i>Evaporative Heat Transfer</i> .....	19
2.4	Numerical Methods .....	20
2.4.1	<i>Boundary Element Method</i> .....	20
2.4.2	<i>Finite Element Method</i> .....	21
2.4.3	<i>Finite Difference Method</i> .....	21
<b>Chapter 3.0</b>	<b>Physical System .....</b>	<b>24</b>
3.1	Description of Physical System.....	25
3.1.1	<i>Vacuum System</i> .....	25

3.1.2	<i>Transport System</i> .....	26
3.1.3	<i>Deposition System</i> .....	27
3.1.4	<i>System Operation</i> .....	31
3.2	<b>Relevant Physical Data</b> .....	32
3.2.1	<i>Physical Geometry</i> .....	33
3.2.2	<i>Material Properties</i> .....	34
3.2.3	<i>Heat Source, Vaporization Vessel, and Refractory Properties</i> .....	35
3.2.4	<i>Evaporant Properties</i> .....	35
3.2.5	<i>Calorimetric Differential Thermal Analysis</i> .....	38
3.2.6	<i>Operation of Differential Thermal Analyzer</i> .....	39
3.2.7	<i>Operations Data</i> .....	40
	<b>Chapter 4.0 Modeling of Physical System</b> .....	<b>44</b>
4.1	<b>Relevant Physics</b> .....	44
4.1.1	<i>Electrical Power Input</i> .....	45
4.1.2	<i>Radiative Phenomena</i> .....	47
4.1.3	<i>Convection Heat Loss</i> .....	50
4.1.4	<i>Evaporative Heat Loss</i> .....	52
4.2	<b>Modeling of Physical System</b> .....	54
4.2.1	<i>Symmetry</i> .....	54
4.2.2	<i>Internal Radiation</i> .....	55
4.2.3	<i>External Radiation</i> .....	58
4.2.4	<i>Lumping in z-Direction</i> .....	59
4.2.5	<i>Treatment of Voided Regions</i> .....	61
4.2.6	<i>Treatment of Evaporative Contribution</i> .....	62
	<b>Chapter 5.0 Numerical Solution</b> .....	<b>65</b>
5.1	<b>Formulation of Governing Equation</b> .....	65
5.1.1	<i>The Energy Equation</i> .....	65
5.1.2	<i>Formulation of the Source Term</i> .....	66
5.2	<b>Discretization of Governing Equations</b> .....	70

5.2.1	<i>Time Discretization</i> .....	70
5.2.2	<i>Spatial Discretization</i> .....	71
5.2.3	<i>Development of the Discretized Governing Equation</i> .....	75
5.3	<b>Implementation of Numerical Solution</b> .....	81
5.3.1	<i>Evaluation of Inputs</i> .....	82
5.3.2	<i>Iterative Solution</i> .....	86
5.3.3	<i>Marching Through Time</i> .....	87
<b>Chapter 6.0 Simulation Results .....</b>		<b>90</b>
6.1	<b>Validation of Solution</b> .....	90
6.1.1	<i>Grid Refinement</i> .....	90
6.1.2	<i>Convergence Criteria Refinement</i> .....	96
6.1.3	<i>Time Dependence of Model Stability</i> .....	98
6.1.4	<i>Case Studies</i> .....	100
6.1.5	<i>Experimental Validation</i> .....	106
6.1.6	<i>Summary: Validity of the Numerical Solution</i> .....	114
6.2	<b>Simulation of Proposed Improvements</b> .....	118
6.2.1	<i>Method of Comparison</i> .....	118
6.2.2	<i>Unsatisfactory Proposed Improvements</i> .....	120
6.2.3	<i>Satisfactory Proposed Improvements</i> .....	123
6.2.4	<i>Summary: Evaluation of Proposed Improvements</i> .....	127
<b>Chapter 7.0 Conclusions and Recommendations .....</b>		<b>129</b>
7.1	<b>Conclusions</b> .....	129
7.2	<b>Recommendations</b> .....	131
<b>References .....</b>		<b>133</b>
<b>Appendix A Material Property Tables .....</b>		<b>138</b>
<b>Appendix B DTA Data.....</b>		<b>141</b>

<b>Appendix C</b>	<b>Effective Convection Coefficient.....</b>	<b>146</b>
<b>Appendix D</b>	<b>Lumping in z-Direction.....</b>	<b>149</b>
<b>Appendix E</b>	<b>Discretization of Governing Equation.....</b>	<b>152</b>
<b>Appendix F</b>	<b>Table of Discretized Boundary Conditions .....</b>	<b>160</b>
<b>Appendix G</b>	<b>Derivation of the Stability Criteria.....</b>	<b>163</b>
<b>Appendix H</b>	<b>Mathematica<sup>â</sup> Code .....</b>	<b>168</b>
<b>Appendix I</b>	<b>Mean and 16X Grid Density Responses .....</b>	<b>211</b>
<b>Vita</b>	<b>.....</b>	<b>213</b>

# List of Figures

Figure 2.1	Schematic of Sputtering Deposition	8
Figure 2.2	Schematic of LPCVD reactor	9
Figure 2.3	Common Vacuum Metallizer for Aluminum	11
Figure 2.4	Conventional Box Evaporation Source	13
Figure 3.1	Schematic of a Vacuum Chamber for Evaporative Web Coating	26
Figure 3.2	Conventional Box Evaporation Source, Cross-Section	27
Figure 3.3	Cutaway View of a Conventional Box Vaporization Source	28
Figure 3.4	Major Axial Section of a Conventional Box Evaporation Apparatus	31
Figure 3.5	Physical Vapor Deposition from a Conventional Evaporation Source	32
Figure 3.6	Temperature Dependence of Material Properties	36
Figure 3.7	Schematic of a Boersma-Type Calorimetric DTA System	38
Figure 3.8	Source Thermocouple Locations	41
Figure 3.9	Typical Heat Source Input and Transient Response	43
Figure 4.1	General Schematic Representation of Model Physics	45
Figure 4.2	Typical Stepped Power Input	46
Figure 4.3	Sites Experiencing Internal Radiation Transfer	47
Figure 4.4	Upper Heat Source-Evaporant Interface	48
Figure 4.5	Lower Heat Source-Vessel Interface	48
Figure 4.6	Radiative Boundary Condition	49
Figure 4.7	Convective Boundaries and Lumped Contribution	50
Figure 4.8	Schematic of Entire System Prior to Invoking Symmetry	54
Figure 4.9	Application of Symmetry to Full System	55
Figure 4.10	Schematic of Columnar Internal Radiation	56
Figure 4.11	Equivalent Resistance Network, Lumping in z-Direction	60

Figure 4.12	Schematic illustrating latent and sensible heat	63
Figure 5.1	Practice A Discretization (Courtesy Vick, 2000)	72
Figure 5.2	Practice B Discretization (Courtesy Vick, 2000)	73
Figure 5.3	Zoned Domain Construction (adapted from Vick, 2000)	74
Figure 5.4	Typical Zoning Scheme	75
Figure 5.5	Interior 2-D Control Volume, Practice B (Courtesy Vick, 2000)	76
Figure 5.6	Thermal Resistance Network for Interface Conductivity (Courtesy Vick, 2000)	78
Figure 5.7	Schematic of Internal Radiation Node—Stability Development	85
Figure 5.8	Simplified Flow Chart of Numerical Solution	89
Figure 6.1	Grid Refinement, Transient Response	92
Figure 6.2	Grid Refinement, Axial Temperature Distribution	93
Figure 6.3	Convergence Criteria, Transient Response	97
Figure 6.4	Convergence Criteria, Axial Temperature Distribution	97
Figure 6.5	Time-Step Dependence of Stability	98
Figure 6.6	Case Studies: Transient Response, Center Position	102
Figure 6.7	Case Studies: Axial Temperature Distribution, 2000 seconds	104
Figure 6.8	Spatial Temperature Distribution, Case Study 3.0.1	105
Figure 6.9	Contour Plot of Evaporant Depletion, Case Study 3.0.1	106
Figure 6.10	Numerical Simulation of Data Set I Transient Response, Center	108
Figure 6.11	Axial Temperature Distribution, Data Set I, 8000 seconds	109
Figure 6.12	Spatial Temperature Distribution, Data Set I, 8000 seconds	110
Figure 6.13	Numerical Simulation of Data Set II Transient Response, Center	112
Figure 6.14	Axial Temperature Distribution, Data Set II, 8000 seconds	113
Figure 6.15	Spatial Temperature Distribution, Data Set II, 8000 seconds	113
Figure 6.16	Unsatisfactory Proposed Improvements	121
Figure 6.17	Satisfactory Proposed Improvements	124
Figure 6.18	Spatial Temperature Distribution: Satisfactory Improvements	126

Figure B1	DTA: Energy Absorbed by Sample	144
Figure B2	MathCAD Plot of Evaporant Heat Capacity	145
Figure D4.11	Equivalent Network Resistances, Lumping in the z-Direction	150
Figure G5.7	Schematic of Internal Radiation Node	164
Figure H5.8	Simplified Flow Chart of Numerical Solution	169
Figure I1	Mean and 16X Grid Density Transient Responses	212

# List of Tables

Table 6.1	Grid Refinement Schedule, Simulated Time = 1680s	91
Table 6.2	Deviations Among Subsequent Grid Densities	95
Table 6.3	Case Studies for Model Validation	100
Table A1	Heater Property Data	139
Table A2	Insulation Property Data	140

# Nomenclature

Symbol	Description	Units
$A$	area	$m^2$
$a$	implicit source and transient term	$W/K$
$aE$	eastern conductance	$W/K$
$aN$	northern conductance	$W/K$
$aO$	capacity coefficient	$W/K$
$aS$	southern conductance	$W/K$
$aW$	western conductance	$W/K$
$b$	explicit source and transient term	$W$
$C$	specific heat capacity	$J/kgK$
$d$	deviation	$^{\circ}C$
$F$	view factor	
$f$	Moody friction factor	
$h$	convection coefficient	$W / m^2 K$
$h$	heat of vaporization / sublimation	$J/kg$
$i$	electrical current	$A$
$k$	thermal conductivity	$W/mK$
$L$	length or characteristic length	$m$
$m$	mass	$kg$
$\dot{m}$	mass flow rate, fluid conduit	$kg/s$
$n$	mass flow rate, evaporation	$kg/s$
$Nu$	Nusselt number	
$p$	electrical power	$W$
$P$	perimeter	$m$
$Pr$	Prandtl Number	
$q$	heat rate	$W$
$R$	resistance, electrical or equivalent	$W \text{ or } K/W$
$Re$	Reynold's Number	

$S$	volumetric source term	$W / m^3$
$Sc$	constant part of source term	$W / m^3$
$Sp$	proportional part of source term	$W / m^3$
$T$	temperature	$^{\circ}C$
$t$	time	$s$
$u$	velocity	$m/s$
$\forall$	volume	$m^3$
$x$	axial or horizontal direction	$m$
$y$	vertical direction	$m$
$z$	lateral direction	$m$

### ***Greek Symbols***

Symbol	Description	Units
$D$	differential or change	
$K$	conductance in stability equation	$W/K$
$e$	emissivity	
$\mu$	dynamic viscosity	$N \cdot s / m^2$
$\rho$	density	$kg / m^3$
$\sigma$	Stefan-Boltzmann constant	$W / m^2 K^4$
$s$	standard deviation	$^{\circ}C$
$\nu$	kinematic viscosity	$m^2 / s$

### ***Superscripts***

Symbol	Description
$\wedge$	vector quantity
$\llcorner$	flux
$*$	previous iteration
$\bar{\quad}$	averaged

### ***Subscripts***

Symbol	Description
$\infty$	free stream
$12$	from 1 to 2
$conv$	convection, convective
$cs$	cross-sectional
$E$	east, eastern
$eff$	effective
$ELEC$	electric
$elec$	electric
$evap$	evaporation, evaporative
$fg$	fluid to gas
$h$	hydraulic (diameter)
$i$	initial condition
$i$	x-direction index
$IN$	into the system
$in$	into the system
$INSULATION$	of the insulation
$internal$	internal
$j$	y-direction index
$lower$	of the lower heat source
$lumped$	of the lumped contribution
$m$	mean , free-stream
$mean$	mean, free stream
$N$	north, northern
$OUT$	out of the system
$p$	current integer time value
$r$	radiation
$rad$	radiation, radiative
$S$	south, southern
$SIDES$	of the lateral part of lower source

<i>stable</i>	stable condition
<i>surr</i>	surrounding
<i>upper</i>	of the upper heat source
<i>VESSEL</i>	of the vessel
<i>VOID</i>	of the voids
<i>w</i>	wetted
<i>W</i>	west, western
<i>WATER</i>	of the water

# Chapter 1.0

## Introduction

### 1.1 Motivation

As one might expect, a compelling impetus must provide the foundation for any endeavor having the breadth and duration entailed herein. Such is also the case with this investigation. Specifically, a converter of polymer sheet has enlisted the assistance of the academic community to resolve an analytical quandary concerning the operation of a processing machine. The author, being a member of the interested company's employ, was selected to conduct this study to accomplish the Company's project goal of process improvement while obtaining his Master of Science degree.

The interested firm expects to accentuate the performance, and thus the marketability and reputation, of a profitable film product by enhancing its quality. Specifically, the family of consumers for this brand of film demands a certain degree of consistency throughout the merchandise. For the applications in which this product is used, optical-quality clarity and uniformity of the applied coating are critical. To affect such an improvement, gradients in coating thickness must be diminished. Consequently, this requires an inherent enhancement in the uniformity of the source temperature distribution, as this property correlates strongly with coating uniformity. As the system is situated such that it may continuously deposit a coating spanning the width of the feeding substrate, the consistency at issue is in the cross-sheet direction, (orthogonal to the direction of film travel).

Currently, attainment of the minimum uniformity requirement is within the capabilities of the production vaporization system. However, as public regard for the product line increases, so too does consumer expectation of increased quality. Moreover, if the consistency of the coated polymer substrate may be sustained at yet a higher degree

of uniformity, new, higher margin markets for this product suddenly become feasible. The film may be used in applications far more conspicuous than those currently targeted. Herein lies the motivation for this investigation.

The vaporization system is highly sensitive to irregularities in temperature distribution. Since the major axis of the vaporization source corresponds to the cross-web direction of the substrate, uniformity along the length of the source is crucial. Gradients of a minor scale produce significant variances in product consistency. Coating thickness and uniformity are directly coupled with source temperature. Therefore, to ameliorate the performance of the production vaporization source, and enhance the quality of the consumer's product, this examination aims to model, predict, and improve the thermal behavior of the subject vaporization source.

## **1.2 Objectives**

Three objectives comprise the focus of this work. Primarily, this investigation aims to derive and develop a numerical model of the transient thermal behavior of a general box vaporization source utilized in thin film deposition. The model will comprise a two-dimensional, rectangular, composite thermal system having time- and temperature-dependent inputs and properties.

Secondly, the behavior of the resulting numerical model will be examined in comparison to both simplified case studies of known phenomena and experimental data acquired from the physical vaporization source. This validation phase comprises a qualitative comparison of numerical results to expected behavior and a qualitative and quantitative comparison of numerical results to experimental data.

Third, having verified the operation of the model qualitatively against known case studies, and quantitatively using data collected from the production vaporization source, hypothetical permutations of run conditions will be simulated using the numerical model. The results yielded by these simulations will be utilized to evaluate and select proposed design enhancements effecting temperature distribution and uniformity. The most favorable results obtained in this phase will be selected as the recommended design improvements to the existing physical system.

# Chapter 2.0

## Background

### 2.1 Thin Film Technology

The development and utilization of inorganic coatings has borne countless processes and technologies. Various methods, ranging from liquid applications to ion beam deposition, have been successfully employed in the precipitation of inorganic thin film coatings on a myriad of substrates.

For instance, rotogravure-coating processes are employed extensively in both the flexographic printing and polymer film conversion industries for the application of inks and dyes, and protective and adhesive coatings. The familiar process of screen-printing, used often in the garment industry, is considered a film coating process, although, in terms of deposition thickness, it is more substantial than its thin film brethren (Kern & Schuegraf, 1988).

Industrial film coating processes include electroplating, electroless plating, and mechanical methods of film precipitation. Electroplating is often employed in the deposition of metals such as gold, silver, copper, chromium, nickel, and zinc. Electroless plating is dominantly used to produce coatings of nickel, nickel alloys, and copper. Mechanical techniques, such as plasma spraying, flame spraying, and electric arc spraying, are utilized to generate thin metal coatings by pyrolytic reaction and deposition (Kern & Schuegraf, 1988).

Decorative coatings, such as those found on plastic toys, automotive interior trim, and trophies, are likely the most readily visible use of vacuum deposited thin films. Often, the mirror-like finish of these items is produced by the vacuum evaporation of aluminum, a process commonly recognized as metallizing (Stuart, 1983).

Wear-resistant and solid-lubricant coatings have gained much popularity and utility in many industrial, commercial, and scientific settings. A wear-surface may be coated with a wear-resistant film, such as tungsten carbide, while a solid lubricant, such as molybdenum disulfide, lubricates the mating surface of its complementary part (Stuart, 1983). Coatings of this genre are generally chemically deposited (Powell, 1966).

Despite the numerous and diverse uses for other thin film products and processes, two relatively new applications boast the distinction of inspiring significant technological development in thin film coating techniques. Rapid growth in both the optics and electronics industries has perpetuated remarkable advancement in the technology of thin film deposition (Schuegraf, 1988).

A substantial portion of the tremendous growth in thin film applications and processes may be aptly attributed to the explosive development of microelectronics and the incorporation of such coating technologies therein. Consequently, an obvious indicator of the financial impact and global importance of thin film technologies is the multi-billion dollar semiconductor industry (Schuegraf, 1988).

Specifically, integrated circuits, magnetic devices, and numerous semi-conductors are manufactured using thin film deposition techniques (Stuart, 1983). Moreover, recording and storage media, as well as electronics accessories and packaging are fabricated using thin-film techniques. Antistatic packaging, magnetic storage and recording media, compact discs (CD's), and CD-ROMS have a common thin-film heritage (Kern & Schuegraf, 1988).

Electronic components are often utilized within more consumer-recognizable electronic devices that are coated by thin-film methods. Electronic displays, such as liquid-crystal displays (LCD's), light-emitting diodes (LED's), electroluminescent displays, plasma and fluorescent displays, and electrochromic displays, comprise some of the more prevalent configurations. Production of these devices may entail the deposition of numerous thin-film layers of varied properties and composition. Conductive, dielectric,

fluorescent, and transparent coatings are just a few of the many possibilities (Kern & Schuegraf, 1988).

In much the same fashion as the electronics industry, growth in the applications of optics and the optical industry spurs the development of thin-film coatings. Optical component and equipment manufacturers utilize various coating technologies in the production of their assorted wares.

For instance, antireflection coatings, primarily inorganic deposits, found on eyeglass lenses, binocular components, microscope components, and computer monitors, for example, are commonplace (Stuart, 1983). Such deposits improve product performance by reducing glare and unwanted reflection, a desirable effect in the optics industry. Optical coatings are employed in the production of interference filters for solar panels, infrared solar reflectors, and laser optics. Various processes, resulting in film constructions which affect the control or manipulation of light energy, are applied to achieve the desired effects of light filtering, increased luminous flux intensity, and radiation-resistant reflectivity, respectively (Kern & Schuegraf, 1988).

Obviously, the processes of thin-film deposition have become integral to the high-technology industries of electronics and optics. The importance of these methodologies is evidenced in the economic vastness of these industries. The sheer utility of electronic devices, the promise of optical data storage, the power and efficiency of optical fibers, the evolution of lasers, and the necessity to manipulate and optimize solar energy, render thin-film coating techniques paramount to the progression of many areas of technological advancement.

A great number of the thin-film depositions employed within electronic and optical functions are created using vacuum coating processes. As the basis of this investigation lies within the realm of coatings characterized as vacuum depositions, a closer examination of applications and processes implicit to the domain of vacuum coatings is pertinent.

## 2.2 Vacuum Coating Processes

The classification of vacuum coatings contains many unique deposition techniques and technologies. A number of more common examples include sputtering, low-pressure chemical vapor deposition (LPCVD), and physical vapor deposition (PVD).

### 2.2.1 Sputtering

One prevalent film deposition process is that of sputtering. Stuart gives a vivid definition of the physics of sputtering. “If a solid or liquid at any temperature is subjected to bombardment by suitably high energy atomic particles (usually ions), it is possible for individual atoms to acquire enough energy via collision processes to escape from the surface” (Stuart, 1983, p. 91).

In that, any manner of surface impingement resulting in atomic ejection, and usually, subsequent deposition may be considered a form of sputtering. In order to be effective, incident particles must be of atomic scale. Larger particles will not interact with surface atoms, whereas smaller particles, such as electrons, lack the mass to acquire sufficient momentum to be of use. Therefore, ions, primarily from noble gases, are employed as sputtering “bullets” to eject atoms from the target surface (Chapman & Mangano, 1988). This process is likewise conducted within a vacuum environment, often in a planar or cylindrical magnetron configuration. Wherein, ions of a sputtering gas are excited within a plasma, a gaseous conductor likened to the glow discharge of fluorescent light tubes and neon signs (Konuma, 1992). This plasma environment is created in the immediate vicinity of the deposition source material by a high voltage applied to the magnetron supporting the “target” (deposition) material, which is enveloped in the desired sputtering gas. Hence, atoms of the target material are thus deposited on the desired substrate via the sputtering phenomenon. Figure 2.1 depicts a schematic of the sputtering mechanism.

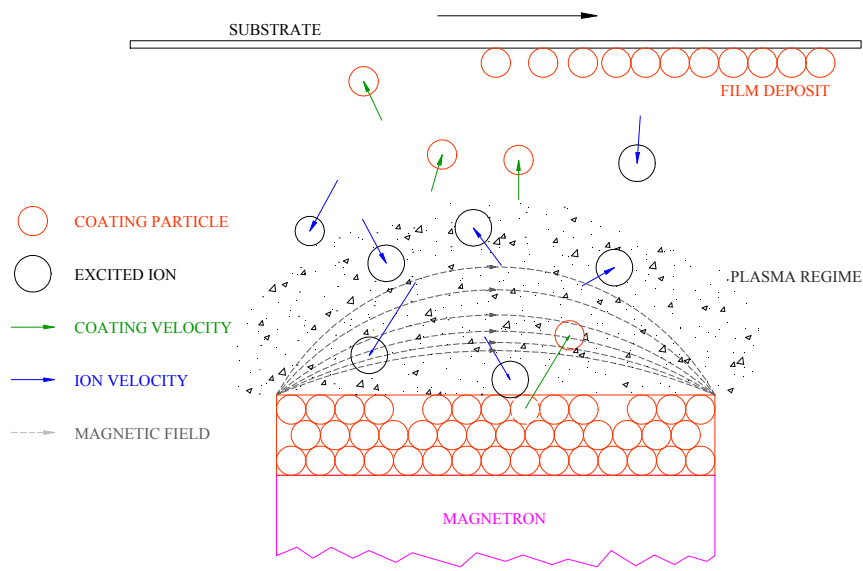


Figure 2.1 Schematic of sputtering deposition  
(adapted from Chapman & Mangano, 1988)

Today, sputtering is widely used “...in industries ranging from microelectronics, to automobiles, to architectural glass, to hardcoatings” (Wasa & Hayakawa, 1992, p. 101).

## 2.2.2 Low-Pressure Chemical Vapor Deposition

Low-pressure chemical vapor deposition represents the process of choice for the chemical precipitation of thin films (Rossi, 1988). The method of chemical vapor deposition (CVD) entails the treatment of a substrate by the localized reaction of chemicals at its surface. More specifically, CVD “...is a method of plating in which the deposits are produced by heterogeneous gas-solid or gas-liquid chemical reaction at the surface of a substrate” (Powell, 1966, p. 250). Equipment for low-pressure chemical vapor deposition includes a reactor, vacuum system, substrate, and constituent reactants. Typically, the

substrate is positioned within the reactor in the locality of the reactant introduction. Under vacuum conditions, the reactants are introduced about the surface of the heated substrate.

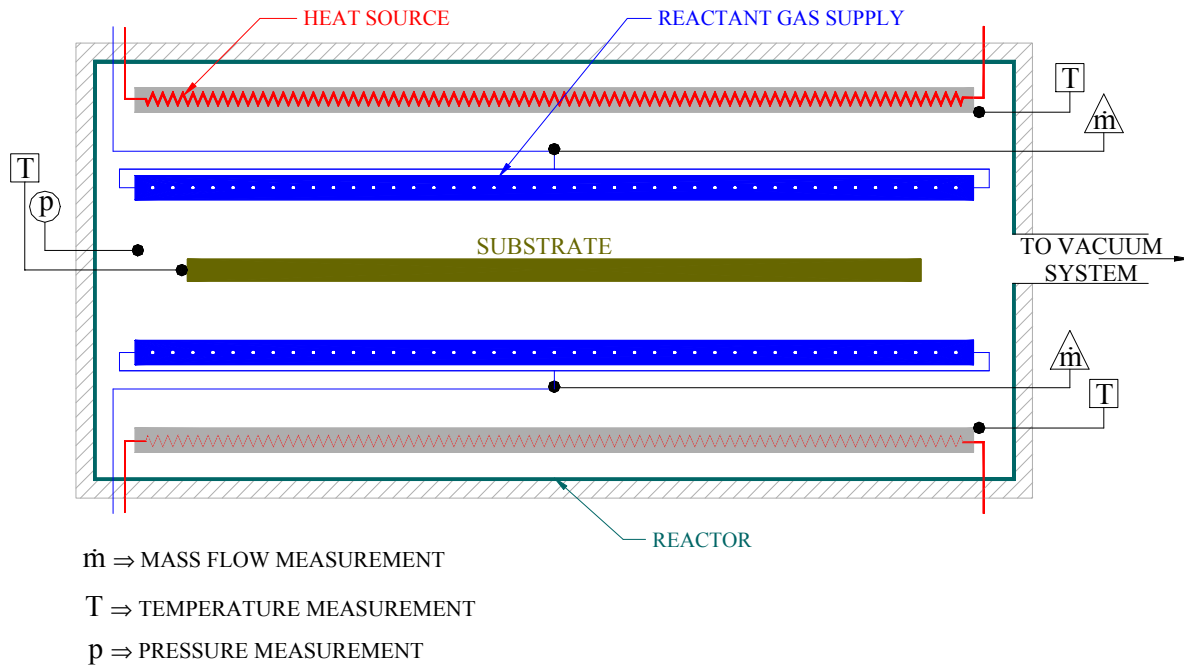


Figure 2.2 Schematic of LPCVD reactor

The resulting controlled reaction provides the favored coating. Obviously, this type of CVD is distinguished from atmospheric pressure chemical vapor deposition by the ambient pressure at which the reaction is carried out. Moreover, the efficiency, uniformity, precision, quality, and return on capital investment makes this form of CVD highly desirable in comparison to its atmospheric predecessor (Rossi, 1988). Chemical vapor deposition facilitates the plating of "...most of the refractory metals and nonmetals" (Powell, 1966, p. 249).

### **2.2.3 Physical Vapor Deposition**

Finally, the class of processes termed physical vapor deposition is to be discussed. Wherein,

- (1) A vapor is generated by boiling or subliming a source material;
  - (2) The vapor is transported from the source to the substrate; and
  - (3) The vapor is condensed to a solid film on the substrate surface
- (Kern & Schuegraf, 1988, p. 3).

Thus, quite simply, physical vapor deposition is the creation of thin film coatings by the purely physical mechanism of creating and condensing a molecular beam of source material. In that, the process evolves molecular beams or rays of coating vapor that, traveling within an evacuated space, impinge upon the whole of the chamber interior, including the substrate surface. The vapor flow is considered to be in the molecular regime because the molecular “density” of the flow is sufficiently low so as to be well beyond the realm of the viscous / compressible regime. Vacuum evaporation is regarded as the chief methodology of physical vapor deposition. Common applications of evaporative coatings include reflective, antireflective, absorptive, electro-optical, and electronic products (Ullrich, 1966).

### **2.2.4 Metallizing**

Metallizing is a common form of vacuum evaporation, and thus a process categorized as physical vapor deposition. Wherein a metal is vaporized within an evacuated chamber by feeding wire into a heated “boat” which quickly melts the consumable wire. The molten metal vaporizes rapidly, under the high-temperature and low-pressure conditions, condensing on the relatively cool surface of the nearby substrate. Figure 2.3 illustrates a common form of vacuum metallizer.

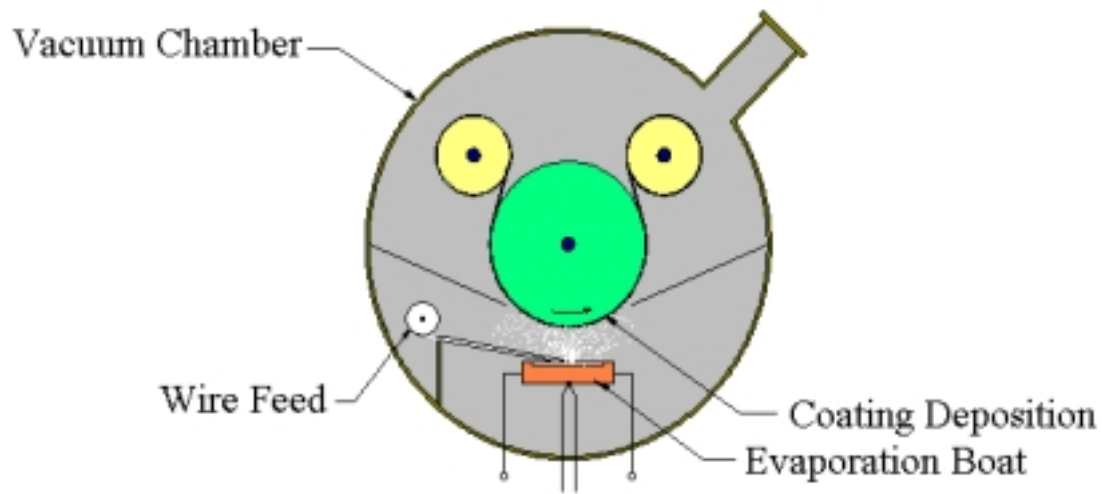


Figure 2.3 Common Vacuum Metallizer for Aluminum

The condensation, and thus deposition, of metal vapor lends the metallic coating process its name. As previously mentioned, this technique is used frequently in the coating of toys, trophies, and interior automotive trim. Most often, the metal deposition is a film of aluminum (Stuart, 1983). Although this process captures the essence of the physical vapor deposition phenomena, it does not portray the intricacies that differentiate more advanced PVD techniques from aluminum metallizing.

Specifically, the classification of vacuum evaporation processes comprises, among others, conventional vacuum evaporation, electron-beam evaporation, molecular-beam epitaxy, and reactive evaporation (Kern & Schuegraf, 1988). Such techniques may employ various components in the assembly of effective PVD process. Vacuum evaporation apparatuses include "...resistance-heated filaments; electron beams; crucibles heated by conduction, radiation, or rf-induction; arcs, exploding wires, and lasers" (Kern & Schuegraf, 1988, pp. 3-5). The facility and application of each feature provides unique characteristics to each vacuum evaporation process.

### 2.2.5 Technology of Interest: *Conventional Evaporation*

Conventional evaporation remains the most basic form of vacuum evaporation. The system of interest to this investigation may be characterized as a conventional evaporation source. Most often, conventional evaporation is a resistively heated methodology, with the source material either directly applied to the heating element or boat, or indirectly heated within a crucible. As previously mentioned, aluminum metallizing is a common manifestation of this technology. In addition to the metallizing boat, the resistance heated filament and conduction-, radiation-, or rf-induction-heated crucibles are common features of the conventional evaporation process. Common crucible, or vaporization vessel, materials include graphite, alumina, and zirconia (Wasa & Hayakawa, 1992). This process is utilized in the deposition of various metals, from aluminum and copper to gold and platinum (Stuart, 1983). Applications for conventional evaporation include gold, aluminum, and like coatings for electronic contacts and silicon monoxide and silicon dioxide deposits for low-reflectance coatings (Runyan, 1966). Figure 2.4 below depicts a schematic of a conventional vacuum evaporation system. A more detailed description of the system of concern to this study is portrayed in following sections.

Despite the obvious advantages of a simplistic conventional evaporation system, thermal and reactivity limitations may plague the implementation of this technique. In the case of resistively-heated sources, power limitations, reactivity with coated filaments, and a melting point maximum of approximately 1300°C limit the utility of these systems (Powell, 1966).

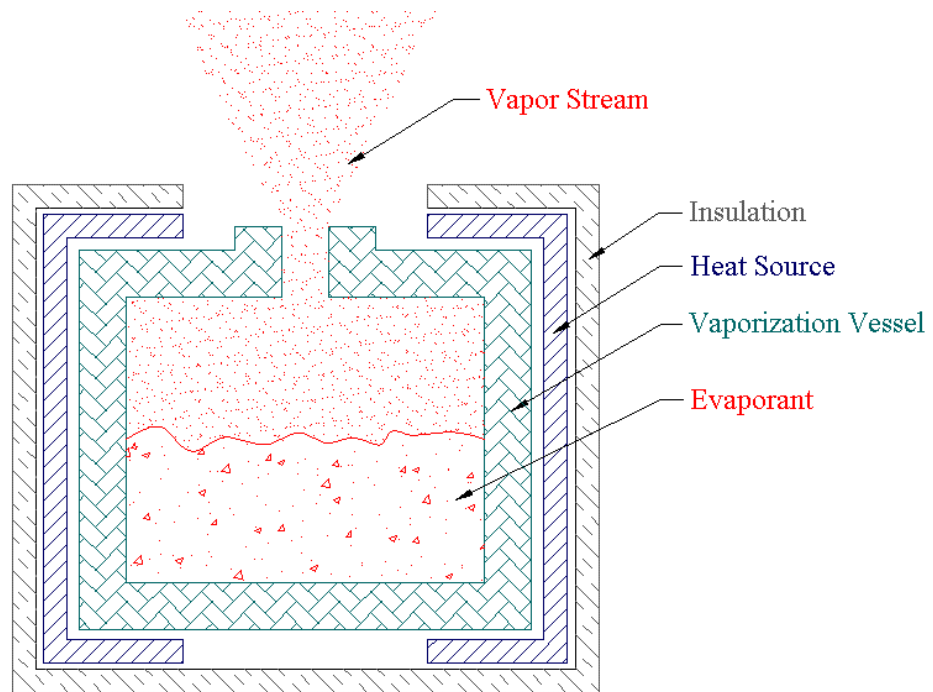


Figure 2.4 Conventional Box Evaporation Source

### 2.2.6 Electron Beam Evaporation

To overcome some of the difficulties of conventional evaporation, the implementation of electron beam evaporation has gained increasing utility (Stuart, 1983 and Konuma, 1992). Electron beam evaporation is commonly employed in the deposition of refractory metals, substances with exceedingly high melting points (Wasa & Hayakawa, 1992). “Commercially available sources typically use magnetic deflection to direct an intense electron beam into a water-cooled hearth. The evaporant charge is shaped to fit the hearth” (Knodle & Chow, 1988, p.191). The surface of the charge is heated by the sweeping beam, evaporating materials such as tungsten, cobalt, nickel, silicon, and germanium (Knodle & Chow, 1988).

### ***Molecular Beam Epitaxy***

Molecular Beam Epitaxy (MBE) represents a specific implementation of conventional evaporation or electron beam evaporation. These processes are utilized as constituent components of the process of epitaxial film deposition. Epitaxy is defined as “...a method of growing a thin layer of material upon a single crystal substrate so that the lattice structure is identical to that of the substrate” (Pitt, 1987). Kern & Schuegraf (1988) portray the MBE process as follows:

The films are formed on single-crystal substrates by slowly evaporating the elemental or molecular constituents of the film from separate Knudsen effusion source cells onto substrates held at a temperature appropriate for chemical reaction, epitaxy, and re-evaporation of excess reactants (p. 5).

As one might deduce, the primary application of molecular beam epitaxy is the growth of thin film coatings on wafers for electronic applications. Unfortunately, despite the precision and promise that this method of deposition affords, it is limited by product throughput, complex operation, and capital investment cost (Kern & Schuegraf, 1988).

### **2.2.7 Reactive Evaporation**

The final significant class of physical vapor deposition is reactive evaporation. This process may feasibly involve any of the mechanisms previously mentioned as a means of source material heating and vaporization. However, the distinction between reactive evaporation and conventional evaporation, electron beam evaporation, and molecular beam epitaxy is self-evident in its nomenclature. The utilization of chemical reaction during the evaporation process separates this methodology from those above. Furthermore, the presence of such a chemical mechanism also delineates this process from true physical vapor deposition; it is more accurately a combination of both chemical- and physical vapor depositions. Wherein, as the source material is vaporized it is intermixed

with a reacting gas to produce the desired stoichiometry of coating incident upon the substrate.

The technology of interest employs a conventional vacuum evaporation configuration that will be examined, in detail, in following sections of this thesis. The primary intent of the foregoing review of similar processes and applications is to provide substantive information on which the reader may draw for purposes of analogy, comparison, simplification, and explanation. As one might expect, the relationship between evaporation source temperature and coating uniformity is quite intimate. In fact, "...close control of [temperature][sic] in evaporation source, substrates, and CVD reactors is crucial to the reliable operation of film deposition processes" (Smith, 1995, p. 85). Recall that this principle belies the motivation for this investigation. Therefore, a survey of the precepts of heat transfer and numerical methods germane to those employed herein is requisite.

## **2.3 Heat Transfer Phenomena**

As they apply to this investigation, several modes of heat transfer are notable. More specifically, the physical system at issue experiences heat transfer in the form of conduction, convection, radiation, vaporization, and internal generation. The exploration of each of these modes is an entire field of study unto itself. Therefore, only a precursory review follows.

### 2.3.1 Conductive Heat Transfer

In the exploration of heat transfer within a conventional vacuum evaporation system, the mechanism of conduction plays a crucial role. This mode of heat transfer forms the basis for many numerical analyses and, as a diffusion mechanism, conduction conveys thermal energy across most internal interfaces of the subject experimental system. Poulidakos (1994) presents Fourier's law of heat conduction within an isotropic material as:

$$\hat{q}'' = -k\nabla T, \quad [2.1]$$

where  $\hat{q}''$  is the heat flux vector,  $k$  is the thermal conductivity of the material, and  $T$  is the material temperature. In two-dimensional problems, the gradient operator yields the following:

$$\hat{q}'' = \left(-k \frac{\partial T}{\partial x} \hat{i} - k \frac{\partial T}{\partial y} \hat{j}\right), \quad [2.2]$$

(Poulidakos, 1994). Thus, conduction is a vector quantity in the direction of the temperature gradient within the body.

### 2.3.2 Convective Heat Transfer

Convection is the mode of heat transfer occurring at the interface between a moving fluid media and a solid surface. It is actually a combination of two mechanisms, diffusion (or conduction within the fluid) and energy transfer due to the fluid action (Incropera & DeWitt, 1990). Newton's law of cooling expresses convective heat flux as:

$$q''_{conv} = h(T - T_{mean}), \quad [2.3]$$

where  $q''_{conv}$  represents the convective heat flux,  $h$  is the convection heat transfer coefficient,  $T$  is the object temperature, and  $T_{mean}$  represents the bulk mean fluid temperature (Incropera & DeWitt, 1990).

The diffusion contribution is attributed to random motion of the fluid molecules and it is incorporated by the thermal conductivity of the fluid,  $k$ . Energy transfer resulting from the fluid motion is quantified by the Nusselt number, which considers fluid velocity field, fluid properties, and the geometry of the solid surface. Correlations for the Nusselt number have been developed for numerous scenarios. These will be covered in greater detail in later sections of this thesis. The Nusselt number is defined as:

$$Nu = \frac{hL}{k}, \quad [2.4]$$

where,  $h$  is the convection heat transfer coefficient,  $L$  is a characteristic length, and  $k$  is the thermal conductivity of the fluid.

### 2.3.3 Radiative Heat Transfer

Within the physical system of interest, heat transfer by electromagnetic radiation is a dominant factor in the operation of the system. Although this fact is not immediately evident in a global sense, the internal mechanism of the vaporization source is dependent on radiative heat transfer. The rate of heat transfer by radiation is proportional to temperature differences to the fourth power:

$$q_{rad} \propto T^4 - T_{surr}^4, \quad [2.5]$$

where  $q_{rad}$  is the radiative heat transfer rate,  $T$  is the surface temperature of the object of interest, and  $T_{surr}$  is the temperature of the surroundings. One may infer that this mode

contributes most notably in cases where the surface temperature of the emissive object is far greater than that of the surroundings (Modest, 1993). The extension of the proportionality to an equality relating radiative heat transfer rate is given by:

$$q_{rad_{12}} = AseF_{12}(T^4 - T_{surr}^4), \quad [2.6]$$

where  $A$  is the surface area exposed to radiation,  $s$  is the Stefan-Boltzmann constant ( $5.67 \cdot 10^{-8} \frac{W}{m^2 K^4}$ ),  $e$  is emissivity of the hot surface, and  $F_{12}$  is the view factor relating the two surfaces of interest. At times, it may be convenient to express radiation in a “linearized” form similar to that of convection. Such a convention lends itself to the solution of otherwise nonlinear radiation problems in more expeditious and convenient linear fashion. A linearized form of the radiation heat rate is given by:

$$q_{rad} = h_r A(T - T_{surr}), \quad [2.7]$$

where,  $h_r$  is the radiation heat transfer coefficient, given by Incropera & DeWitt (1990):

$$h_r = seF_{12}(T + T_{surr})(T^2 + T_{surr}^2). \quad [2.8]$$

### 2.3.4 Internal Heat Generation

Internal heat generation may be evidenced in various forms; two most common mechanisms are nuclear generation and electrical generation. The latter is a constituent of the subject vaporization system. Electrical heat generation is a function of current and resistance, voltage and resistance, or current and voltage; Ohm’s law dictates the similarity. Wherein, electrical power dissipated by a current passing through a resistance is given by Bobrow (1985) as:

$$p = Ri^2, \quad [2.9]$$

where  $p$  denotes electrical power dissipated,  $R$  is the electrical resistance of the object, and  $i$  represents the current flowing through the body. Conservation of energy dictates that this energy then becomes available to the vaporization source as heat.

### 2.3.5 Evaporative Heat Transfer

The final mechanism of interest is vaporization. This process is characterized by the heating of a substance to a temperature sufficient to promote melting and evaporation or sublimation. With respect to heat transfer analysis, for a given mass flux leaving a control volume, the heat flux due to evaporation is:

$$q''_{evap} = n'' h_{fg}, \quad [2.10]$$

where  $q''_{evap}$  represents the heat flux due to evaporation,  $n''$  is the mass flux from the system, and  $h_{fg}$  denotes the latent heat of vaporization (or sublimation) of the source material or evaporant (Incropera & DeWitt, 1990). This may be better expressed as a rate if the mass flow rate from the system is known.

$$q_{evap} = \dot{m}_{evap} h_{fg}, \quad [2.11]$$

In this case,  $q_{evap}$  denotes the rate of heat loss from the system and  $\dot{m}_{evap}$  represents the mass flow rate from the system.

## **2.4 Numerical Methods**

The last topic requiring a preliminary introduction is that of numerical methods. The utilization of numerical methods for the solution of complex systems has gained increasing popularity and utility within the field of mechanical engineering. The advent of powerful “personal” computers and commercial finite element codes has provided an ease of access to these techniques not previously enjoyed. Furthermore, implementation of related methods may be achieved with similar efficiency and convenience.

With regard to heat transfer analysis, three general categories of numerical methods rank high among techniques commonly employed in problem solution. The Boundary Element Method (BEM), Finite Element Method (FEM), and Finite Difference Method (FDM) have seen countless applications of complex or irregular heat transfer phenomena.

### **2.4.1 Boundary Element Method**

The Boundary Element Method represents the most complex numerical method among the three covered here. However, it boasts superiority in the number of operations and storage required in obtaining solutions, chiefly because the BEM “... reduces by one the dimensionality of the problem, resulting in a smaller system of equations to be solved” (Wrobel & Brebbia, 1981, p. 111). This method is well suited to potential problems within or about arbitrary geometries (Betts & Kang, 1981). The method is driven by the use of Green’s functions to “... reduce the domain problem to a boundary integral equation form” (Betts & Kang, 1981, p. 275). This boundary integral form is then solved numerically to obtain a solution to the continuous problem. Singh and Kalra (1989) propose utilization of an improved BEM in the solution of transient one-dimensional conduction problems. This method also enjoys utility in the solution of two-dimensional transient conduction / diffusion problems as is evidenced by Wrobel & Brebbia (1981).

## **2.4.2 Finite Element Method**

A second possibility for the numerical approximation and solution of complex heat transfer questions is the finite element method. FEM offers a computationally efficient solution methodology that is somewhat less mathematically complex than the boundary element method. Finite element solutions are especially well suited to irregular geometries and three-dimensional problems where the BEM and FDM exhibit limitations. In this scheme, the continuous domain is discretized into smaller elemental portions. The governing equations of interest are systematically applied to these elements. Examining the region in summation, the process arrives at a system of equations describing the elemental and global behavior of the system. These equations may then be solved numerically with applicable techniques (Knight, 1993).

Real and Oliveira (1989) discuss a hierarchical finite element method for the solution of transient conduction problems with large gradients in temperature. In their research, they compare the traditional methods of attaining convergence by either mesh refinement or polynomial refinement. Real and Oliveira (1989) conclude that polynomial (p-type) refinement offers improvement over mesh (h-type) refinement in the areas of number of elements, data storage, and computational economy. Exact FEM solutions for linear thermal problems at steady-state are discussed by Thornton, Dechaumphai and Tamma (1981). While Zienkiewicz (1981) details the utility of finite element methods in several thermal problems including thermal stress resolution, convective-diffusive heat transfer, non-linearities in diffusion, and coupled thermal flow problems.

## **2.4.3 Finite Difference Method**

The third and final numerical method of interest is the finite difference method (FDM). Of the three at issue, this technique represents the simplest scheme of numerical solution. However, the value of this method is generally restricted to regular, or non-complex, geometries (Ozisik, 1994). Fortunately, the geometry of the physical system

examined herein may be so described. Therefore, the crux of this investigation involves the application of the finite difference method as it is applied to two-dimensional, transient heat transfer. As such, only a brief explanation of the methodology and its application will be given currently. Thorough exploration of the intricacies of FDM and its practice within this investigation will be endeavored in following sections of this paper.

The finite difference method stems from the discrete approximation of derivatives, or partial derivatives, in the governing differential equation(s). Commonly, two approaches are employed in arriving at these approximations: Taylor series expansion and control volume energy balances (Ozisik, 1994). Take, for example, the nonlinear, transient, two-dimensional conduction equation:

$$\nabla \cdot [k(T)\nabla T] + S = \mathbf{r}C_p(T)\frac{\partial T}{\partial t}, \quad [2.12]$$

where  $k(T)$  is the temperature dependent conductivity and  $S$  is a volumetric generation term. This may be written in Cartesian form as:

$$\mathbf{r}C_p \frac{\partial T}{\partial t} = \frac{\partial}{\partial x} \left( k \frac{\partial T}{\partial x} \right) + \frac{\partial}{\partial y} \left( k \frac{\partial T}{\partial y} \right) + S. \quad [2.13]$$

Following the methodology of finite difference, the partial derivatives would then be replaced by discrete approximations. Subsequently, similar equations are then generated at each nodal location within the discrete domain, creating a system of “discretized” equations. For linear systems, these equations may be solved simultaneously to calculate the temperature at each node within the body (Incropera & DeWitt., 1990). In the case of nonlinear systems, the solution technique may entail “linearizing”, quasi-linear, or nonlinear methods. Dusinberre (1961) applies the FDM to numerous classes of heat transfer problems. His text cites solutions for transient one- and two-dimensional problems, multidimensional problems, flow systems, and non-linear systems. Patankar (1991) effectively utilizes the finite difference method in the mechanics

of his heat transfer program CONDUCT, employing this tool in the solution of numerous diffusion problems. Finally, Sunden (1989) provides a most useful investigation of the transient thermal response of a stratified solid with time-dependent boundary conditions. Employing finite difference techniques, Sunden (1989) exposes the substantial impact of radiation and convection boundary conditions on the response of the layered model. It is in similar fashion that the finite difference method will be applied herein.

# Chapter 3.0

## Physical System

Recall the objectives set forth for this endeavor are three-fold.

- 1) Develop a numerical model representative of the experimental system.
- 2) Validate the numerical model against both known case studies and experimental data.
- 3) Evaluate the merits of potential enhancements to the physical system through numerical simulation and comparison.

In fulfilling these criteria, numerous subordinate tasks are methodically accomplished. The operation of the existing physical system is investigated with the goal of ascertaining significant phenomena. Data depicting operating parameters and system behavior are acquired. Subsequently, applicable governing equations describing the physical system are derived or developed from fundamental physics. Assumptions regarding the physical and analytical system are made to expedite or simplify the numerical modeling of the physical problem. A suitable numerical method with which to solve the resulting equations is then selected. Finally, refinement, validation, and implementation of this numerical model conclude the modeling process.

*Regrettably, it is imperative to note that portions of the content of the following body of information may have been omitted or disguised to protect confidential and proprietary interests. No alterations have been made affecting the validity of the investigation.*

## 3.1 Description of Physical System

As discussed, the system of interest is employed in the precipitation of inorganic coatings upon thin polymer sheet. The process may readily be termed a physical vapor deposition, but more specifically, this coating method is an example of resistively heated, vacuum evaporation. The experimental macro-system is composed of three primary sub-systems: a vacuum system, a transport system, and a deposition system.

*Nota Bene:* The term “experimental” is employed to indicate the actual production vaporization system. Its usage is purely relative to this investigation; the term bears no indication of the facility of the system to support production. In short, the term “experimental” denotes the physical system, whereas the terms “model” and “numerical” indicate the numerical model of the physical system.

### 3.1.1 Vacuum System

A typical vacuum system for film coating is comprised of a vacuum chamber, high-vacuum pumps, rough-vacuum pumps, and a series of valves for controlled operation, see Figure 3.1 below. The vacuum chamber, Item 1, houses the whole of the coating process, including both the web-handling and depositions systems, Items 2 and 6, respectively. This vessel provides a means of isolating the system from the ambient, and thus facilitates the creation of a high-vacuum environment within the chamber. This high-vacuum condition is provided courtesy of a staged pumping group, Items 3, 4, and 5. This pumping array is often composed of high-vacuum pumps, roots blowers, and rough-vacuum pumps. Often, the high vacuum units are of the diffusion or turbomolecular pump configuration. In this array, the high vacuum pump represented by Item 3 is a diffusion pump design. The intermediate pumping stage, commonly of a roots-type design, sustains a moderate vacuum for the high-vacuum pumps. Item 4, of Figure 3.1 symbolizes the intermediate roots pump for the schematic system. Finally, the roughing stage comprises rotary or reciprocating pumps, Item 5, that afford the coarsest vacuum to the roots blowers.

The development of this vacuum “atmosphere”, or veritable lack thereof, is crucial to the function of the deposition process.

### 3.1.2 Transport System

The transport system conveys the polymer substrate sheet throughout the vacuum chamber. This system of various rollers controls the web’s travel and creates a “web path” over which the substrate passes as it moves from the unwind station, through the coating region, through a monitoring zone, and onto a rewind station. Figure 3.1 portrays a common web-handling and vapor deposition arrangement, Items 2 and 6, respectively. The role of the web-handling system is critical to overall quality of the finished product as it controls winding of the semi-finished or finished product.

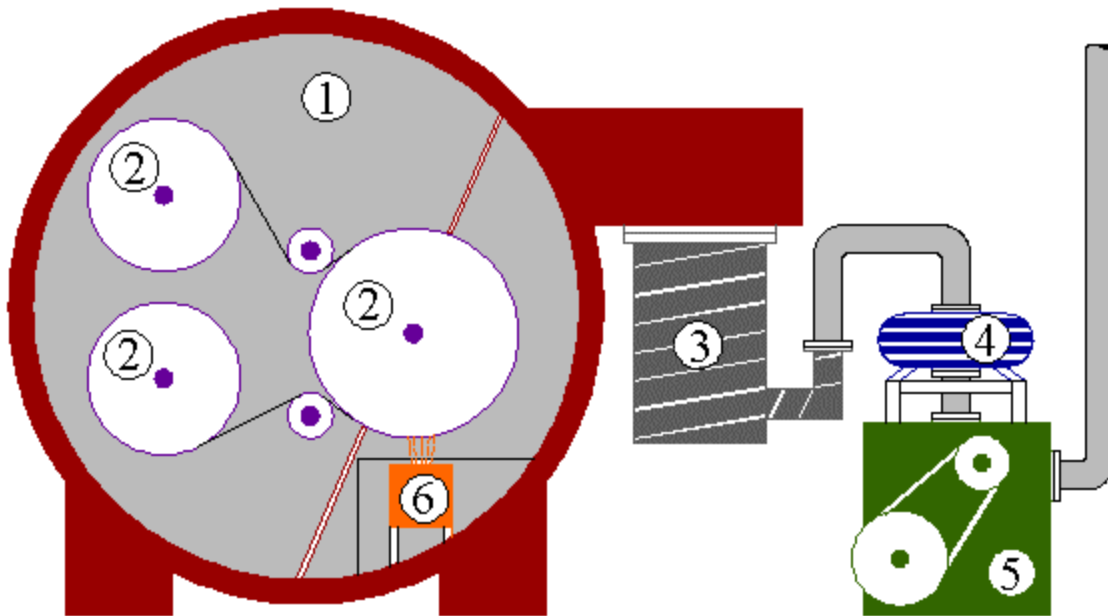


Figure 3.1 Schematic of a Vacuum Chamber for Evaporative Web Coating

### 3.1.3 Deposition System

The chief concern of the present investigation is the operation of the vaporization source or deposition system. As discussed, the deposition system of interest is simply a conventional box evaporation source. This unit comprises a set of resistive heaters, a network of cooling passages and jacketing, various layers of insulation, the consumable evaporant, and a vaporization vessel. Figures 3.2 and 3.3 depict a simplified conventional box evaporation source.

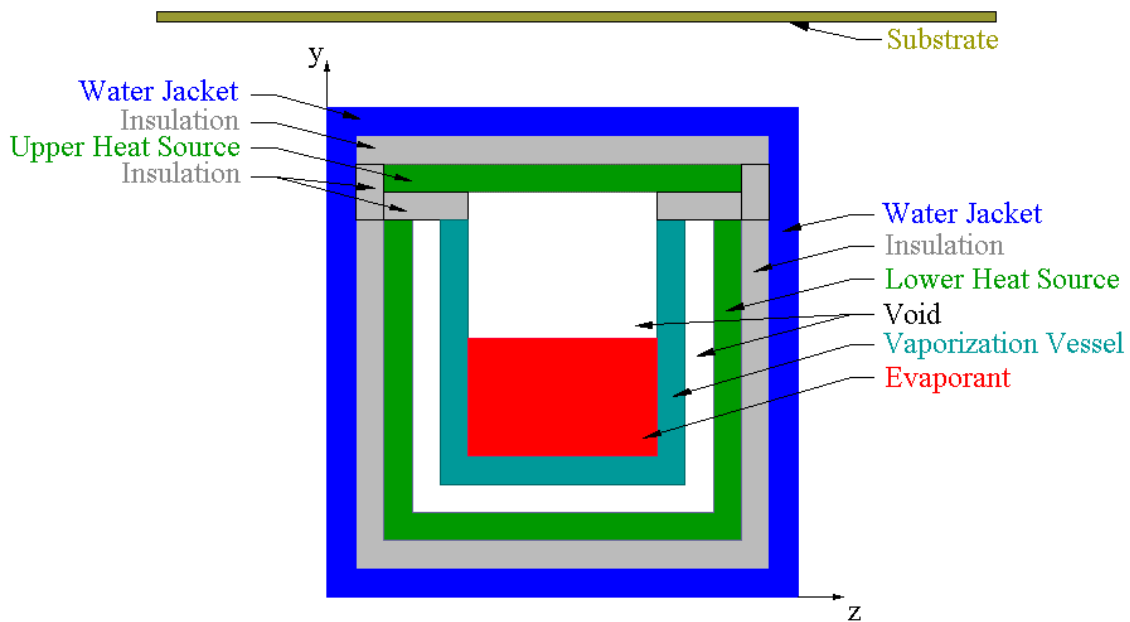


Figure 3.2 Conventional Box Evaporation Source, Cross-Section

At the exterior of the system, a water jacket provides both support for the internal components and the necessary cooling for insulated connections and structural integrity. The jacket is a series of serpentine passages surrounding virtually the entire surface of the source. In addition to those passages within the water jacket, cooling water flows throughout other temperature-critical parts of the system. Water, having an inlet temperature of approximately 20 C , flows through the water jacket's 333mm<sup>2</sup> passages at an approximate velocity of  $0.4 \frac{m}{s}$ .

Traversing toward the interior core of the source, the next layer encountered is that of the insulation. This material serves several functions. In conjunction with providing thermal insulation to the heat sources and vaporization vessel, the refractory isolates electrically “live” components from one another and from the ground plane of the source. Typical materials employed in this function include alumina and alumina-silica fibrous boards and tiles. These substances have negligible electrical conductivity and extremely low thermal conductivity. Common values for thermal conductivity,  $k$ , are on the order of  $0.5 \frac{W}{mK}$ ). The refractory insulation lines the entire length of the water jacket; a thickness of  $9.5mm$  is utilized within the physical system.

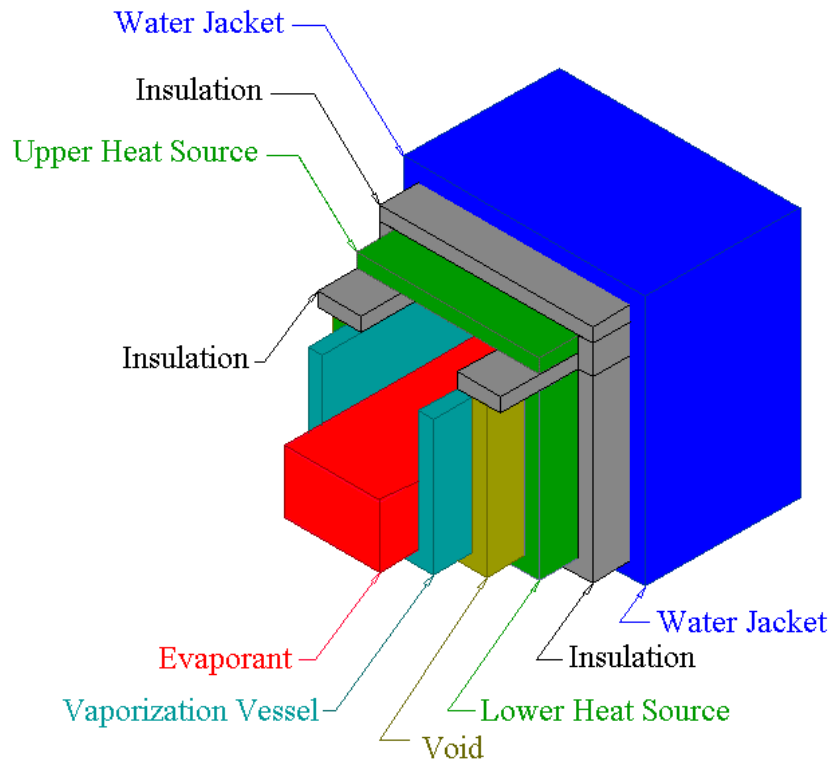


Figure 3.3 Cutaway View of a Conventional Box Vaporization Source

The third stratum, located just inside the insulation, is composed of the resistive heating elements. Within these elements, the electrical power supplied to the source is dissipated as thermal energy, thus providing the necessary heat for the vaporization process. As the heating elements are necessarily devoid of an insulating sheath, the refractory and the voided region provide electrical isolation from the remainder of the system. Materials of construction for the heating elements must possess adequate electrical resistance to enable efficient power delivery and sufficient heat dissipation. The material selected for heater construction in the physical system under scrutiny is necessarily omitted for purposes of confidentiality. The heaters utilized within the subject vaporization system span the length of the vaporization vessel, encasing it on the two longitudinal sides and bottom. Molybdenum, tantalum, tungsten, and rhenium represent a sampling of commonly selected resistive heater materials.

A vacuous, or void, region comprises the fourth layer toward the core of the system. This locale affords electrical isolation between the vaporization vessel and heating elements as it encases the whole of the vaporization vessel. Furthermore, being virtually devoid of matter, this region imparts a direct line-of-sight for radiative heat transfer between the heat sources and the vaporization vessel.

Continuing inward, the vaporization vessel follows, supported by tiny insulators positioned within the void between vessel and heating elements. The vaporization vessel contains the consumable coating material or evaporant. In its assigned role, the vaporization vessel must easily transfer heat from the heat sources to the evaporant particulate. Therefore, a relatively high thermal conductivity is desirable for this component. The vaporization vessel spans virtually the entire length of the source, with the exception of a thickness of refractory insulation protecting the ends. Common material selections boasting sufficient thermal conductivity and temperature limits include beryllium-oxide, alundum, tantalum, molybdenum, carbon, and tungsten (Powell, 1966).

Within the vessel resides the evaporant. This coating material is heated largely by radiation from the upper heat source, but also through the vessel walls, from the bottom

and the sides, by the lower heat source. Vaporization takes place at the exposed surfaces of particles within this stratum. Evaporant utilized in this investigation was acquired in granular ( $\sim 3 - 4mm$ ) form. The evaporant is loaded into the vaporization vessel and leveled to a predetermined depth. Thus, the vaporization source is now “charged” and ready for use. The evaporant material used to charge the subject vaporization source is omitted for purposes of confidentiality. Silver, copper, magnesium fluoride, zinc sulfide, and tin oxide are frequently deposited via conventional box evaporation techniques.

Moving upward, rather than inward, in the stratification, the upper surface of the coating material is bounded by yet another void. This region, however, does not primarily serve to insulate one component of the source from another. The chief intent of this vacant space is to provide a volume sufficient to function as a plenum for the coating vapor. This “headspace” will promote uniform pressure distribution within the vaporization vessel, thereby enhancing coating uniformity.

The upper heat source is situated directly above the plenum void. This heating element provides the remainder of the heat energy required to facilitate vaporization of the evaporant material. As with the lower heat source, materials of construction for the upper heat source should boast sufficient electrical resistance to enable efficient power delivery and adequate heat dissipation. Similar material may be selected as with the lower source.

Yet another layer of refractory insulation bounds the upper heat source, separating the heat source from the outermost, uppermost component, the water jacket. Figure 3.4 illustrates a major axial cross-section of a conventional box evaporation apparatus.

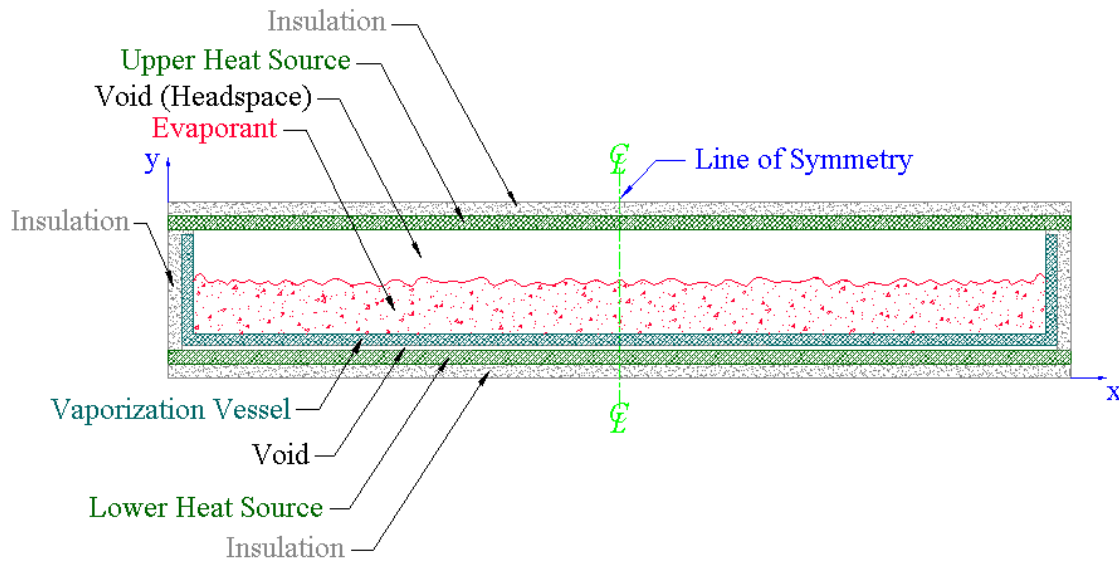


Figure 3.4 Major Axial Section of a Conventional Box Evaporation Apparatus

Now familiar with the construction of the physical vaporization system, an exploration of system operation is in order.

### 3.1.4 System Operation

Operation of the production deposition system follows that of most any conventional box evaporation source. In that, the vaporization source is charged by loading the evaporant source material into the vaporization vessel. The source is then brought to vacuum operating conditions within the vacuum chamber. Once under sufficient vacuum, power is introduced to the heaters surrounding the vaporization vessel. A closed-loop-controlled power feed maintains proper heat application from both of the heat sources, gradually heating the vaporization vessel, and the evaporant within, to each subsequent temperature setpoint throughout a stepped series. As the temperature of the source material approaches the final operation setpoint, vaporization begins within the vessel. As the partial pressure of coating vapor within the headspace above the solid

evaporant increases, coating vapor begins to evolve from the source portals, moving throughout the chamber, and precipitating on the substrate. This controlled evaporation and condensation of source material upon the surface of the passing substrate yields the desired deposition, see Figure 3.5.

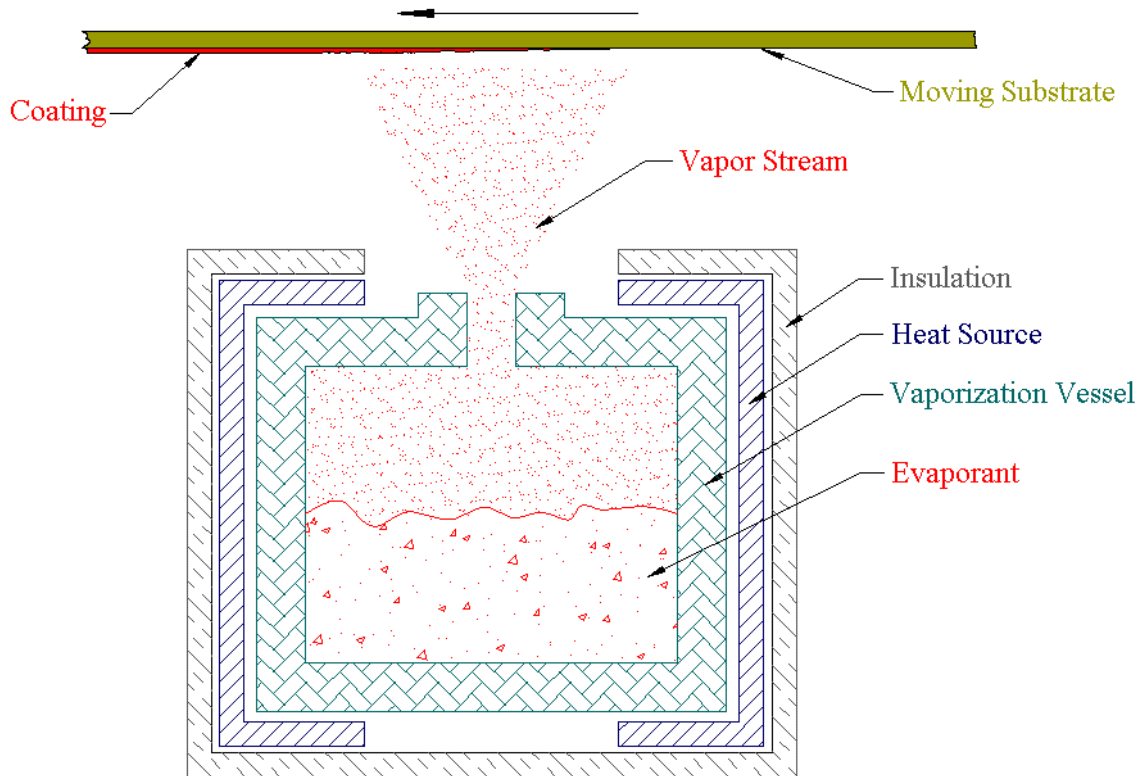


Figure 3.5 Physical Vapor Deposition from a Conventional Evaporation Source

### 3.2 Relevant Physical Data

In developing an effective numerical simulation of the physical system, it is first necessary to derive an accurate representation of the accompanying physics. The physical events present within the operation of the experimental vaporization system must be described in a manner suitable to analytical physics. Moreover, to formulate a model of the relevant physics, numerous supporting data are essential to fully describe notable

phenomena. System geometry, material properties, and operations data are crucial to an accurate understanding and viable model of the physical vaporization system.

Three classes of data comprise that required by this investigation.

- 1) System physical geometry conveys the physical geometric configuration of the source construction.
- 2) Material properties describe the behavior of the constituent materials when subjected to prescribed conditions.
- 3) Operations data portray the response of the physical system subject to prescribed production conditions.

### **3.2.1 Physical Geometry**

The geometry of such a system may be obtained from direct field measurements, from engineering drawings of the vaporization source, or as a matter of design intent in a newly burgeoning project. Regardless of their origin, these data describe the relationship of subordinate parts within the macro-system. The accurate computation of areas, volumes, and volumetric terms are dependent on the acquisition and utilization of proper geometry data. In the case of this investigation and the vaporization system of interest, the geometric dimensions and configuration of strata were obtained from a combination of field measurements and known engineering data. Although specific dimensions are proprietary, system dimensions based on a length of unity are approximately 0.1 wide by 0.1 deep by 1.0 long. For the purposes of this investigation, particularly validation and simulation, system dimensions were exactly duplicated within the numerical model. For reasons of confidentiality, information detailing source dimensional construction is purposely omitted. However, in applying this model to a similar system of arbitrary geometry, duplication of those arbitrary dimensions within the numerical model should afford results comparable in validity to those obtained herein. Numerical input requirements may be viewed in the hardcopy Mathematica<sup>®</sup> code of the numerical model within Appendix H.

### **3.2.2 Material Properties**

In a project such as this, procurement of a substantial quantity of material properties is requisite. This information may be researched, furnished, derived, or determined experimentally. For common materials, and for common physical quantities, such data is available in compiled tabular or graphical form in numerous reputable resource materials. Some common examples include the steam tables, the CRC Handbook, Perry's Chemical Engineer's Handbook, and the JANAF Tables. Thus, properties may be sought within a research facility, via the internet, or within university libraries. If unavailable as compiled data, material properties may often be acquired from the material manufacturer or distributor. As a matter of due course, this method generally yields data more representative of a given specimen than compiled "typical" values. Failing to obtain the necessary information in the previous two fashions, one may derive needed information using known physical laws/relationships, known empirical formulae, or a combination thereof. Typical examples include the use of Fourier's Law and Ohm's Law to obtain property data. Finally, in the event that the foregoing avenues yield no results, experimental means may be employed to discern property values. Calorimetry and Differential Thermal Analysis (DTA) are valuable tools in this arena. Property data for this investigation was acquired through traditional research, from specifications supplied by the manufacturer, and by experimental determination using differential thermal analysis.

### 3.2.3 Heat Source, Vaporization Vessel, and Refractory Properties

The vast majority of property data employed within this project was acquired in tabular or graphical form through traditional research. Materials for the heat sources, vaporization vessel, and refractory insulation are ordinary. Thus, values for their specific heats, at discrete points throughout a range of temperatures, were obtained from documented sources. The specific heat curve for the heat source material was obtained from the International Nuclear Safety Center web site operated by Argonne National Laboratory. The function representing the refractory's temperature-dependent specific heat was acquired from Perry's Chemical Engineers' Handbook.

Values for temperature-dependent thermal conductivity were not readily available within the resources consulted. Therefore, this data was sought from the respective manufacturers. Nonlinear curve fits were applied to this data, providing functions from which thermal conductivity values may be numerically evaluated at given temperatures.

Tabular representation of this information is available within Appendix A. Figure 3.6, Panels a) and b) graphically illustrate the temperature dependence of the heat source, vaporization vessel, and refractory insulation material properties.

### 3.2.4 Evaporant Properties

With regard to the deposition material, because of its limited industrial use, compiled property data for this substance is somewhat scarce. As to thermal conductivity, an order of magnitude approximation of  $1.4 \frac{W}{mK}$ , based on similar materials, was used. Values for the bulk density and the heat capacity of the evaporant granules were obtained by experimental means.

The bulk density of the source material was determined in familiar fashion. Known volumes of granules were massed on a calibrated laboratory scale. Using the formula:

$$\mathbf{r} = \frac{m}{V}, \quad [3.1]$$

where,  $\mathbf{r}$  is the bulk density of the evaporant granules,  $m$  is the mass of evaporant, and  $V$  is the volume of evaporant, the bulk density of the evaporant was calculated to be  $1025 \frac{kg}{m^3}$ .

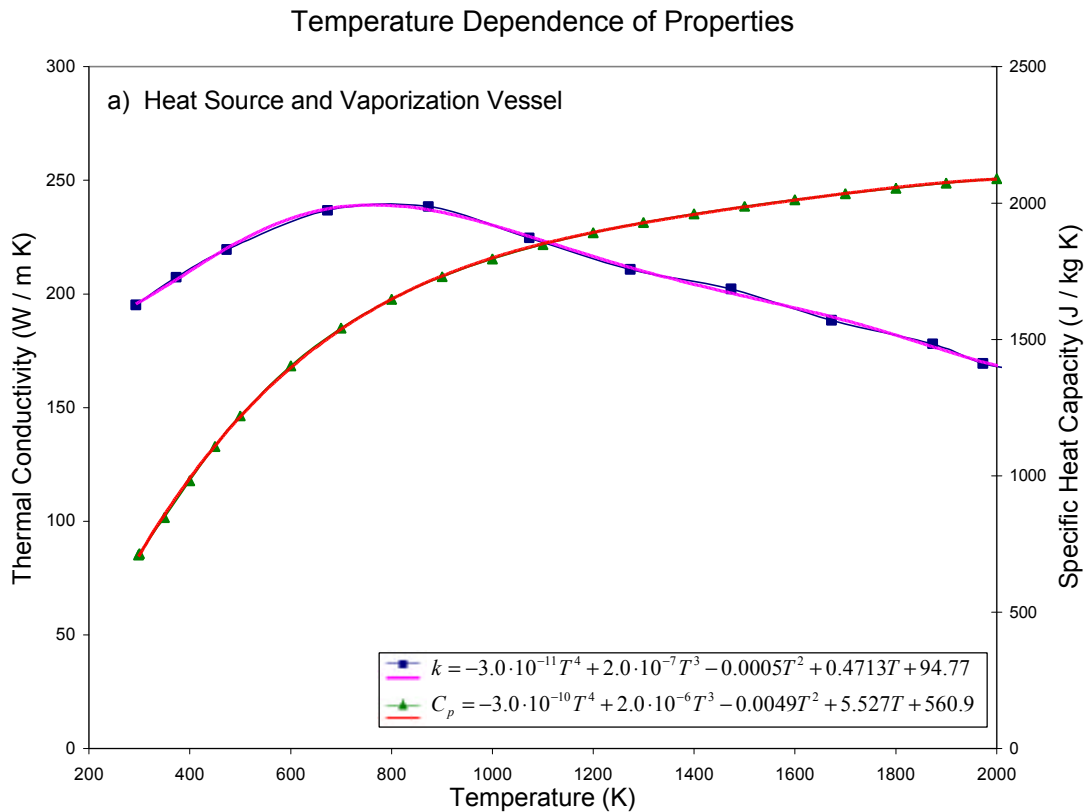


Figure 3.6 Temperature Dependence of Material Properties

### Temperature Dependence of Properties

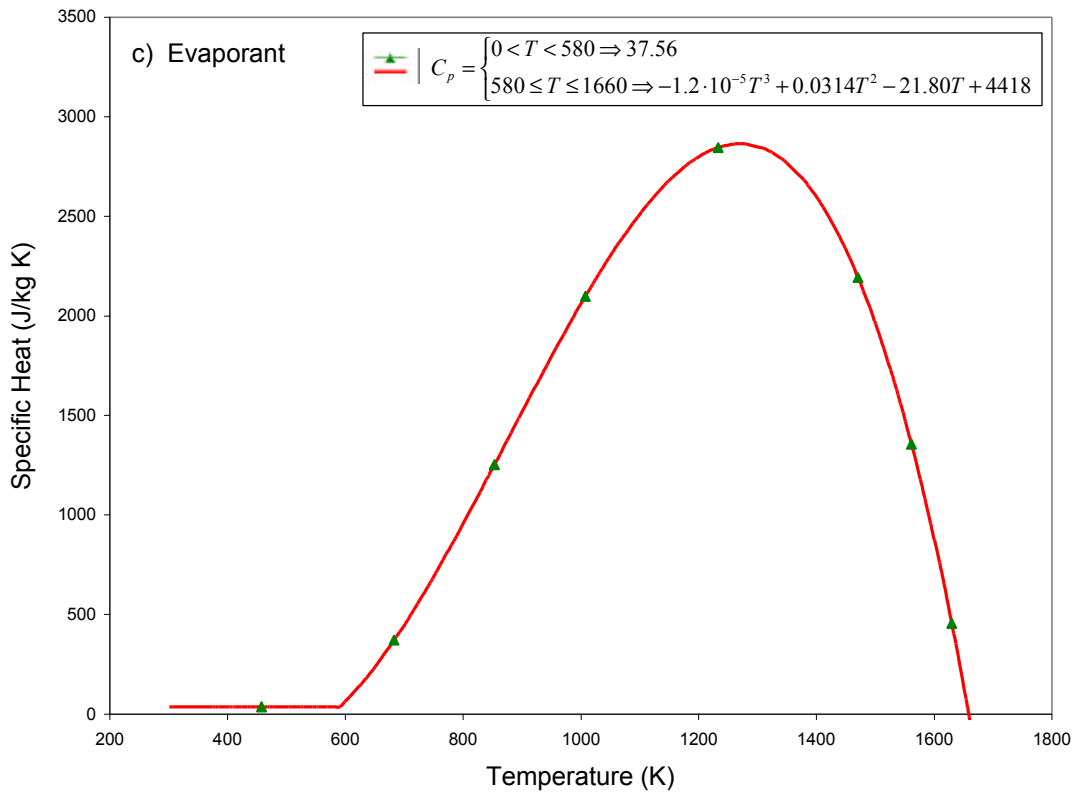
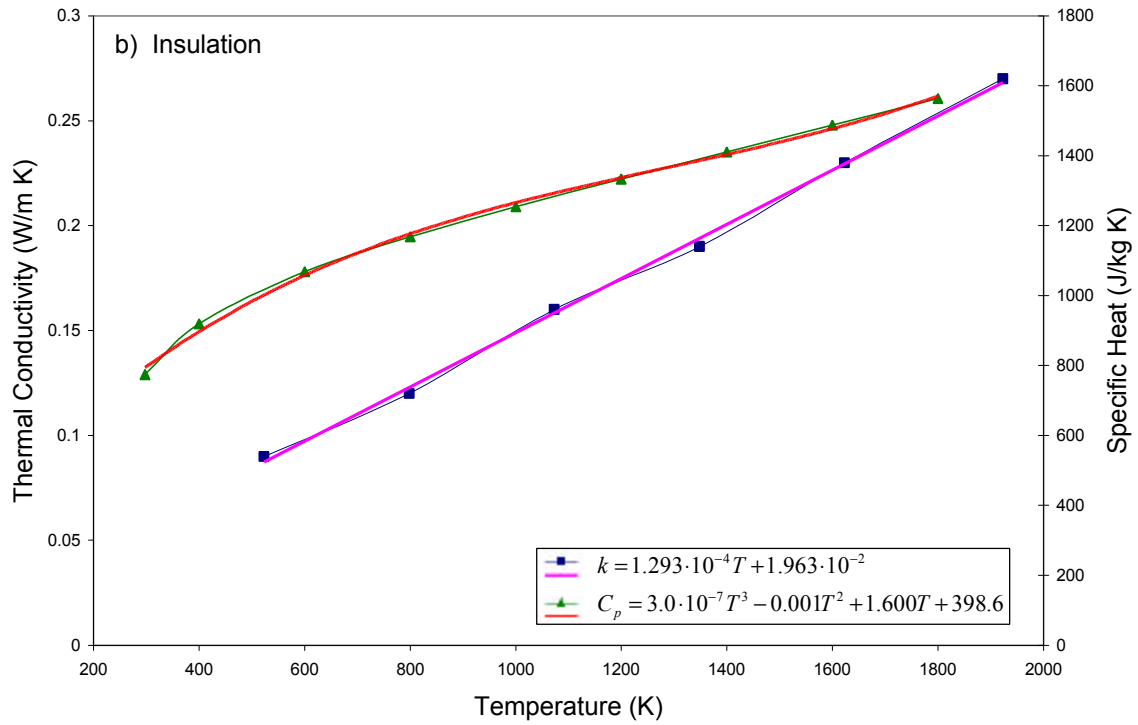


Figure 3.6 (continued)

Temperature Dependence of Material Properties

The final requisite material property to be determined is the specific heat capacity of the evaporant material, depicted in Figure 3.6, Panel c). A convenient method of acquiring this information is the Differential Thermal Analysis (DTA) discussed below. This process “...measures energy released (exotherm) or absorbed (endotherm) by a material due to physical or chemical changes as it is heated or cooled at controlled rates” (Coming, 1998, §12.1.1).

### 3.2.5 Calorimetric Differential Thermal Analysis

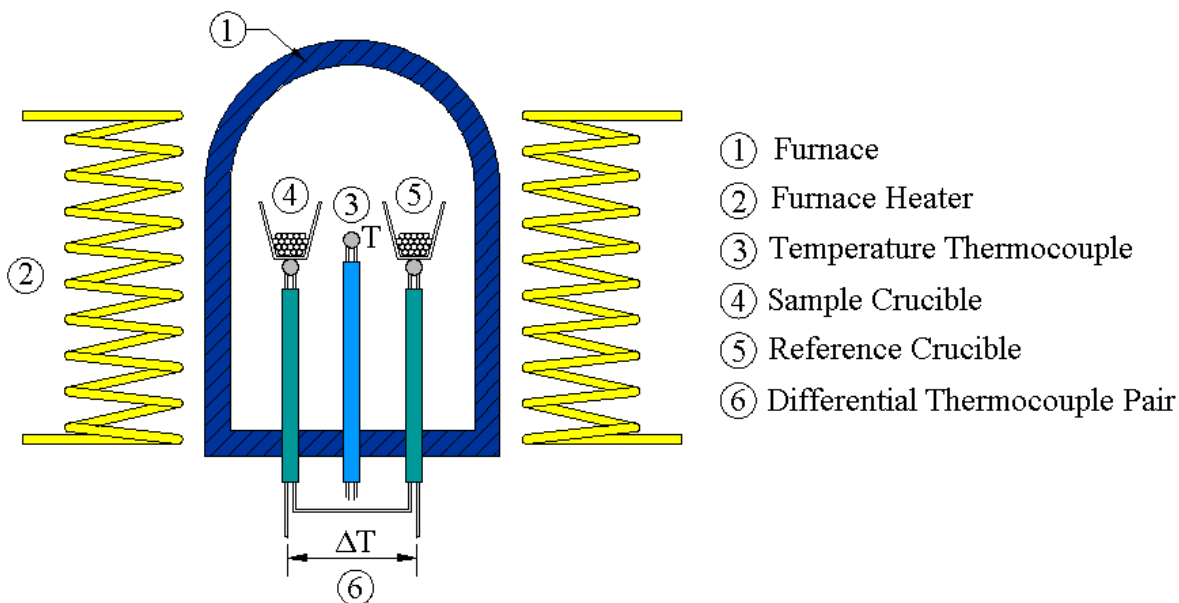


Figure 3.7 Schematic of a Boersma-Type Calorimetric DTA System

The DTA unit, as it appears in Figure 3.7 above, is composed of: a furnace (1), furnace heaters (2), a thermocouple junction (3), a sample and sample crucible (4), a reference sample and its respective crucible (5), and a differential thermocouple pair (6) arranged to sense a temperature differential between the sample and reference. The thermocouple junction, recording system instantaneous temperature, is purposely located in the ideal heat flow path between the two samples (Daniels, 1973). Whereas, the thermocouple pair is connected so that readings of differential temperature are obtained from the reference and sample crucibles. Notably, the junctions of the differential

thermocouples sense the temperature of the reference and sample crucibles, which eliminates any influence that the thermal properties of the sample may have on the differential measurement (Daniels, 1973). Common DTA systems will operate up to 1400°C, utilizing samples of 10–20mg, at heating rates in the 10-15°C/min range (Corning, 1998).

### **3.2.6 Operation of Differential Thermal Analyzer**

As the furnace and samples are heated at a prescribed rate by the heating system, the sample undergoes thermal, chemical, and / or physical changes as a thermal gradient is established between it and the reference. As Daniels (1973) skillfully portrays, “...in the absence of a thermal event a stable temperature gradient is set up along this path” (p. 107). Any occurrence in the sample, that is unseen within the reference, will produce an unsteady thermal gradient between the two. “The absorption or evolution of heat by the sample causes a change in the thermal gradient in the sample side of the system, and the gradient then differs from that in the reference side, resulting in a differential temperature signal” (Daniels, 1973, p. 107).

A typical DTA plot will depict differential temperature as a function of temperature. This may then be integrated to obtain energy evolved or absorbed by the sample. This quantity includes both sensible and latent energy, the energy required to raise the temperature of a substance to a phase change temperature and the energy required by the phase change, respectively.

However, fortune prevailed upon this investigation; the laboratory providing DTA services, Corning Engineering Laboratory Services, utilizes a slightly different DTA system. The results of the DTA analysis of the evaporant sample were supplied depicting energy evolved as a function of temperature, generated at a constant heating rate. Thus, by simply converting the sample mass and measurement units to standard forms, a value for

heat capacity at various temperatures was obtained. Equation 3.2 demonstrates the employed conversion:

$$C_p(T) = \frac{(q_{evolved} \text{ mW}) \cdot \left( \frac{1\text{W}}{1000\text{mW}} \right)}{(m_{sample} \text{ mg}) \left( \frac{1\text{kg}}{1000^2 \text{ mg}} \right) \left( \frac{q_{rate} \text{ K}}{\text{min}} \right) \left( \frac{1\text{min}}{60\text{s}} \right)}, \quad [3.2]$$

where,  $C_p(T)$  is the temperature-dependent heat capacity,  $q_{evolved}$  represents the heat evolved during the analysis,  $m_{sample}$  is the sample mass, and  $q_{rate}$  signifies the heating rate. From the reduced data, temperature and heat capacity, a composite function, equation 3.3, describing heat capacity behavior was produced via polynomial regression:

$$C_p(T) = \begin{cases} 0 < T < 580\text{K} \Rightarrow 37.56 \\ 580 \leq T \leq 1660\text{K} \Rightarrow -1.2 \cdot 10^{-5} T^3 + 0.0314 T^2 - 21.80 T + 4418 \end{cases} \quad [3.3]$$

Figure 3.6, Panel c) presents the resulting plot of temperature-dependent heat capacity, including sensible and latent heat, for the evaporant material. Appendix B presents the raw DTA data utilized within.

### 3.2.7 Operations Data

Having obtained or determined the thermophysical properties of the vaporization source's constituent materials, the investigation lacks only operations data in amassing the experimental information required to create and validate an accurate numerical model. Fortunately, as a matter of necessity to the operation of a production vaporization system, an operations data acquisition system exists in a useful state, available to this study.

The data acquisition system comprises a clock, temperature sensors, pressure sensors, distance counters, voltmeters, and ammeters. This information is fed to data cards

in the process monitoring PC and displayed and recorded by data acquisition software similar to Labview or WorkBench PC. Although crucial to process monitoring and troubleshooting, the pressure- and distance-sensing modules of the data acquisition system are of little interest to this thesis; they simply supply necessary process data to the system operator. The clock function permits tracking of process elapsed time. The temperature sensing modules consist of nine type-B platinum-rhodium thermocouples positioned strategically along the length of the vaporization source, and connected to the data acquisition PC. Thermocouple locations were previously selected to be located longitudinally, either: left, center, or right, denoting the ends and center of the vaporization source. Thus, the three longitudinal locations correspond to nine global locations, as shown in Figure 3.8 below: upper-left, vessel-left, and lower-left; upper-center, vessel-center, and lower-center; and upper-right, vessel-right, and lower-right, indicating sensors reading the left position, center position, and right position, respectively.

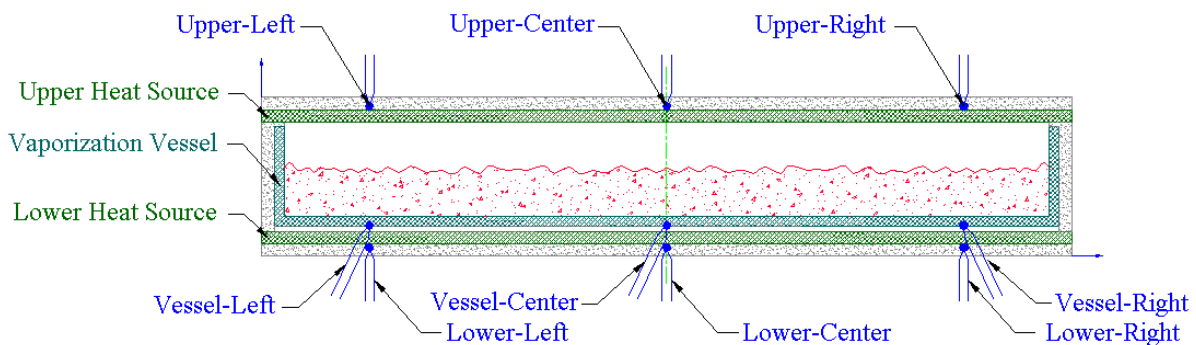


Figure 3.8 Source Thermocouple Locations

The voltmeters and ammeters are attached to the heat source power supplies, supplying voltage and current measurements to the data acquisition system.

Culling the required information from the ASCII text files recorded by the data acquisition system was accomplished using Microsoft<sup>®</sup> Excel, the same facility employed in the production of a majority of the plots contained herein. Specifically, the text data provided by the data acquisition PC was imported into Excel for function generation and output validation.

The temporal data supplied by the data acquisition system was converted from elapsed time in hours, minutes, and seconds to elapsed time in seconds. In this manner, the data correlates directly with that supplied to or generated by the numerical model.

Power information from the data acquisition system is supplied as instantaneous voltage and current readings at each time-step in the data log. These values were converted, via equation 2.9 from section 2.3.4, to power input data and plotted to determine a power input function for each of the heat sources. More information regarding power input data is conferred within section 6.1.5.

The temperature data supplied by the data acquisition system is of similar form to that of the power readings, i.e. instantaneous temperature readings taken, from each of the nine thermocouples, at each 20-second time-step in the data log. The temperature values logged by the PC are recorded in degrees Celsius. A typical example of power input and transient response for one thermocouple position is shown in Figure 3.9 below.

Transient Response: Experimental Data Set I, Center Position

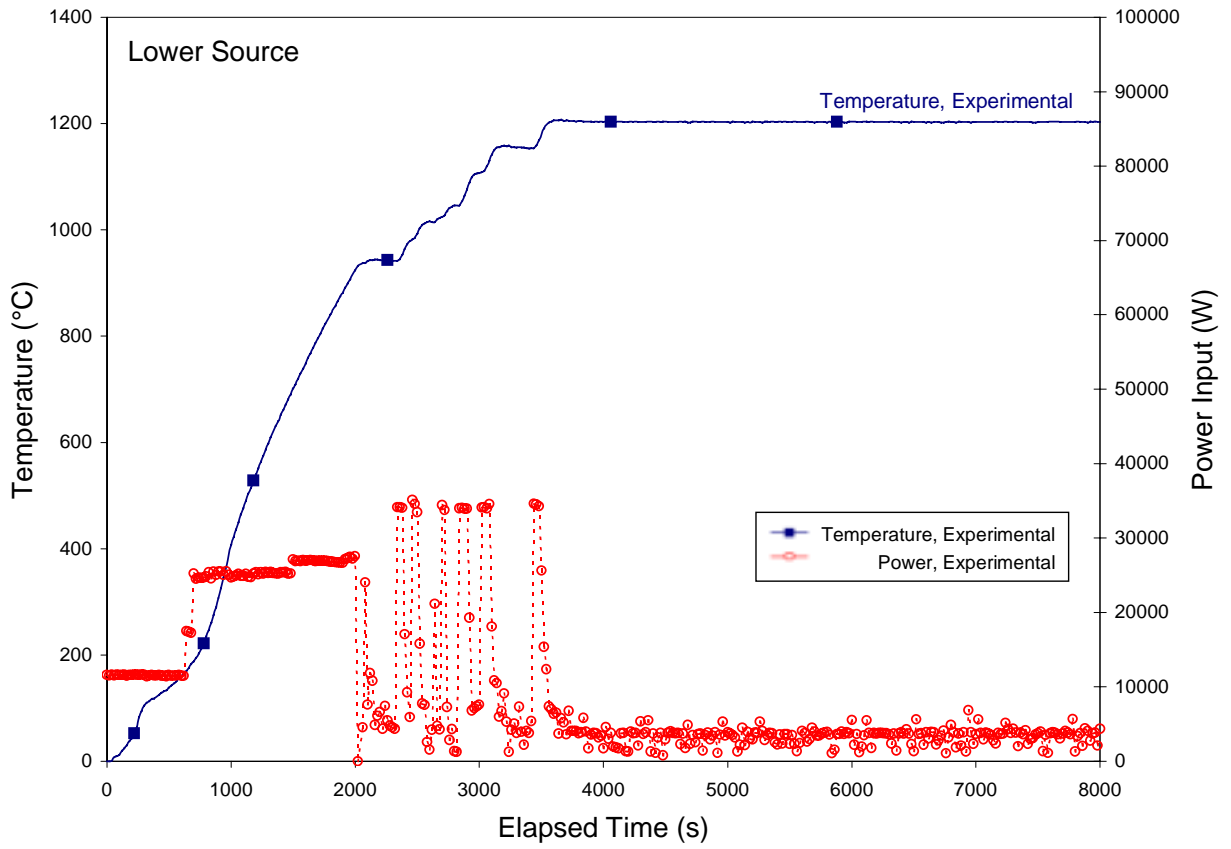


Figure 3.9 Typical Heat Source Input and Transient Response

# Chapter 4.0

## Modeling of the Physical System

### 4.1 Relevant Physics

Having accrued the necessary background, geometric, material, and operations data, logical progression leads to the selection of relevant physical phenomena.

With regard to significant physical phenomena, the vaporization source of interest experiences five significant physical transport or transfer phenomena:

- 1) electrical power input and subsequent internal generation,
- 2) radiative heat transfer to the surroundings and within the system boundaries,
- 3) convective heat transfer to the encasing water jacket,
- 4) evaporative cooling via the removal of heated vapor mass from the system, and
- 5) conduction throughout.

Modes 1) through 4) are briefly introduced within the following sections. Conduction forms the basis for the finite difference model developed herein. Therefore, special treatment will be given to this topic in Chapter 5.0. Please refer to Figure 4.1 below for visualization of the following introduction to each pertinent physical phenomenon.

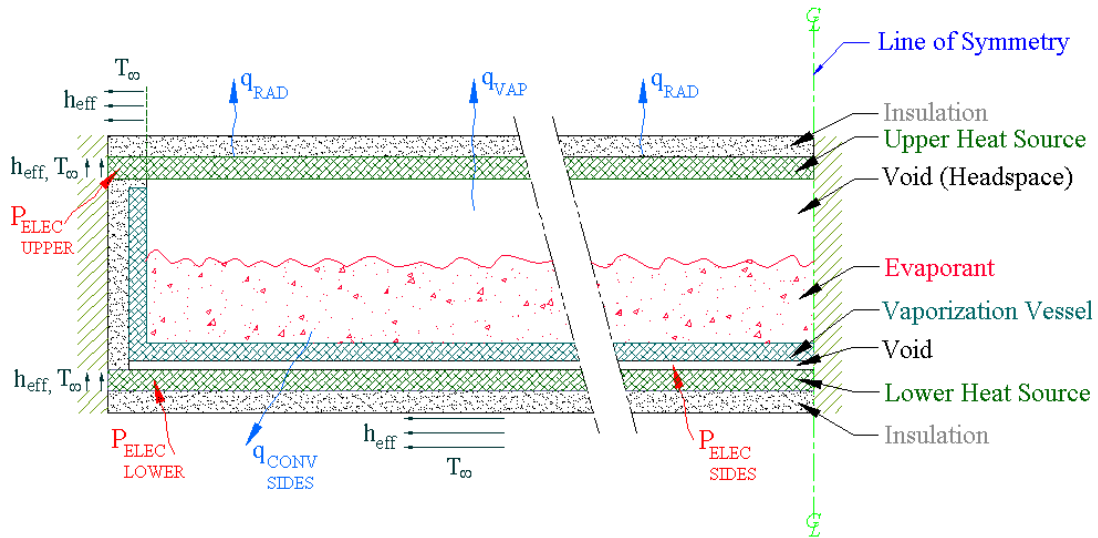


Figure 4.1 General Schematic Representation of Model Physics

#### 4.1.1 Electrical Power Input

As a resistively heated conventional box evaporation system, the experimental system relies upon electrical power input as its sole source of heat input or generation. Wherein, the previously noted equation related by Bobrow (1985) for electrical power dissipation applies:

$$p = Ri^2. \quad [2.9]$$

This dissipated power is manifested in the form of heat energy, which in mechanical engineering nomenclature is commonly denoted by the symbol  $q$ .

In general, during the transient phase of the system's operation, electrical power is supplied in discretely increasing quantities, or steps, corresponding to a predetermined heating schedule. Once the system reaches operating temperature, the power input remains constant at a level sufficient to sustain vaporization. Power input functions for each heat source are obtained from data acquisition logs from the physical vaporization system. The experimental power input function shown in Figure 4.2 below depicts a typical stepped application of power to the lower heat source.

### Power Input: Data Set I

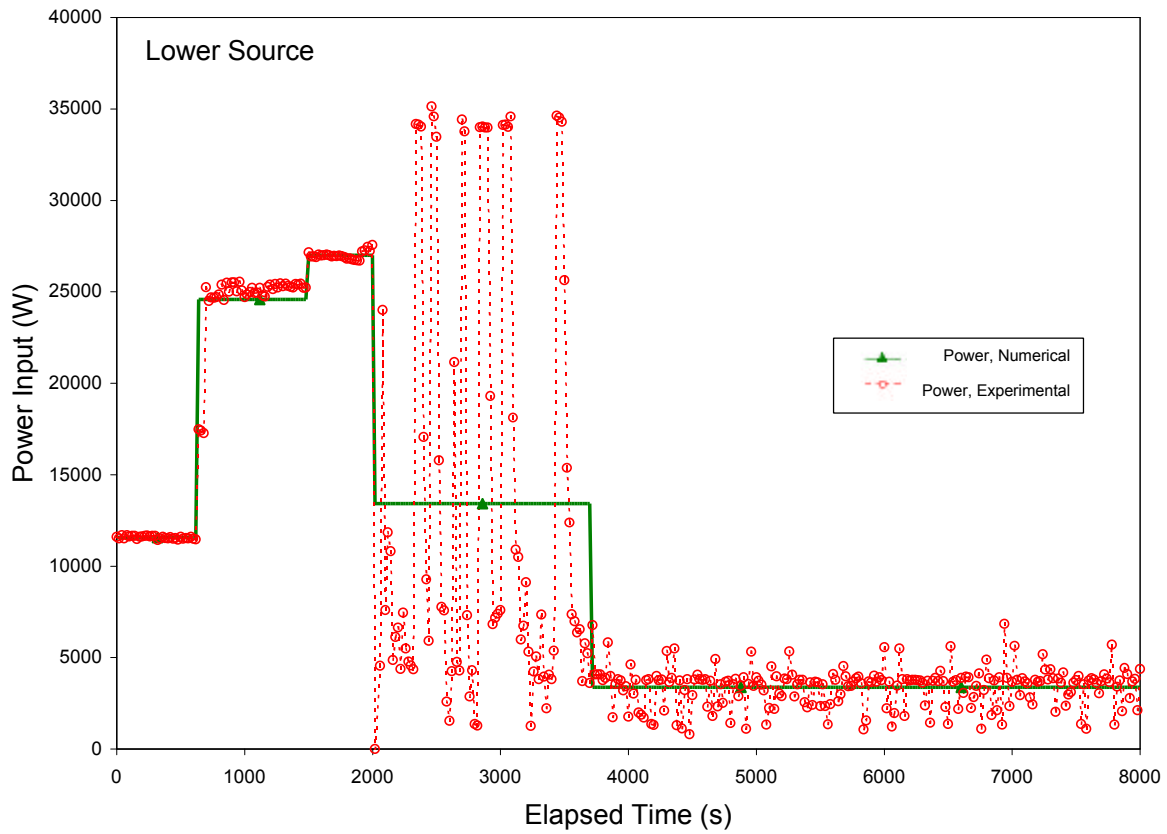


Figure 4.2 Typical Stepped Power Input

Similar functions were subsequently employed within the forthcoming numerical model to replicate the behavior of the experimental system inputs. Further illustration of these inputs is given in section 6.1.5, within Figures 6.10 and 6.13.

## 4.1.2 Radiative Phenomena

In addition to electrical heat generation, the physical vaporization source experiences radiative heat transfer with both internal and external objects. Surfaces within the system exchange energy by radiative heat transfer just as external surfaces of the source undergo radiant heat transfer with the surroundings.

### *Internal Radiation*

With regard to internal radiation, this mode is established within the experimental system in light of the vacuous environment and the absence of thermal surface contact. Specifically, noting Figure 4.3 below, radiation is the only possible mode of heat transfer across the upper heat source-evaporant “interface” and the lower heat source-crucible “interface” because of the included voided region adjoining each surface.

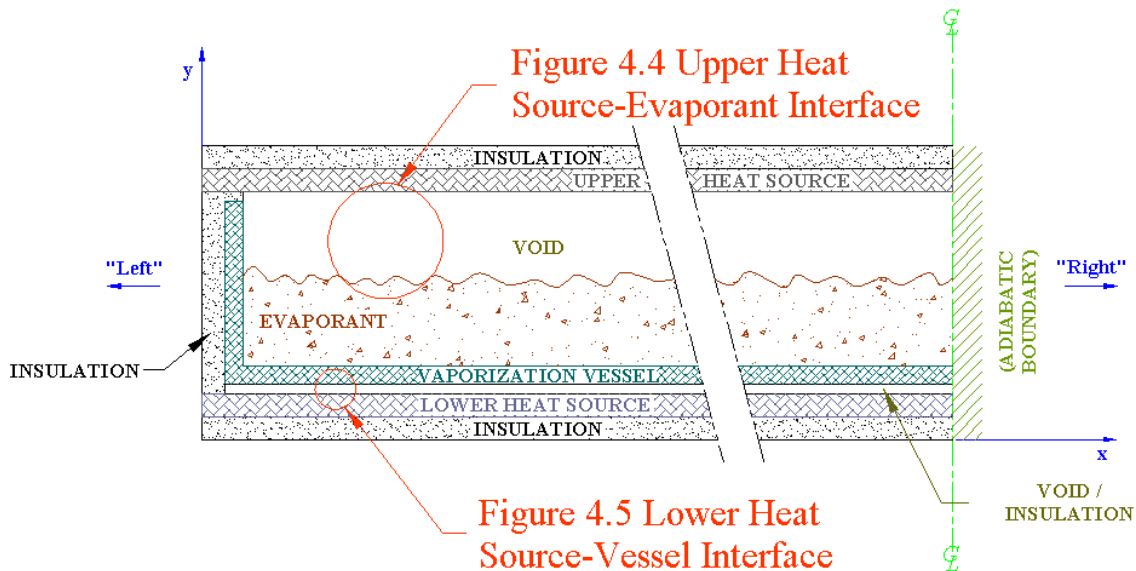


Figure 4.3 Sites Experiencing Internal Radiation Transfer

Figures 4.4 and 4.5 illustrate the upper heat source-evaporant interface and the lower heat source-vessel interface.

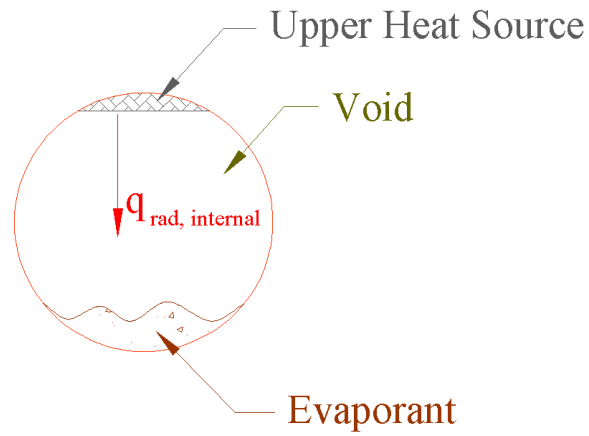


Figure 4.4 Upper Heat Source-Evaporant Interface

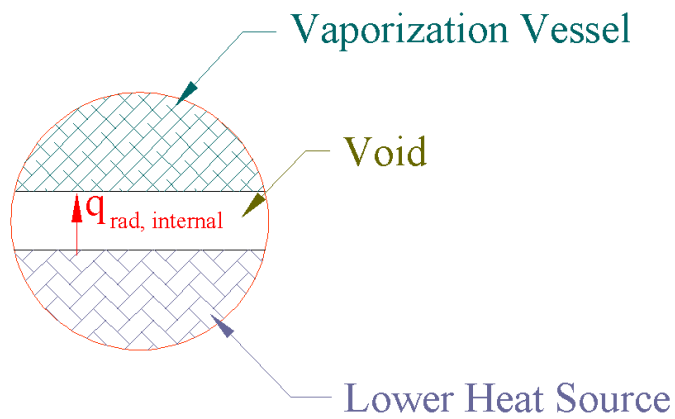


Figure 4.5 Lower Heat Source-Vessel Interface

In both scenarios, heat,  $q_{rad, internal}$ , is transferred via radiation from the respective heat source to the target surface. Mathematically, this takes the form:

$$q_{rad, internal} = \frac{\mathbf{s}A(T_1^4 - T_2^4)}{\frac{1}{\mathbf{e}_1} + \frac{1}{\mathbf{e}_2} - 1}, \quad [4.1]$$

where  $q_{rad, internal}$  is the radiative heat transfer. Assumptions regarding the applicable view factor are discussed within section 4.2.2. Development of this phenomenon within the framework of a generation or “source” term is outlined in section 5.3.1.

### ***External Radiation***

Considering external radiation, or radiative heat exchange with the surroundings, this model parallels the development of basic radiation. Examining Figure 4.6 one observes that only the upper boundary of the source experiences radiation to the ambient.

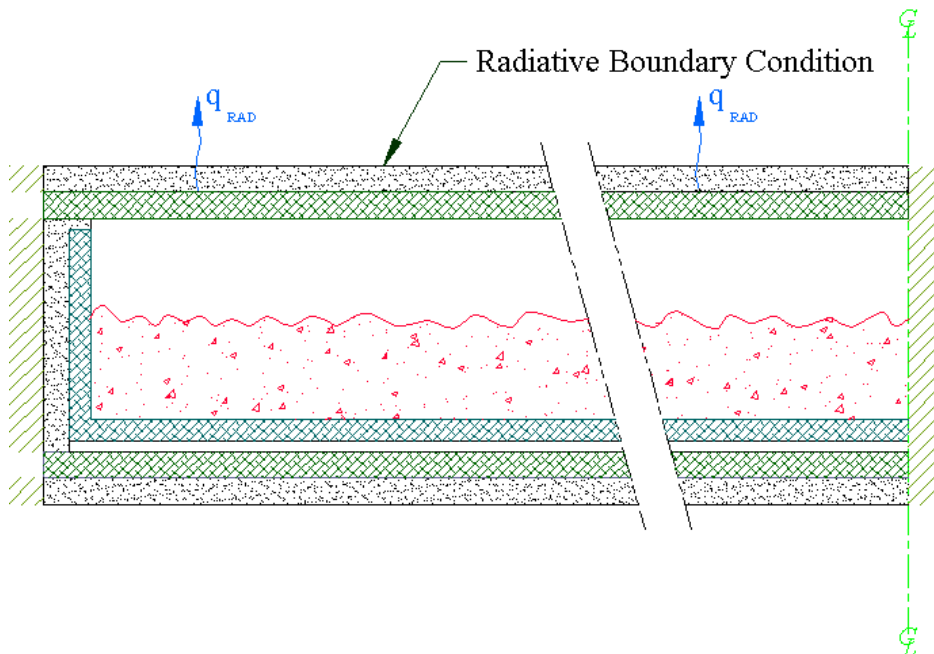


Figure 4.6 Radiative Boundary Condition

As noted earlier, this occurrence is analogous to a small object radiating within a large enclosure. Wherein, the emissive surface of the experimental vaporization source may be approximated as a small object within the large enclosure represented by the vacuum chamber. Hence, equation 4.2 describes the net radiative heat transfer.

$$q_{rad} = A\epsilon e(T^4 - T_{surr}^4), \quad [4.2]$$

In the experimental situation, as well as within the forthcoming numerical model, the surrounding temperature is constant at  $25^\circ C$ . Furthermore, in light of the material of construction for the emissive surface, an emissivity of 0.95 was employed.

### 4.1.3 Convection Heat Loss

Although only the uppermost external surface of the vaporization source undergoes radiation exchange with the surrounding surfaces, virtually the entire perimeter of the vaporization system is exposed to a forced convection boundary condition. Figure 4.7 depicts this aspect of the system's physics.

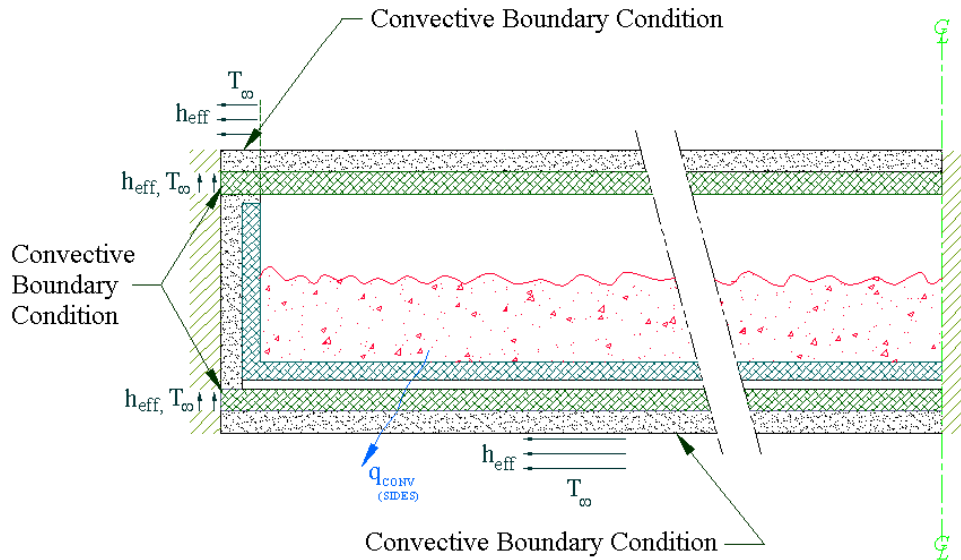


Figure 4.7 Convective Boundaries and Lumped Contribution

The top, bottom, and end surfaces, as well as the sides of the vaporization source, experience convection heat transfer to the adjacent cooling jacket. The only exception to this condition is the right boundary of the symmetry-simplified model, which will be discussed in further detail in section 4.2.1. To incorporate this convection effect, an effective heat transfer coefficient or film coefficient was computed from equation 2.4 of section 2.3.2:

$$Nu = \frac{hL}{k}. \quad [2.4]$$

In the case of the surrounding water jacket, the characteristic length,  $L$ , is defined as the hydraulic diameter of the water passage,  $D_h$ . The relation for the hydraulic diameter,  $D_h$ , of a channel of rectangular cross-section is:

$$D_h = \frac{4A_{cs}}{P_w}, \quad [4.3]$$

where,  $P_w$  is the wetted perimeter of the passage and  $A_{cs}$  is the cross-sectional area of the conduit. For the passages comprising the cooling jacket in question, the hydraulic diameter was calculated to be  $0.015m$ . The thermal conductivity of the fluid under experimental conditions may be found as a tabulated value. For the vaporization source of interest, this medium is water, having a bulk mean temperature of approximately  $20^\circ C$ , and an approximate mean velocity of  $0.4 \frac{m}{s}$ . A fluid thermal conductivity of  $0.613 \frac{W}{m \cdot K}$  was utilized for this investigation (Incropera & DeWitt, 1990). The Nusselt Number,  $Nu$ , was determined from the average of the correlations by Gnielinski and Dittus-Boelter, respectively:

$$Nu_{D_h} = \frac{\left(\frac{f}{8}\right)(Re_{D_h} - 1000)Pr}{1 + 12.7\left(\frac{f}{8}\right)^{1/2}\left(Pr^{2/3} - 1\right)}, \quad [4.4]$$

$$Nu_{D_h} = 0.023 Re_{D_h}^{4/5} Pr^n. \quad [4.5]$$

In these equations,  $f$  represents the Moody friction factor of 0.026 within the passage;  $Re_{D_h}$  is the nondimensional Reynold's number based on diameter (hydraulic);  $Pr$  indicates the nondimensional Prandtl number for the fluid, 5.83 for water at these conditions; and  $n$  is 0.4 for heating and 0.3 for cooling (Incropera & DeWitt, 1990).

Note that the Reynold's number based on diameter takes the form:

$$Re_{D_h} = \frac{u_m D_h}{\boldsymbol{n}} = \frac{\boldsymbol{r} u_m D_h}{\boldsymbol{m}}, \quad [4.6]$$

where  $u_m$  is the mean fluid velocity,  $D_h$  is the diameter (hydraulic diameter) of the passage,  $\boldsymbol{n}$  is the kinematic viscosity of the fluid, and  $\boldsymbol{m}$  is the dynamic viscosity of the fluid. From the computations detailed within Appendix C, the Gnielinski correlation yielded a Nusselt number of  $Nu_D = 40.1$ , whereas, the Dittus-Boelter correlation produced  $Nu_D = 53.4$ . Utilizing these correlations and equations 2.4 and 4.3 above, an approximate effective convection coefficient for the water of  $h_{eff} = 1900 \frac{W}{m^2 K}$  was determined by averaging the results from these correlations. Sections 5.1.2 and 5.2.3 explain the adaptation and utilization of convection and  $h_{eff}$  within the forthcoming analytical and numerical development.

#### 4.1.4 Evaporative Heat Loss

The final significant physical occurrence within the experimental vaporization source is that of evaporative cooling. Wherein, a portion of the system of interest is cooled by the vaporization of the evaporant. Evaporation within a vaporization source holds two

implications for heat transfer. Primarily, the phase change from solid to vapor, or from liquid to vapor, is significantly endothermic. Thus, the physical transformation occurring within the evaporant vessel yields a cooling effect upon the system. Secondly, considering the system's design intent, this vaporized material subsequently leaves the confines of the source. Therefore, a decrease in thermal mass occurs as physical mass is lost from the system of interest.

Traditionally, this mechanism is addressed using the mass flow of vapor from the system and the latent heat of vaporization of the material being vaporized. Allusion to this methodology was made in equation 2.11 of section 2.3.5:

$$q_{evap} = \dot{m}_{evap} h_{fg}, \quad [2.11]$$

where  $q_{evap}$  denotes the rate of heat loss from the system and  $\dot{m}_{evap}$  represents the mass flow rate from the system. Thus, if the mass flow rate of evaporant from the system may be measured or computed, and the latent heat of vaporization may be determined from experiment or tabular data, the heat transfer rate resulting from this vaporization mechanism may be ascertained.

Tabular empirical data regarding the latent heat of vaporization of the evaporant material is, in the author's experience, most difficult to obtain. Furthermore, calculation of the rate of migration of mass from the system is partially dependent upon an arbitrary assumption of coating efficiency, the ratio of vaporized material to condensed coating on the substrate. Thus, the method outlined above is of little use in this investigation. Consequently, an improved treatment of the evaporative contribution, exploiting latent and sensible heats, is detailed in the *Treatment of Evaporative Contribution* part of section 4.2.6.

## 4.2 Modeling of Physical System

Creating an accurate numerical representation of an actual physical system requires that many decisions be made discerning the relative importance or computational relevance of numerous aspects of the physical problem. Often, these engineering judgments are manifested as mathematical or physical assumptions and simplifications.

### 4.2.1 Symmetry

An often utilized and highly effective simplification of physical problems is the exploitation of geometric symmetry. Many large or complex systems may be reduced to manageable form by taking advantage of geometric symmetries. Often, the expanse of a problem may be reduced by a minimum of 50% by analyzing merely one-half of the symmetric system. The experimental system of interest exhibits such a symmetric configuration. The subject vaporization source is symmetric about a line orthogonal to its longitudinal axis located midway between its ends, see Figure 4.8 below.

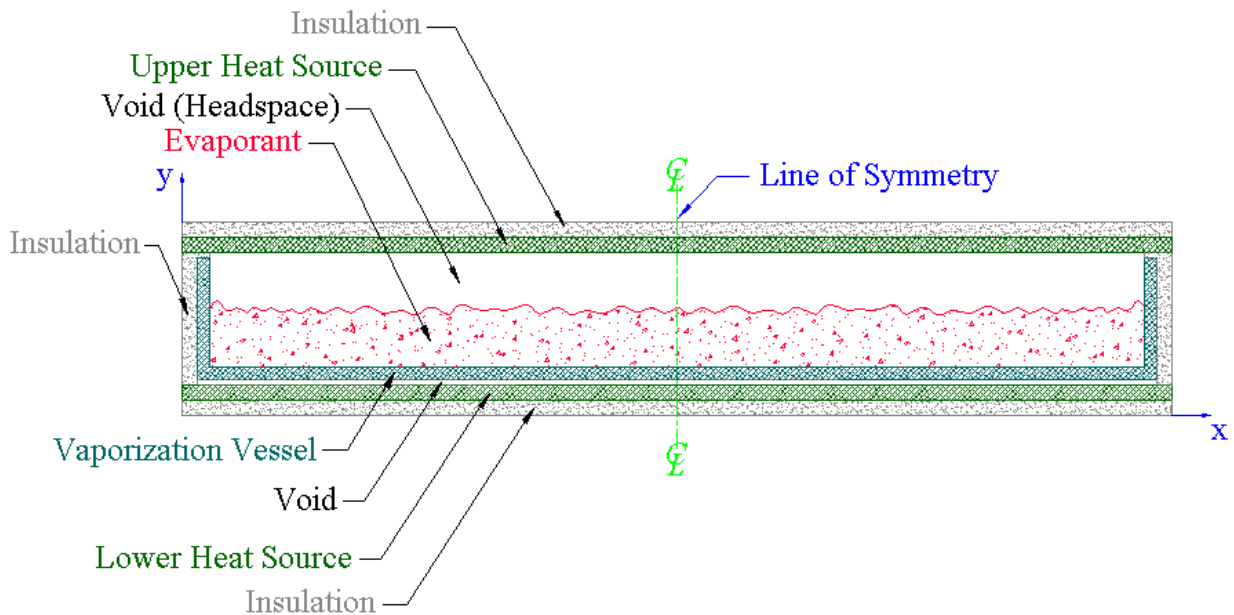


Figure 4.8 Schematic of Entire System Prior to Invoking Symmetry

Thus, the problem of analyzing this physical system may be halved in both physical and numerical size by analyzing one-half of the symmetric whole. With regard to the modeling implications of this simplification, the line of symmetry becomes an adiabatic boundary, see Figure 4.9 below. Such a refinement is both physically and mathematically accurate; it imparts no error of approximation to the analytical or numerical solution, except that, in reality, the physical system is not ideally symmetrical.

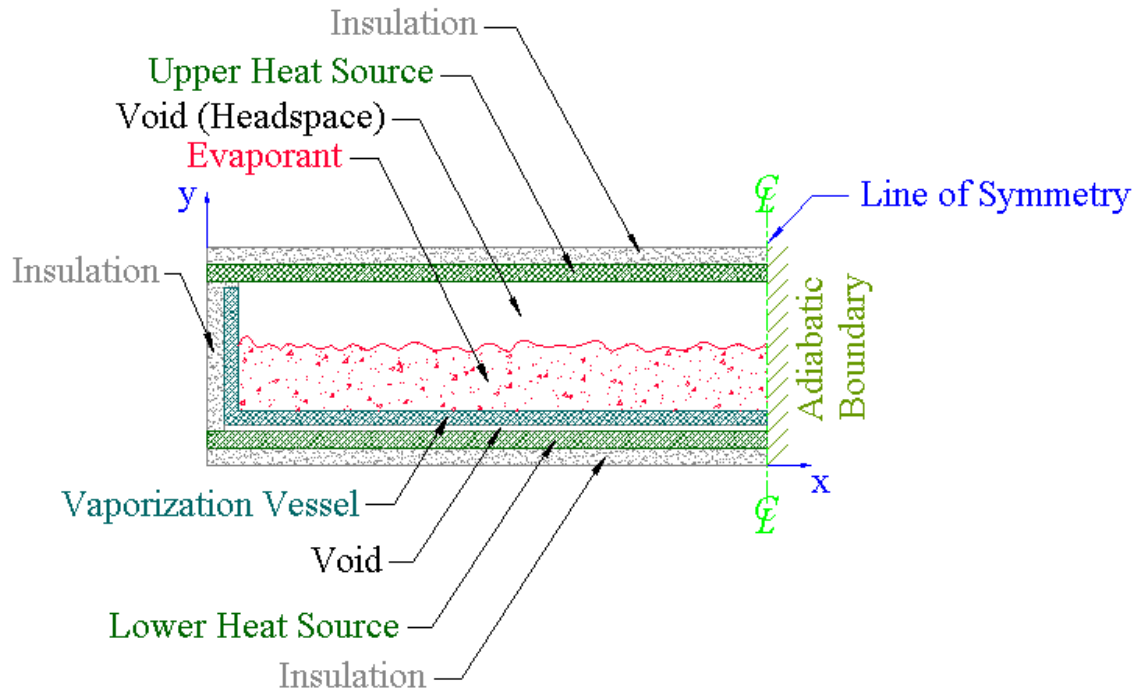


Figure 4.9 Application of Symmetry to Full System

## 4.2.2 Internal Radiation

The experimental vaporization system modeled within this investigation operates, as noted, within an ambient vacuum environment. This environment, in conjunction with the system's construction, demands that radiative heat transfer play a major role in the system's operation. Although two modes of radiation exist within the system, the first to be discussed is that of internal radiation. This thesis considers radiative heat transfer among regions internal to the physical system of interest as "internal" radiation. In that,

radiative heating or cooling of an internal surface or volume, where heat is exchanged with a complementary internal surface or volume, qualifies as internal radiative heat transfer. Refer to Figs. 4.3, 4.4, and 4.5 for visualization.

The regular and fully rectangular configuration is a convenient feature of the physical vaporization source under consideration. In addition to aiding the discretization scheme to be discussed later, this quality lends itself to relatively simple modeling of internal radiation. Furthermore, noting that the ratio of surface length to separation distance is, in one case 80, and in the other 230, a rather simplistic model of internal radiation is employed.

Specifically, considering the narrow spacing of the acting surfaces, internal radiation is assumed to behave in a strictly columnar fashion. Radiant energy emitted from one control volume surface is presumed to travel in a purely vertical direction, falling incident upon the complementary control volume surface above or below. Figure 4.10, below, illustrates this notion of internal radiation.

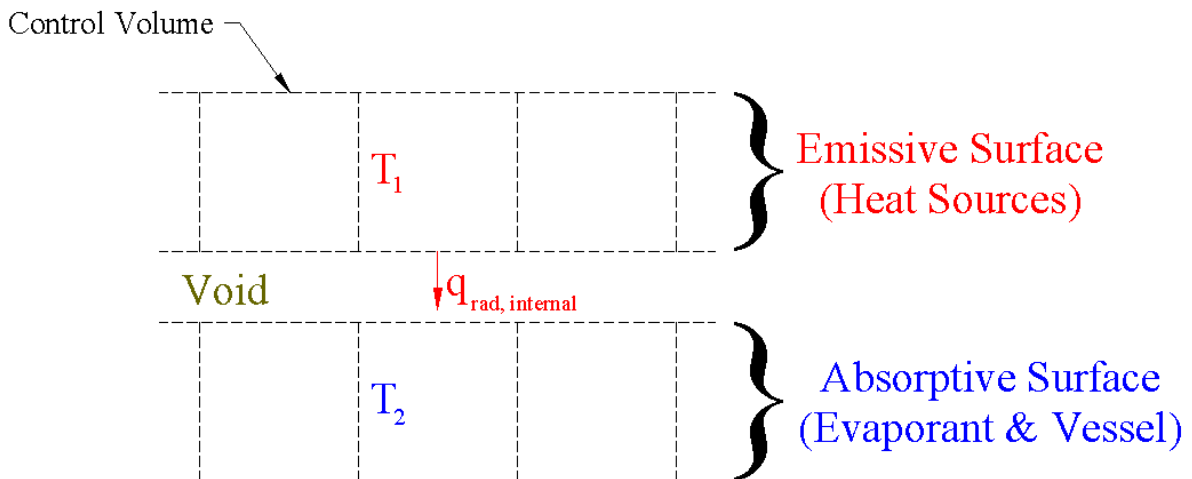


Figure 4.10 Schematic of Columnar Internal Radiation

In this manner, equation 4.1 is applied individually to each surface of a complementary control volume pair undergoing internal radiation.

$$q_{rad,internal} = \frac{\mathbf{s}A(T_1^4 - T_2^4)}{\frac{1}{\mathbf{e}_1} + \frac{1}{\mathbf{e}_2} - 1} \quad [4.1]$$

Hence, a control volume surface within the upper heat source emits radiant energy to only the evaporant control volume surface directly beneath. Concurrently, this evaporant control volume absorbs radiant energy solely from its complementary control volume directly above within the upper heat source. Control volumes bounding the radiant surfaces of the lower heat source and vaporization vessel are assumed to operate using the same mechanism. However, realize that in the case of the lower heat source / vaporization vessel pair, the emissive and absorptive surfaces are reversed in elevation. Thus, during heating, radiant energy follows in an upward path from the lower heat source, and a downward path from the upper heat source.

This method of modeling internal radiation offers a significant benefit to the ensuing development. Beyond the evident simplicity, this columnar approach provides an assurance that energy is conserved among participant control volumes. In that, the construction of the internal radiation model necessitates that all energy leaving the emissive control volume is absorbed by its complementary control volume, either above or below. This mathematical convenience is shown in equation 4.7 below.

$$q_{rad,internal} \Big|_{\substack{\text{EMISSIVE} \\ \text{SURFACE}}} = \mathbf{s}A(T_1^4 - T_2^4) = -q_{rad,internal} \Big|_{\substack{\text{ABSORPTIVE} \\ \text{SURFACE}}} \quad [4.7]$$

Thus, the internal radiation model utilized throughout this investigation is inherently obedient of the First Law of Thermodynamics.

Note that this assumption dictates that the surface emissivities,  $\mathbf{e}_1$ , and  $\mathbf{e}_2$ , are taken to be unity. Obviously, this scenario is not fully descriptive of the physical

phenomenon of internal radiation. Improved methodologies for handling this mechanism will be covered in Chapter 7.0. However, for the purposes of this project, this method serves to address this important mechanism without incurring the development of an internal radiation model equitable in complexity to the scope of the current investigation.

### 4.2.3 External Radiation

As noted in the foregoing section, the vaporization system of interest experiences two forms of radiative heat transfer. This second process is external radiation, or radiative heat transfer with the surroundings. Noting that the experimental system is located within a vacuum chamber of significant volume, an assumption or simplification as to the nature of the radiation exchange between these two bodies may be utilized. Considering the large disparity between the size of the two bodies concerned, e.g. the vacuum vessel is orders of magnitude more voluminous than the vaporization source, the radiative transfer may be closely approximated as that of a small object within a large enclosure. This relationship is portrayed, for the net radiative heat transfer at a surface, by the equation:

$$q_{rad} = \mathbf{se}A(T^4 - T_{surr}^4). \quad [4.8]$$

With regard to the numerical model of the physical vaporization source, an external radiation boundary condition is imposed at the upper surfaces of the discretized region. As previously mentioned, Figure 4.6 depicts the radiative boundary condition present and its respective location.

Acknowledging the small object / large enclosure simplification specified above, and the material of construction of the surface involved, the externally emissive surface of the vaporization source is of an undisclosed proprietary material having an approximate emissivity of 0.95.

The enclosure assumption and emissivity discussed above are then incorporated within the linearized radiation form from section 2.3.3:

$$q_{rad} = h_r A(T - T_{surr}), \quad [2.7]$$

where it was introduced that  $h_r$  is the radiation heat transfer coefficient, given by:

$$h_r = \mathbf{se}(T + T_{surr})(T^2 + T_{surr}^2), \quad [2.8]$$

Note that in this form, the large enclosure assumption has been applied. Hence, radiative heat transfer occurring at the upper boundary of the physical system may be properly accounted in a manageable, linear form similar to convection.

#### 4.2.4 Lumping in z-Direction

The physical vaporization source is a three-dimensional entity. However, the thermal behavior of the entire system, although interesting, is only relevant to production uniformity in consideration of the  $x$ - and  $y$ -directions. Refer to Figure 4.9 which portrays  $x$  as the longitudinal axis,  $y$  as the minor axis, and by nature of the right-hand convention, the  $z$ -axis protrudes from the page. Concisely, this investigation, and the inherent numerical model, neglects thermal gradients in the  $z$ -direction, as they have negligible effect on product outcome. In so doing, the ensuing analysis is lumped in the  $z$ -direction. That is, the temperature is assumed uniform in that particular direction. In reality, temperature gradients do exist in this direction within the vaporization source. However, the effect of these gradients on the crux of this investigation is minimal and is therefore assumed to be negligible.

Despite neglecting thermal gradients in the  $z$ -direction, surface effects strongly influencing the behavior of the system are incurred at both of the boundaries in this direction. A problem is then presented in handling these critical modes of heat transfer

while preserving both the two-dimensionality and the mathematical rigor of the mathematical and numerical models. Specifically, these surface effects may not simply be applied directly to the nodes with which indirect interaction would occur. The composite result of these surface phenomena, acting through the proper strata, must be applied to the correct nodes.

To accomplish this goal, a resistance network representing the physical system's construction along the  $z$ -direction is formulated. Figure 4.11 exemplifies the resistance network employed.

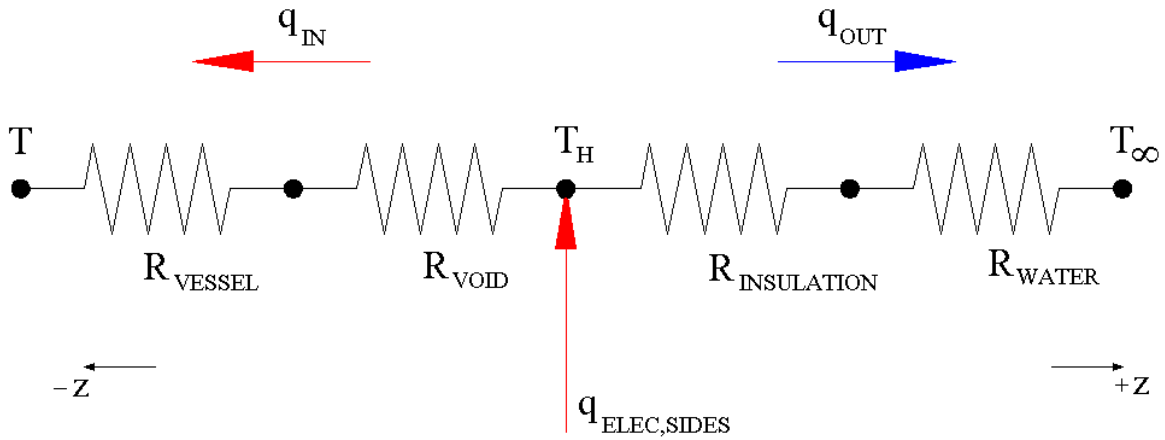


Figure 4.11 Equivalent Resistance Network, Lumping in  $z$ -Direction

Performing an energy balance on the node representing the lateral portion of the lower heat source yields three equations correlating temperature and heat input. Manipulating the equation describing the portion of heat added to the system,  $q_{in}$ , and the overall equation describing the heat input to the  $z$ -direction network, an equation explicit in temperature may be obtained for  $q_{in}$ :

$$q_{in} = \frac{\left[ \frac{q_{ELEC,SIDES} + \frac{T_{\infty}}{R_{OUT}} + \frac{T}{R_{IN}}}{\left( \frac{1}{R_{IN}} + \frac{1}{R_{OUT}} \right)} \right] - T}{R_{IN}}, \quad [4.9]$$

where,  $q_{ELEC,SIDES}$  represents the power input applied laterally to the system by the lower heat source,  $T_{\infty}$  signifies the temperature of the water coolant,  $T$  symbolizes the nodal temperature,  $R_{IN} = R_{VOID} + R_{VESSEL}$ , and  $R_{OUT} = R_{INSULATION} + R_{WATER}$ . These relations are covered in depth within Appendix D, which details the derivation of  $q_{in}$  in terms of equivalent network resistances. Thus, the correct proportion of heat from the lateral parts of the lower heat source is correctly applied to the effected nodes.

#### 4.2.5 Treatment of Voided Regions

One particularly interesting characteristic of the experimental system and its developing model is the existence of regions within the source that are almost entirely devoid of mass. Recalling that the ambient environment is that of a high vacuum having ambient pressure on the order of  $10^{-5} Torr$ , the absence of insulation, heat sources, evaporant, or other materials dictates the absence of mass. On a macroscopic scale, no ambient fluid, such as air, fills this space. It is relevant to note that molecular flow exists within a high vacuum system. However, the small quantity of mass and minimal molecular conduction imparted to this problem are deemed negligible.

The significance of these voided regions becomes obvious in the consideration of the property of thermal capacitance and the mechanism of conduction. Thermal capacitance quantifies the ability of a material to absorb and retain thermal energy. This quality is largely dependent upon the density and specific heat capacity of the material. Quite simply, in the absence of matter, no thermal capacitance can exist. Similarly, the presence of matter is paramount to the existence of thermal conduction. Without intimate thermal contact, between both moving atoms and material surfaces, thermal conduction is nonexistent.

The implications of a regional lack of matter within the evolving model are certainly noteworthy. Specifically, as one might deduce from the foregoing information,

the absence of matter necessitates the *absence of temperature*. A domain having no mass can possess no thermal capacitance, nor can it conduct thermal energy. Therefore, this region cannot logically have a temperature. In this regard, a mathematical discrepancy between the concept of *no temperature* and *zero temperature* arises. Wherein, *no temperature* implies the aforementioned absence of mass and temperature; *zero temperature* indicates a measured temperature of zero in reference to an established standard. The two differ significantly.

With respect to conduction, the mechanism upon which this numerical method is based, *no temperature* dictates the lack of a temperature gradient associated with the voided domain. Yet, *zero temperature* results in a temperature gradient suitable for thermal conduction to exist. Thus, a means of compelling zero conduction to or from this domain is required. This objective is achieved via nodal property assignments. Specifically, all voided regions are assigned a null property set. Density and specific heat capacity are specified as  $0 \frac{kg}{m^3}$  and  $0 \frac{kJ}{kg \cdot K}$ , respectively. Thermal conductivity is stipulated to be an infinitesimally small number,  $k = 10^{-100} \frac{W}{m \cdot K}$ . The discussion of the interface conductivity in section 5.2.3 will address the reason for a nonzero thermal conductivity. Hence, a zero mass ( $\rho = 0$ ), zero thermal capacitance ( $C_p = 0$ ), and zero conduction ( $k \rightarrow 0$ ) condition is imposed to accurately replicate the voids present within the actual vaporization source.

#### 4.2.6 Treatment of Evaporative Contribution

As previously noted, a significant physical aspect of the experimental system is that of the evaporative cooling contribution imparted by the system's design intent. Although, a traditional, straightforward approach, such as that outlined in section 2.3.5, exists for the incorporation of such a phenomenon, an alternate, more germane, treatment was adopted for this investigation. Conveniently, this methodology is doubly beneficial to this project.

The *Evaporant Properties* subsection of 3.2.4 discusses the development of a temperature dependent function that describes the heat capacity of the vaporization material. Fortuitously, this information incorporates the evaporative mechanism currently at issue. In that, as it spans a range that includes the evaporant's vaporization temperature, the DTA outlined above measures not only the sensible energy required to heat the material to its transformation temperature, but also the latent heat required to induce any physical or chemical transformations. Appendix B contains the raw DTA data plot obtained. Figure 4.12 graphically illustrates the concept of sensible and latent heat in the phase transformation of a pure substance. Therefore, the total heat capacity established in section 3.2.4 inherently accounts for both the specific heat capacity of the material and the evaporative cooling contribution yielded by the latent heat of vaporization or sublimation.

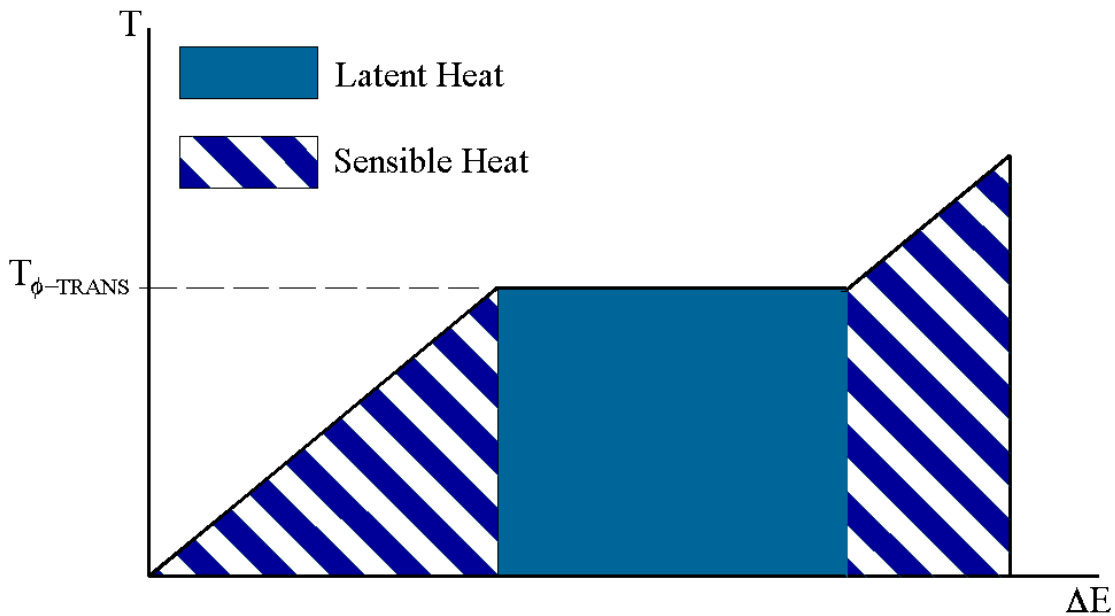


Figure 4.12 Schematic Illustrating Latent and Sensible Heat

Hence, as areas containing evaporant are heated, their response is governed by the heat capacity function  $C_p(T)$ , equation 3.3, which accounts for vaporization.

A further trait of vaporization which is key to the physical accuracy of the evolving model is the depletion of evaporant mass during operation of the vaporization source.

Observing the experimental system, one notes that, expectedly, the mass of evaporant decreases significantly over the duration of each run. Therefore, the necessity of simulating this decrease in physical and thermal mass is pertinent to the physical significance of the model and subsequent numerical solution. Thus, the procedure adopted to address the existence of voids within the system is utilized to replicate the depletion of evaporant during operation.

Simulation of the subsequent evolution and loss of evaporant, then, is accomplished by a numerical flag denoting the attainment of the maximum temperature for which  $C_p(T)$  for the evaporant is defined, approximately 1500°C. At this point evaporant at this node is assumed to be completely vaporized and nodal properties are reset to those of a voided region. Hence, having no density, specific heat, nor conductivity, the absence of evaporant mass in this region is accurately replicated.

A final noteworthy aspect to evaporant depletion involves ever-important internal radiation. As previously discussed, the modeling of internal radiation is dependent on the interaction of complementary control volume surfaces. During operation, the physical and numerical representation of these particles “disappear” from the system. Therefore, the numerical model must dynamically detect the most proximal complementary node still present within the model. Hence, a search routine is implemented to determine the correct complementary evaporant node with which to exchange heat energy. Please refer to forthcoming section 5.1.2 for the treatment of internal radiation within the framework of the source term.

# Chapter 5.0

## Numerical Solution

### 5.1 Formulation of Governing Equation

To formulate a mathematical problem from the fundamental physics discussed in the foregoing sections, a derivation of the applicable equation(s) describing the behavior is essential.

#### 5.1.1 The Energy Equation

The most rigorous treatment of this process would derive the conduction equation from an energy balance on a control volume, which is a rather lengthy and detailed process. Poulidakos presents an excellent example of this formulation in Conduction Heat Transfer (1994). A more abbreviated construction, however, may begin with the incompressible energy equation:

$$\rho C_p \left( \frac{\partial T}{\partial t} + \vec{V} \cdot \nabla T \right) = \nabla \cdot (k \nabla T) + S. \quad [5.1]$$

In this fashion,  $\vec{V}$  is the velocity of the system with regard to the control volume,  $S$  signifies the rate of internal energy generation, and  $\nabla$  is the gradient operator for vector mathematics. Noting that the system of interest is motionless with respect to an arbitrary control volume within,  $\vec{V} = 0$ , and equation 5.1 reduces to:

$$\rho C_p (T) \frac{\partial T}{\partial t} = \nabla \cdot (k \nabla T) + S(T). \quad [5.2]$$

Transforming to cartesian notation, equation 5.2 becomes the familiar:

$$\rho C_p \frac{\partial T}{\partial t} = \frac{\partial}{\partial x} \left( k \frac{\partial T}{\partial x} \right) + \frac{\partial}{\partial y} \left( k \frac{\partial T}{\partial y} \right) + S. \quad [2.13]$$

This relation is the foundation for both Patankar's and Vick's development of the form of the conduction equation employed herein. The term  $S$  is then referred to as the "source" term (Patankar 1991, Vick 1998). The source term,  $S$ , is defined as containing both a constant and proportional part,

$$S = Sc(x, y, t) - Sp(x, y, t) T, \quad [5.3]$$

where  $Sc$  represents the constant portion, and  $Sp$  symbolizes the proportional component. Substituting definition of equation 5.3 into equation 2.13 results in:

$$\rho C_p \frac{\partial T}{\partial t} = \frac{\partial}{\partial x} \left( k \frac{\partial T}{\partial x} \right) + \frac{\partial}{\partial y} \left( k \frac{\partial T}{\partial y} \right) + Sc(x, y, t) - Sp(x, y, t) T. \quad [5.4]$$

This is the form of the conduction, or energy, equation that will be utilized in the development of a suitable analytical problem depicting the vaporization source of interest.

### 5.1.2 Formulation of the Source Term

Equation 5.4 lends itself to preparation for numerical solution. The utilization of the source term permits the accurate treatment of numerous thermal inputs and outputs. Popular examples include internal generation, convection, and radiation. Within this investigation, the formulation of the source term includes all of these mechanisms.

## ***Internal Radiation***

Heat transfer by radiation among two surfaces internal to the vaporization source is paramount to the operation of both the experimental system and the evolving model. As noted earlier, the presence of this mode of transfer is essentially a product of the system design. Figure 4.3, within the *Internal Radiation* subsection of section 4.1.2, illustrates those surfaces participating in internal radiation.

Section 4.1.2 details the physical significance of internal radiation within this investigation. It is now pertinent to explore the adaptation of this mechanism to the mathematical or analytical problem construction. As discussed, the benefit of the conduction equation containing the two-part source term is that it is well suited to this modification. Recall that equation 5.3 contains both constant and proportional components that may be space- and / or time-dependent:

$$S = Sc(x, y, t) - Sp(x, y, t)T. \quad [5.3]$$

Additionally, section 4.2.2 offered a model of internal radiation utilizing equation 4.7.

$$q_{rad, internal} \Big|_{\substack{\text{EMISSIVE} \\ \text{SURFACE}}} = \mathbf{s}A(T_1^4 - T_2^4) = -q_{rad, internal} \Big|_{\substack{\text{ABSORPTIVE} \\ \text{SURFACE}}} \quad [4.7]$$

To preclude any nonlinearities, equation 4.7 is evaluated for each node in an explicit fashion. This value for  $q_{rad, internal}$  is then included as a portion of the constant source term component,  $Sc$ .

Thus, the temperatures utilized in the computation of  $q_{rad, internal}$  are one time step old. For relatively small time-steps, this time-lagging method imparts little error to the solution, while affording a linear solution scheme. An alternative involves a nonlinear, iterative process to arrive at a converged solution for  $q_{rad, internal}$  at each node, at each time

step. Such a method is a time-consuming and computationally expensive endeavor that offers dubious contribution to this investigation in terms of accuracy.

### ***Internal Generation***

Since the heat sources utilized in the physical system are resistance heaters, electrical power dissipation as internal heat generation plays a crucial role in this investigation. Yet, the modeling and implementation of this phenomenon is straightforward. As noted in section 4.1.1, power is supplied to the upper and lower heat sources following a stepped input schedule. Therefore, the numerical simulation includes this behavior in the ever-useful source term. Due to the discretized nature of the solution, the power input is dynamically evaluated at the beginning of each time-step. In this fashion, power input to both upper and lower heat sources is constant over any time step. This trait allows the incorporation of power dissipated as heat within the constant portion of the source term,  $Sc$ . Observing the volumetric units of the source term, all that remains to fully implement heat input is the distribution of power over each heat source's respective volume. Thus, the upper heat source distributed source term takes the form:

$$Sc_{elec,upper} = \frac{q_{elec,upper}}{V_{upper}}. \quad [5.5]$$

Similarly, for the lower heat source the following applies:

$$Sc_{elec,lower} = \frac{2}{3} \frac{q_{elec,lower}}{V_{lower}}, \quad [5.6]$$

where  $V_n$  represents the respective source volume. Note that  $\frac{1}{3}q_{elec,lower}$  is yet unaccounted for; this portion of the lower heat source input is addressed in the following *Convection* subsection.

## Convection

In much the same vein as the lumped portion of the power input to the lower heat source is managed, so too is the lumped convection contribution due to the lateral portion of the water jacket. Drawing on section 4.2.4, and equation 4.9, the contribution due to convection at the lateral, or  $z$  boundaries, is managed within this relation by the quantity of  $q_{ELEC,SIDES}$  that enters the system as  $q_{in}$ . Furthermore, as presented in section 4.2.4, this equation also encompasses the effect of convection at the  $z$  boundaries of the system. Having previously modeled the effect of convection and lateral heat input, these phenomena will now be framed as constant and proportional constituents of the source term. Grouping like terms, constants and those proportional to  $T$ , performing the requisite algebraic manipulations, and dividing terms by affected volumes, both components of the source term are revealed. Specifically, equation 5.7 portrays the constant part, while equation 5.8 describes the proportional quantity.

$$Sc_{elec,lumped} = \frac{\left( \frac{\frac{1}{3} q_{elec,lower} R_{OUT}}{R_{IN} + R_{OUT}} \right) + \left( \frac{T_{mean}}{R_{IN} + R_{OUT}} \right)}{V_{lower,lumped}}, \quad [5.7]$$

$$Sp_{elec,lumped} = \frac{\left( \frac{1}{R_{IN} + R_{OUT}} \right)}{V_{lower,lumped}}, \quad [5.8]$$

Thus, all lumped contributions may be accurately applied to each effected node utilizing the concept of the source term.

## **5.2 Discretization of Governing Equations**

The final phase in the numerical modeling of a given system is the selection and implementation of a numerical method for equation solution. From those methods foregoing within the Literature Review, the Finite Difference Method is selected for use in this investigation, in light of its relative simplicity and applicability to rectangular geometry.

Within this methodology, several subclasses describe the types of temporal and spatial discretization to be employed. Each discretization method offers specific advantages and disadvantages, depending on the intended application. Two common time discretization schemes and two control volume discretization practices are considered in selecting an overall numerical method for this investigation.

### **5.2.1 Time Discretization**

In general, most time discretization schemes are variations or modifications of two basic types: the explicit method and the implicit method. Explicit discretization involves the solution of discretization equations at a particular node using surrounding nodal temperatures from the previous time step. In this manner, the solution is explicit in temperature; the nodal temperature of interest is a function of the known surrounding temperatures at each time step. This technique is advantageous in its convenience and simplicity as solutions may be readily computed at each ensuing time step. However, drawbacks in stability and computational inefficiency make this method less than desirable for this investigation.

As one might expect, the implicit discretization scheme entails the evaluation of surrounding nodal temperatures at the current time, rather than the previous time step. In this fashion, since the current time step has yet to be evaluated, all nodal temperatures are unknown. Solution methodology for the resulting system of equations must then be

simultaneous; iterative numerical methods, such as Gauss-Seidel iteration, or direct solvers, such as matrix inversion or LU-decomposition, are commonly employed in the solution of such problems.

Although seemingly more complex and time consuming, the implicit time-discretization method surpasses the explicit method in both computational efficiency and stability. As in the foregoing allusion, time steps utilized by the explicit method must be carefully chosen to be of a sufficiently small magnitude to maintain stability. Hence, since the implicit design is unconditionally stable, the chosen size of the time increment may be adjusted to desirably affect solution efficiency, while maintaining sufficient accuracy. Consequently, the resulting quantity of computations required to achieve an explicit solution generally outdistances the required solution time of an iterative implicit solution (Incropera & DeWitt, 1990). For these reasons, unconditional stability and computational efficiency, the implicit method of time-discretization was selected for this investigation.

### **5.2.2 Spatial Discretization**

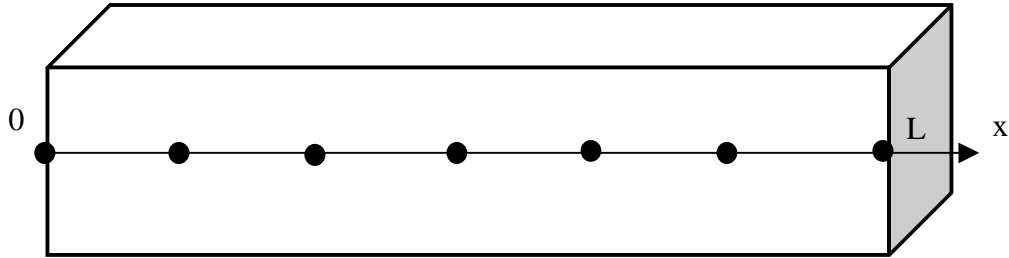
In conjunction with the temporal methodologies outlined above, two approaches to control volume or spatial discretization are also considered in the design of this investigation. As described by Patankar in his text and Vick in his adaptation, these methods will likewise be termed “Practice A” and “Practice B” (Patankar, 1991 and Vick 2000).

#### ***Practice A***

In Practice A, the grid point locations are selected first. A grid point is placed on each boundary of the region and adjacent internal grid points are inserted using any uniform or non-uniform spacing. Next, the control volume boundaries are drawn at exactly the midpoint between grid points. This results in a grid system where control

volume boundaries lie midway between nodes; nodes do not necessarily fall midway between control volume faces, and a half-thickness control volume is generated at each boundary (Patankar, 1991). Figure 5.1 illustrates the Practice A method of spatial discretization.

Specify nodal locations first.



Locate control volume faces between nodes.

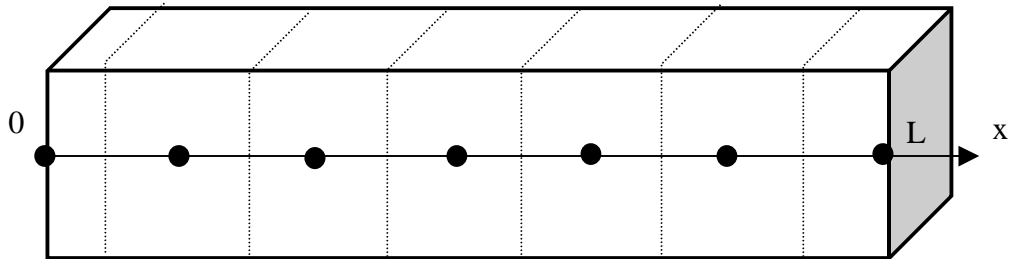


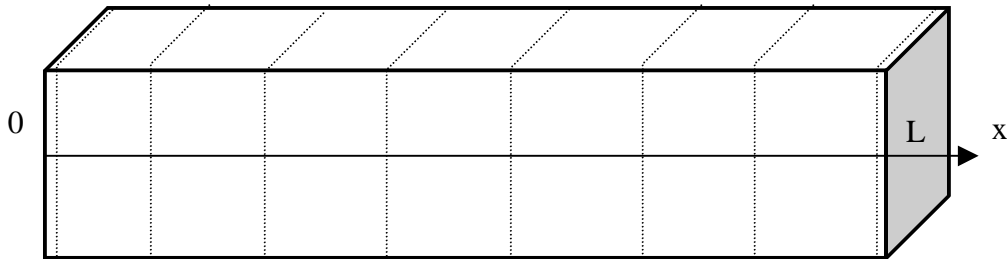
Figure 5.1 Practice A Discretization (Courtesy Vick, 2000)

### ***Practice B***

In contrast to Practice A, Practice B dictates that the control volume locations be decided first. As with the grid selection of Practice A, the control volume selection in Practice B may be either uniform or non-uniform. A control volume face is placed at each boundary within the region of interest and the desired number of volumes are specified within the region according to the chosen spatial distribution. In this technique, the nodes are located midway between the control volume faces. In this fashion, the boundaries are

enclosed by zero-width control volumes rather than the half-width volumes of Practice A (Patankar, 1991). Figure 5.2 depicts the discretization of a simple region using Practice B.

Specify control volume face locations first.



Place nodes at control volume centers.

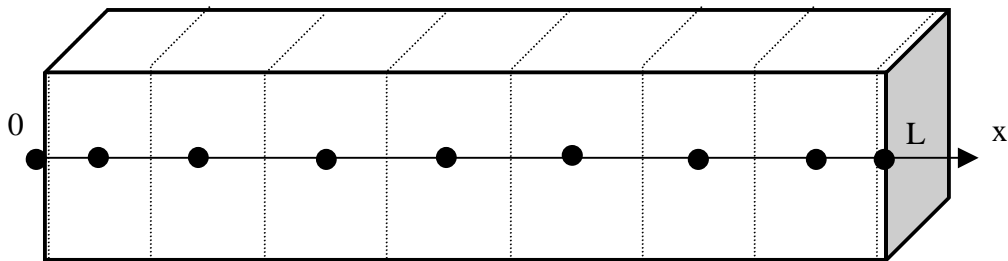


Figure 5.2 Practice B Discretization (Courtesy Vick, 2000)

### *Selection of Method*

Practice A may often be utilized in the discretization of one-dimensional problems because of its simplicity. However, in more complex problems, especially those with composite geometries or spatially variant properties, this method is cumbersome and ineffective. In cases such as these, it is desirable to locate a control volume boundary at the interface between different property regions. In this fashion, the control volume properties are preserved as uniform over the volume, with discontinuities occurring only at control volume boundaries. Since the grid points are established before the control volume

boundaries in Practice A, a particular relationship between the number and spacing of grid points and control volumes must be maintained to achieve this scenario (Patankar, 1991).

Such an exercise is inconvenient and computationally inefficient when compared to Practice B. As noted, Practice B disposes of the problem of boundary and discontinuity correspondence. Specifying the control volume faces before the grid points allows the engineer to dictate that a control volume face be coincident with each discontinuity in properties (Patankar, 1991). The experimental vaporization system is composed of several materials, each having unique thermophysical properties. Therefore, owing to its computational and theoretical convenience in handling multi-dimensional problems with spatially variant properties, Practice B is selected as the control volume discretization method within this investigation.

As implemented within the developing numerical model, this discretization practice is framed within a zoned construction. The solution domain is divided into zones in the  $x$ - and  $y$ -directions, using Practice B conventions. Then, the zoned domain is discretized into control volumes, again following the precepts of Practice B, see Figure 5.3 below.

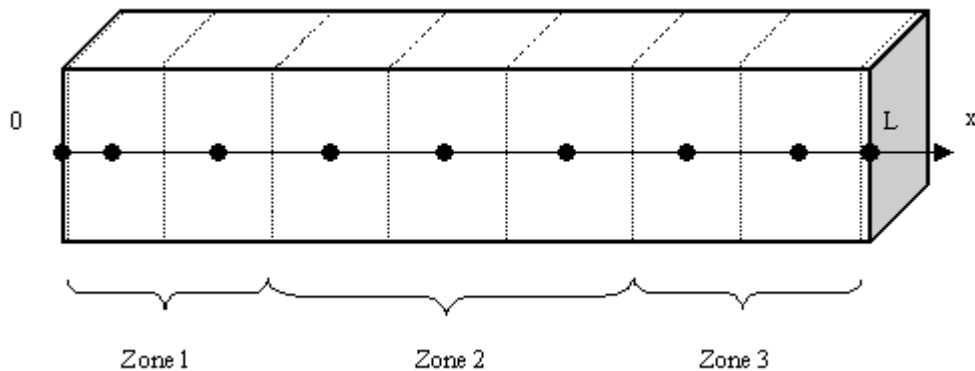


Figure 5.3 Zoned Domain Construction (adapted from Vick, 2000)

The use of zones facilitates the convenient modeling of composite or multi-layered structures such as the physical vaporization source, which comprises varying materials, properties, and source terms. Within the structure of the numerical model, the number of zones in a chosen direction is specified. Then the number of control volumes per zone and

zonal properties are assigned. Figure 5.4 exemplifies a zoning scheme utilized within this investigation.

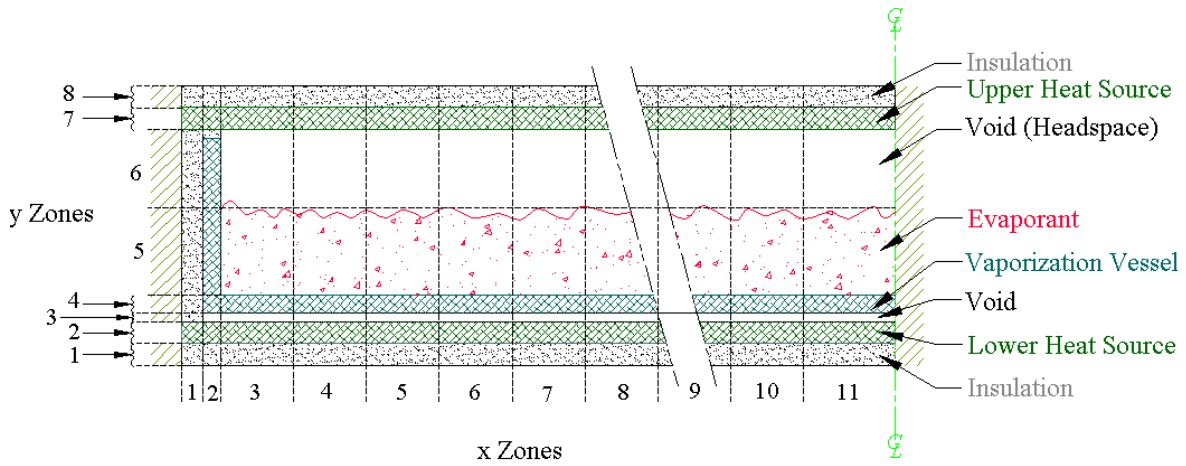


Figure 5.4 Typical Zoning Scheme

### 5.2.3 Development of the Discretized Governing Equation

Recall the governing equation developed within section 5.1.1 has the form:

$$rC_p \frac{\partial T}{\partial t} = \frac{\partial}{\partial x} \left( k \frac{\partial T}{\partial x} \right) + \frac{\partial}{\partial y} \left( k \frac{\partial T}{\partial y} \right) + Sc(x, y, t) - Sp(x, y, t) T. \quad [5.4]$$

Applying Practice B to an arbitrary two-dimensional rectangular domain, Vick depicts a typical interior control volume in Figure 5.5.

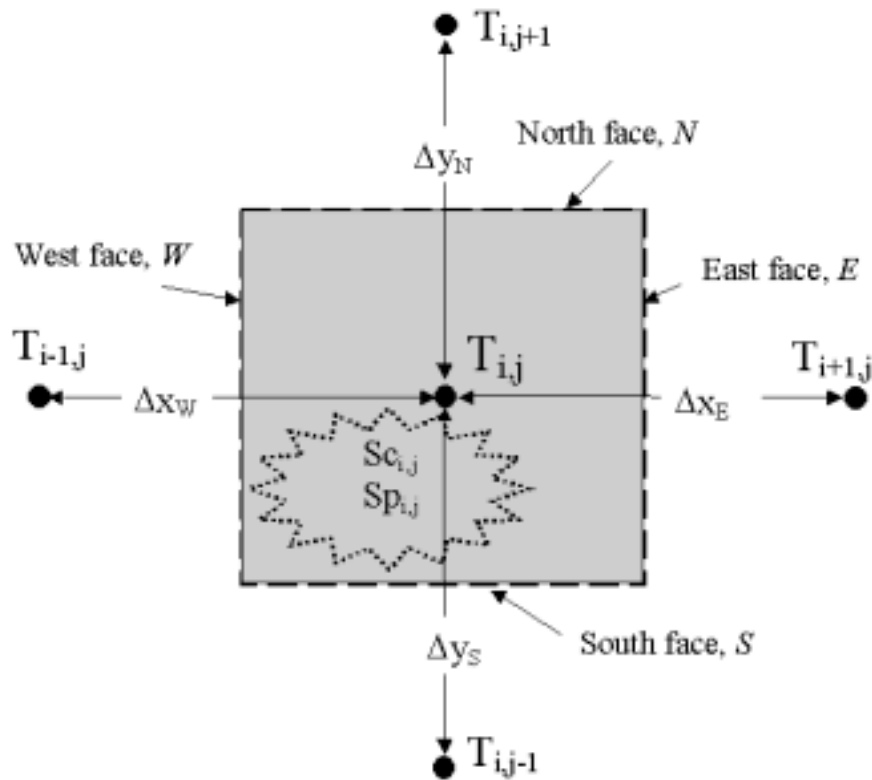


Figure 5.5 Interior 2-D Control Volume, Practice B (Courtesy Vick, 2000)

In this scheme, the node under consideration is depicted as node  $(i, j)$ ; its western, eastern, southern, and northern neighbors are illustrated by  $(i-1, j)$ ,  $(i+1, j)$ ,  $(i, j-1)$ ,  $(i, j+1)$ . The notation  $E$  denotes the east face of the control volume;  $W$ ,  $S$ , and  $N$  represent the west, south, and north faces, respectively. The symbol  $\Delta x_E$  signifies the nodal spacing to the east of the current node,  $\Delta x_W$ ,  $\Delta x_S$ , and  $\Delta x_N$  symbolize the spacing to the west, south, and north, respectively (Vick, 2000).

Having employed the given discretization scheme, the governing equation is now integrated over the time and spatial control volume domains.

$$\int_{t_{p-1}}^{t_p} \int_S \int_W \left[ \underbrace{\frac{\partial}{\partial x} \left( k \frac{\partial T}{\partial x} \right)}_I + \underbrace{\frac{\partial}{\partial y} \left( k \frac{\partial T}{\partial y} \right)}_II + \underbrace{Sc(x, y, t) - Sp(x, y, t) T}_{III} - \underbrace{rC_p \frac{\partial T}{\partial t}}_IV \right] dx dy dt = 0, \quad [5.9]$$

Integrating each of the four terms in a discretized manner, manipulating algebraically, regrouping to form discretization coefficients (conductances), and reassembling results in the General 2-D Conduction Equation:

$$a_{i,j} T_{i,j,p} - aE_{i,j} T_{i+1,j,p} - aW_{i,j} T_{i-1,j,p} - aN_{i,j} T_{i,j+1,p} - aS_{i,j} T_{i,j-1,p} = b_{i,j}, \quad [5.10]$$

where,

$$aE_{i,j} = \frac{k_E \Delta y_{i,j}}{\Delta x_E} = \text{Eastern conductance}$$

$$aW_{i,j} = \frac{k_W \Delta y_{i,j}}{\Delta x_W} = \text{Western conductance}$$

$$aN_{i,j} = \frac{k_N \Delta x_{i,j}}{\Delta y_N} = \text{Northern conductance}$$

$$aS_{i,j} = \frac{k_S \Delta x_{i,j}}{\Delta y_S} = \text{Southern conductance}$$

$$aO_{i,j} = \frac{rC_p}{\Delta t_p} \Delta x_{i,j} \Delta y_{i,j} = \text{Capacity term}$$

$$b_{i,j} = Sc_{i,j} \Delta x_{i,j} \Delta y_{i,j} + aO_{i,j} T_{i,j,p-1} = \text{Explicit part of source and transient terms}$$

$$a_{i,j} = aO_{i,j} + aE_{i,j} + aW_{i,j} + aN_{i,j} + aS_{i,j} + Sp_{i,j} \Delta x_{i,j} \Delta y_{i,j} = \text{Implicit part of source and transient terms}$$

A rigorous derivation of the discretized governing conduction equation is included in Appendix E. Moreover, Vick (2000) provides an excellent development of this entire method for both one-dimensional and two-dimensional steady and transient problems.

## Interface Conductivity

An important feature of this method of discretization is the notion of interface conductivities. These terms,  $k_E$ ,  $k_W$ ,  $k_N$ , and  $k_S$ , define the “mean” conductivity between adjacent nodes. It is critical to note, however, that the term “mean” does not connote the arithmetic mean. Rather the interface conductivity is computed as the harmonic mean of the two neighboring sets of nodal properties. As explained by Vick, this theory is based on the equivalent resistance concept, see Figure 5.6 below.

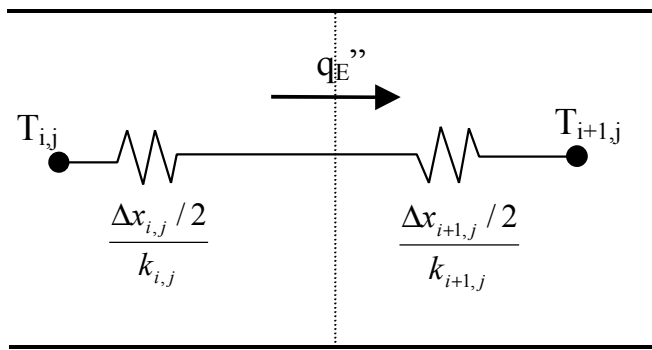


Figure 5.6 Thermal Resistance Network for Interface Conductivity

(Courtesy Vick, 2000)

To derive the harmonic mean interface conductivity, equations for the heat flux,  $q_E''$ , at the interface are written using both the equivalent resistance and finite difference interpretation and equated.

$$q_E'' = \frac{T_{i,j} - T_{i+1,j}}{\frac{\Delta x_{i,j}}{k_{i,j}} + \frac{\Delta x_{i+1,j}}{k_{i+1,j}}} = k_E \frac{T_{i,j} - T_{i+1,j}}{\Delta x_E} = q_E'' \quad [5.11]$$

This form is then solved for the respective conductance, in this case  $aE_{i,j} = \frac{k_E}{\Delta x_E}$ .

Isolating  $k_E$ , the defined interface conductivity, an expression for the interface conductivity as the harmonic mean is revealed:

$$k_E = \frac{2k_{i,j}k_{i+1,j}}{\left(k_{i+1,j} \frac{\Delta x_{i,j}}{\Delta x_E}\right) + \left(k_{i,j} \frac{\Delta x_{i+1,j}}{\Delta x_E}\right)}, \quad [5.12]$$

Similar relations are then determined for the west, north, and southern interfaces (Vick, 2000).

This formulation of the interface conductivity as the harmonic mean offers a unique advantage over the arithmetic mean. Specifically, the harmonic mean better describes limiting behaviors between neighboring nodes. In that, for extremely large disparity between adjacent conductivities, the arithmetic mean yields an interface conductivity approximately equal to half of the dominating conductivity. The harmonic mean gives an interface conductivity of twice the dominating conductivity. Obviously, the harmonic mean more closely simulates actual behavior. Moreover, in the event that one of the conductivities is zero, the arithmetic mean again produces a result of half the dominating (larger) conductivity; the harmonic mean yields an interface value of zero. Most certainly, the result yielded by the harmonic mean is the correct behavior (Vick, 2000). However, note that if both of the conductivities are zero, the harmonic mean yields division by zero. This aspect is, as previously noted, of critical importance in the modeling of voided regions. Despite this drawback, owing chiefly to its superior validity, the harmonic mean construction of interface conductivity is exclusively employed within this analysis.

### ***Boundary and Initial Conditions***

To complete the information required to fully characterize the numerical solution, boundary and initial conditions must be defined. Specifically, information regarding the spatial and temporal constraints of the numerical system is necessary to generate a complete solution.

## Boundary Conditions

With regard to applicable boundary conditions, section 4.1.3 details the specifics of the manifestation of convective boundary conditions within the physical vaporization system. While, sections 4.1.2 and 4.2.3 explain the implications of the radiative boundary condition present at the upper surface of the physical system. These phenomena must now be applied to the discretized conduction equation as boundary conditions.

Consider an arbitrary eastern boundary, with possible specified heat flux or convective boundary conditions. Assigning the coordinates (L,j) to this node and its zero-width control volume, an energy balance at this boundary yields:

$$-k \frac{dT}{dx} = h_L (T_{mean} - T) + q_L'' . \quad [5.13]$$

As Vick illustrates, discretization of this equation produces:

$$-k_{L,j} \frac{T_{L,j} - T_{L-1,j}}{\frac{\Delta x_{L,j}}{2}} = h_L (T_{mean} - T) + q_L'' . \quad [5.14]$$

Introducing discretization coefficients results in:

$$aE_{L,j} T_{L-1,j} + a_{L,j} T_{L,j} = b_{L,j} . \quad [5.15]$$

Similar equations for the boundary conditions may be obtained at the western, northern, and southern boundaries also. Appendix F, adapted from Vick (2000), tabulates the applicable boundary condition coefficients for each boundary by type, including the special case of a specified temperature.

With the development of equations describing the four system boundaries, a system of equations may be assembled by systematically applying equation 5.10 to each interior node, and the proper form of equation 5.15 to each boundary node.

### *Initial Condition*

In the solution of transient problems, the solution obviously requires an initial condition with which to begin. This investigation entails a system heated from ambient, throughout a prescribed heating schedule. As such, the applicable initial condition is a uniform grid temperature of  $300K$  occurring at the initial time value of  $t = 0$ :

$$T_i = 300K \text{ at } t = 0. \quad [5.16]$$

The specific utilization of this data will be evidenced in following sections.

Having a fully discretized solution scheme, and a full complement of known properties, inputs, initial conditions, and boundary conditions, the solution methodology advances to the implementation of the numerical solution.

## **5.3 Implementation of Numerical Solution**

Numerical solution of the evolved system of equations follows a familiar script.

- (1) All properties, inputs, and boundary conditions are evaluated at the prescribed initial condition.
- (2) An incremental time step implemented, advancing the solution to the next discretized time. The system is then evaluated at the new time-step within an iteration scheme to obtain a converged solution to the time-implicit equations.
- (3) This procedure is then repeated for a given number of time-steps to “march” the solution through time.

### 5.3.1 Evaluation of Inputs

At the beginning of each successive time-step within the numerical solution, updated values for all temperature- or time-dependent quantities must be obtained. Two basic options exist for the evaluation of these properties, source terms, and boundary conditions. (1) Inputs may be calculated at each time-step using the temperatures from the previous time-step, or (2) inputs may be assessed using an iterative or predictive scheme at the current time-step. The latter option of an iterative or predictive evaluation of inputs generally offers the most accurate method of computing this information. However, as will soon become evident, iterative methods are computationally demanding. The former possibility, computing the inputs using temperatures from the previous time-step, affords the advantages of simplicity and computational efficiency. By assessing the inputs in an explicit fashion, their values “lag” the solution by one time-step. For relatively small time-steps, this incurs minimal computational error and few problems. Therefore, an evaluation format of allowing input computations to lag the solution is adopted. It is worth noting, however, that the phrase “relatively small time-steps” is key to this method. Significant stability problems arise from the violation of this caveat. Thus, a method of quantifying the “smallness” of time-steps is later presented.

#### *Material Properties*

Sections 3.2.3 and 3.2.4 relate the development of temperature-dependent functions for applicable material properties. Advancing the numerical solution, these property functions are evaluated in a lagging fashion at the start of each time-step. Despite the explicit nature of this procedure, it produces little cause for stability concerns, as property values change gradually over the thermal range of this investigation.

### ***Boundary Conditions***

Section 4.1.3 explains the physics and data regarding the convection boundary condition. Section 4.2.3 demonstrates the application of a linearization method to the external radiation boundary condition, allowing implementation as though it were convection. This information is then discretized within the derivations of section 5.2.3. The discretization coefficients conveying the convection contribution, are constant by virtue of the definition of the convection coefficient utilized.

As to the discretization coefficients containing the external radiation contribution, by definition of the linearized radiation coefficient  $h_r$ , these terms are inherently dependent upon temperature. Thus, again much as the material properties, these terms are evaluated in a lagging scheme to preclude iterative, nonlinear solutions. However, unlike the material properties, utilizing this simplistic method creates a potential for stability problems. A moderate change in temperature from the previous to the current time-step can generate a significant change in the radiation coefficient, and thus, in the radiative losses computed. If this change yields a temperature solution sufficiently far removed from the correct solution, an oscillation may be created. The potential instability concern is further explored within the coming *Stability Criteria* subsection.

### ***Source Term***

Concerning the majority of interior nodes, the source term contains no temperature-dependent terms. In most cases, the source term represents a varied combination of heat source input, lumped convection, and / or lumped heat source input. Those instances involving heat source input entail evaluation of the time-dependent input schedules.

Regarding those surfaces illustrated in Figures 4.3, 4.4, and 4.5, the source term contains quantities representing the internal radiation interaction among complementary nodes. In the same manner as the temperature-dependent properties and radiative discretization coefficients, nodal values for the source term are computed using

temperature values from the previous time-step. Source terms entailing internal radiation terms exhibit an exacerbated case of the stability problem alluded to in the foregoing *Boundary Conditions* subsection.

Considering the internal radiation model of sections 4.2.2 and 5.1.2, the same construction that affords the aforementioned, and convenient energy conservation aspect, also affects a significant instability potential. Specifically, the selected method of simulating internal radiation requires that the radiant energy leaving an emissive node be entirely absorbed by its complementary receptor node. In this fashion, any error in computed temperatures produced by overly large time-steps is not only evidenced in one of the complementary nodes; it is mirrored by the other. Therefore, if computed temperatures from the previous time-step generate a surplus heat loss from an emissive node, its complementary absorptive node receives an equitable surplus heat gain. In this sense, the instability propensity of internal radiation terms is twice that of external radiation terms. For this reason, this quantity is the basis for the forthcoming development of a stability criteria.

### ***Stability Criteria***

To prevent any numerical oscillations induced by explicit techniques, a stability criteria is implemented. Drawing on the propensity for instability outlined in the *Source Term* subsection above, this criteria is based upon an energy balance on an arbitrary node experiencing internal radiation, as in Figure 5.7.

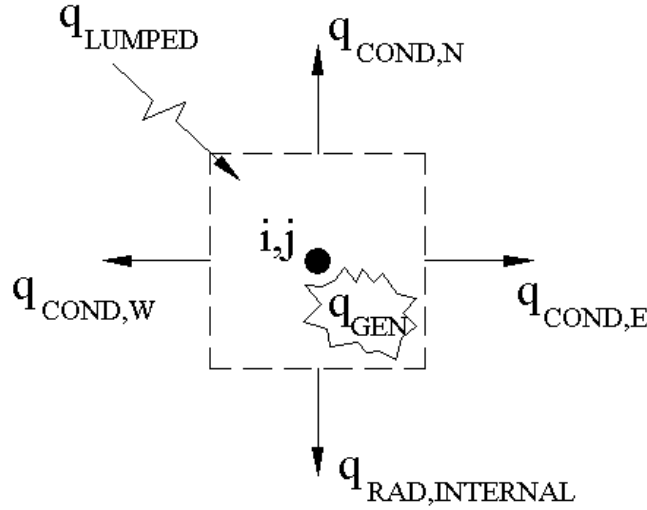


Figure 5.7 Schematic of Internal Radiation Node—Stability Development

Copious algebraic manipulation is then performed to isolate terms containing the explicit temperature,  $T_{i,j,p-1}$ . More algebra results in a grouping of terms multiplying  $T_{i,j,p-1}$ . The coefficient acting on  $T_{i,j,p-1}$  must be positive to ensure stability. Appendix G provides a rigorous derivation of this relationship; considering the length of the equations and the derivation, only the resulting relation is given here. Thus, although the bulk of the solution methodology presented is based on implicit time discretization, to maintain a stable solution in light of the foregoing explicit approximations, the selected time-step should meet the following criteria:

$$\Delta t < \frac{C_1}{\left( \frac{1}{R_{in} + R_{out}} \right) + \sigma A T_{i,j,p-1}^3 + K_E + K_W + K_N}, \quad [5.17]$$

where  $\Delta t$  is the stable time-step,  $C_1 = \rho_{i,j} V_{i,j} C p_{i,j}$ , and  $K_E = \frac{k_E \Delta y_{i,j}}{\Delta x_E}$ ;  $K_W$  and  $K_N$  are similarly formulated.

It is both pertinent and interesting to note that, due to the nonlinear form of the internal radiation term, the above expression for stability is a function of the temperature from the previous time step. This implies that, in certain cases, dynamic computation of the stability criteria may be necessary to obtain a valid solution. An alternative approach is to decrease the time-step at strategic points during the simulation to avoid instabilities. This method is employed herein. As the maximum evaporation temperature is attained, the time-step is decreased by a predetermined factor to a stable size. In this fashion, the efficiency of the solution may be improved without sacrificing stability.

Furthermore, the foregoing relation for stable time-step selection is also strongly influenced by grid dimension. This effect enters, in dominating fashion, through the equivalent resistance term. Thus, consideration should be given to stability during any grid refinement procedures.

### **5.3.2 Iterative Solution**

At this point in the investigation, a system of equations, complete with boundary and initial conditions, has been assembled; a method of evaluating relevant inputs to these equations has been decided; and an expression for the computation of a stable time-step size has been derived. Next, a scheme for the solution of this system of simultaneous linear (or linearized) equations is requisite. As previously noted, numerous direct and indirect solution methods exist for this purpose. By assembling the equations in matrix form, a particular method soon becomes evident.

Matrix inversion is highly unfeasible due to the magnitude of computations required in the solution of such large sparse matrices. A tridiagonal solver, most applicable to one-dimensional problems, is of no direct use in two-dimensional problems, as they lack tridiagonal structure. However, an obvious possibility is a Gauss-Seidel iteration method.

The equations are arranged in the form:

$$T_{i,j} = (aW_{i,j} T_{i-1,j}^* + aE_{i,j} T_{i+1,j}^* + aS_{i,j} T_{i,j-1}^* + aN_{i,j} T_{i,j+1}^* + b_{i,j}) / a_{i,j} , \quad [5.18]$$

where  $T^*$  denotes the value of  $T$  at the previous iteration. Successive guesses for the temperatures are iteratively evaluated to reach a converged solution. Unfortunately, this technique is slow to converge because the boundary inputs are conveyed by one grid-step each iteration (Vick, 2000).

An improved means of solution combines the tridiagonal algorithm with the Gauss-Seidel iteration scheme. Commonly termed “Line-by Line Method” (Vick, 2000), this method solves a single, one-dimensional, line of nodes at a time. By assuming the surrounding values from the previous time step, the Line-by Line technique, uses the tridiagonal algorithm to solve this line, repeatedly sweeping across the domain. Following each sweep, Gauss-Seidel iteration is employed to evaluate convergence and establish the next set of guessed temperatures. Again, this process is repeated until satisfactory convergence is achieved.

A common improvement applied herein to the Line-by Line method is the execution of multiple sweeps in alternating directions. In other words, during each Gauss-Seidel iteration, the solution domain is swept alternately in both the  $x$ – and  $y$ – directions, multiple times. This process affords faster overall convergence and a more accurate solution within each iteration, as diffusion effects are transmitted in all directions using the “current” temperatures.

### 5.3.3 Marching Through Time

With an assembled system of equations and various inputs, coupled with an efficient iterative solver, the final task in obtaining a full solution to the transient problem

lies in marching the solution through time. Compared to the foregoing developments, this procedure is both uncomplicated and brief.

Concisely, after establishing the initial conditions, an incremental time-step is taken in the solution scheme. Wherein, the previous temperature values are stored as the current guesses, the time counter is augmented by the time-step values, the inputs are re-evaluated using the current guesses, and the iterative solution process begins. Following satisfactory convergence of the solution at the current time-step, the subsequent time-step is made. The inner loop of iterative solution proceeds within the outer loop of time marching until the prescribed number of time-steps has been evaluated. Figure 5.8, on the following page, illustrates this nested loop structure.

Thus, the transient solution of a discrete two-dimensional domain, with time- and temperature-dependent inputs, representing the operation of a conventional box evaporation source, is obtained. The foregoing solution methodology is then fully implemented using Mathematica<sup>®</sup>, Version 3.0 to acquire useful results. A full copy of the developed Mathematica<sup>®</sup> program is included as Appendix H.

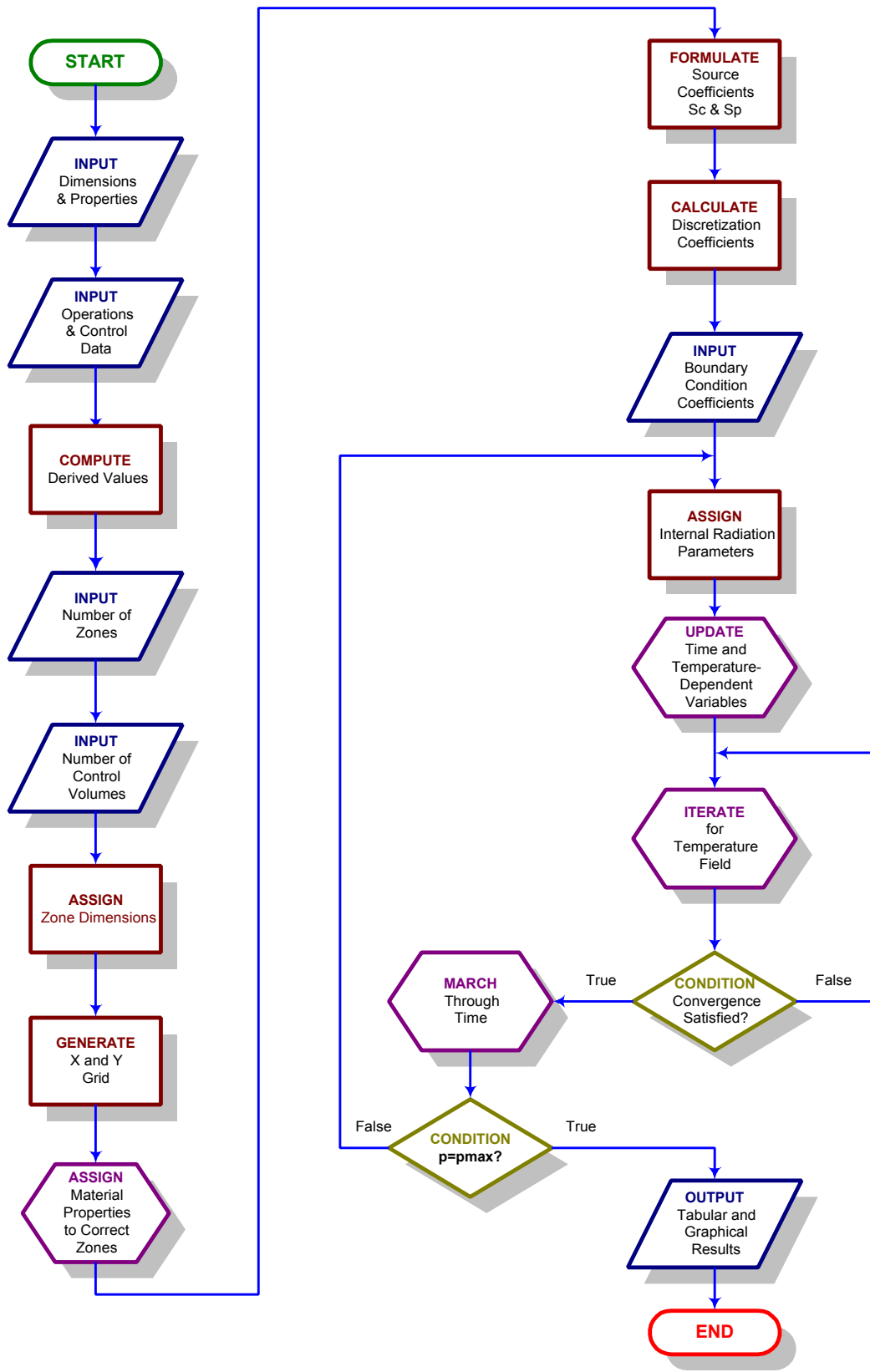


Figure 5.8 Simplified Flow Chart of Numerical Solution

# Chapter 6.0

## Simulation Results

Recall, once again, that the second and third objectives set forth within this thesis are 2) the validation of the numerical model developed within and 3) the simulation and evaluation of potential enhancements to the physical system. Utilizing the Mathematica<sup>®</sup> code of the model included as Appendix H, numerous simulations were run, modeling the various conditions established by known case parameters or experimental operations data.

### 6.1 Validation of Solution

The second objective outlined above requires a thorough process of model and solution validation. To meet this criteria, a multiphase validation methodology comprising: 1) grid refinement, 2) convergence criteria refinement, 3) stability assessment, 4) comparison to known cases studies, and 5) comparison to experimental data, is employed. This composite verification procedure provides validation of both the numerical solution and the mathematical model.

#### 6.1.1 Grid Refinement

The process of grid refinement offers a method of ascertaining what grid density offers a grid-independent solution. In other words, a limiting maximum grid density is determined, beyond which, additional solution accuracy is negligible.

Within this investigation a doubling scheme is utilized, wherein the number of grid points in each direction is successively doubled. In a two-dimensional problem such as this, the grid density is increased by a factor of four.

Beginning with a coarse grid density of 126 nodes, this trend results in the following progression of refinements:

Table 6.1 Grid Refinement Schedule, Simulated Time = 1680s

<b>Grid Density</b>	<b>Number of Nodes</b>	<b>CPU Time Required for Solution (seconds)</b>
Coarse	126	65
4X	504	700
16X	2016	4367
64X	8064	33425

Following the schedule illustrated by Table 6.1, simulations are conducted employing the prescribed grid densities.

Figure 6.1 on the following page depicts the results of this refinement procedure for the transient numerical solution at the center thermocouple position. Recall that this position lies on the centerline or line of symmetry of the physical vaporization source. The graph presents both the numerical inputs and the outputs of the simulation, detailing the constant power supplied to the upper and lower heat sources and their respective transient responses. A simulated time span of 1680 seconds is employed to maintain reasonable computation times. The asymptotic convergence of successive refinement steps demonstrates the desired trend for solution validation. In that, as grid density is increased, the solutions approach limiting values, beyond which further refinement is fruitless. Also of note are the time-step-induced instabilities evidenced in both the 16X and 64X grid densities beginning at approximately 1200 seconds. This occurrence demonstrates the substantial effect grid resolution has on the stability criteria. Specifically, from equation 5.17 one may deduce that as control volume dimensions,  $\Delta x$  and  $\Delta y$  are decreased; so too must the time-step be reduced.

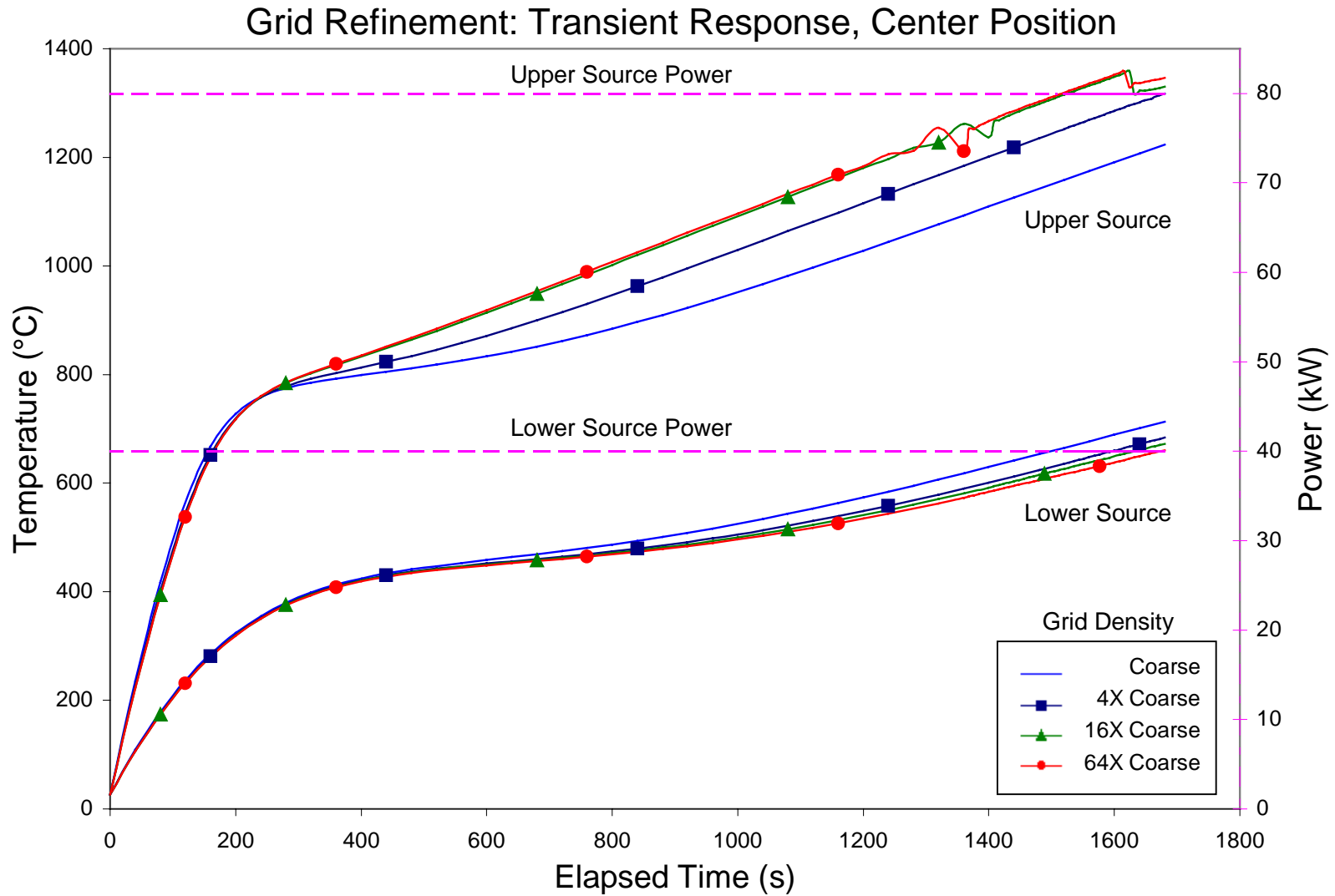


Figure 6.1 Grid Refinement, Transient Response

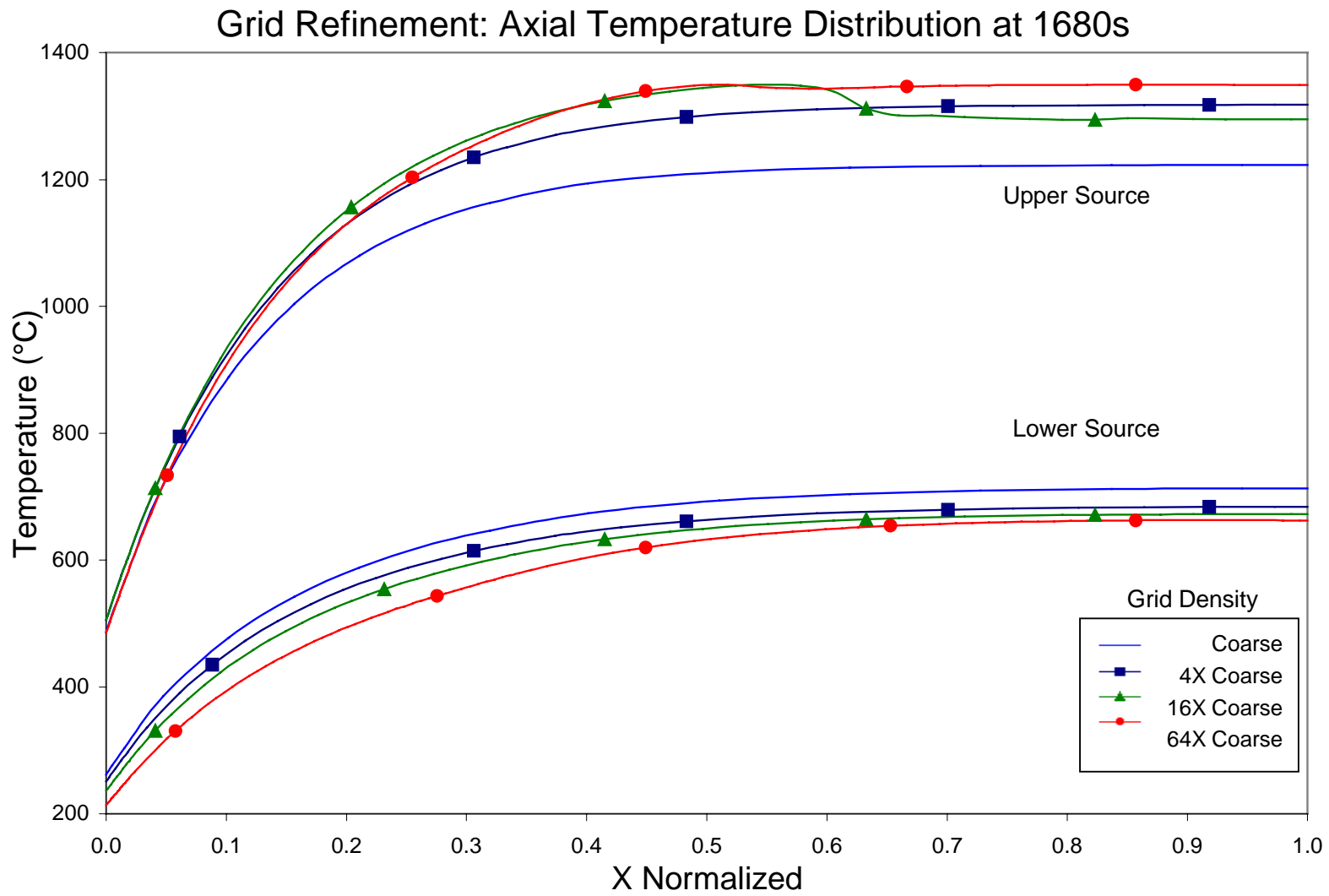


Figure 6.2 Grid Refinement, Axial Temperature Distribution

Figure 6.2 succeeds Figure 6.1, depicting the results of refinement for the axial temperature distribution at 1680 seconds. Again, the output data for both the upper heat source and the lower heat source are plotted. As in Figure 6.1, the axial distribution plots are asymptotic to a theoretically ideal solution near that portrayed by the 64X Density curve. The idiosyncrasies present within the upper source curves depicting 16X and 64X grid densities are the result of the dynamic time-step reduction of previous allusion.

Examining Figure 6.1 and Figure 6.2 in a qualitative manner, one expects that an ideally sized grid possesses approximately the 64X density. However, referring to Table 6.1 above, the computational accuracy of such a fine nodal network must be weighed against the solution time required. Obviously, a simulation representing 1680 seconds of operation that requires 33425 seconds (9 hours and 17 minutes) to run will no doubt be intolerable in replicating 8000 seconds of physical system operation. Therefore, a less computationally demanding grid density should be utilized in further simulations.

To that end, the notion of deviation is introduced. For the purposes of this thesis, deviation is considered to be the absolute value of the difference between two compared temperature values:

$$d = |T_1 - T_2|, \quad [6.1]$$

where  $d$  signifies the computed deviation. Comparing this notion to variance or standard deviation, it is evident that the sample size of two would produce virtually meaningless results if either alternative were chosen. Hence, the concept of deviation is utilized to select an appropriate grid density for subsequent simulations. Table 6.2 presents deviation values for the transient response of Figure 6.1.

Table 6.2 Deviations Among Subsequent Grid Densities

	<b>Upper Source Transient Response, Center Position</b>	<b>Lower Source Transient Response, Center Position</b>
<b>Refinement Step</b>	<b>Mean Deviation, <math>\bar{d}</math></b>	<b>Mean Deviation, <math>\bar{d}</math></b>
Coarse → 4X Density	57.1	15.4
4X Density → 16X Density	33.4	4.71
16X Density → 64X Density	15.6	4.20
Coarse → 64X Density	103.2	24.3
4X Density → 64X Density	46.2	8.90

Deviations for the axial distribution of Figure 6.2 are not tabulated. In light of the nature of grid refinement, the domain of  $x$  locations is not identical for each grid density. Thus, an accurate representation of the deviation is not defined. More specifically, a correct comparison of temperature values must occur at the same axial location. Since the data does not reflect this condition, this comparison is omitted.

Thus, noting Table 6.2, the obvious grid density choice for optimal accuracy is 64X. However, reconciling this fact with the ominous CPU time of Table 6.1, a revised selection of 4X is made. This nodal scheme yields a maximum expected mean deviation of less than 4% of the experimental steady-state temperatures to be later simulated. For the purposes of this investigation, this level of accuracy is deemed sufficient.

## 6.1.2 Convergence Criteria Refinement

In much the same manner as the grid refinement detailed above, the convergence criteria used to signify a sufficiently accurate solution at the close of each Line-by-Line iteration must be optimized. In that, the accuracy of the overall solution is dictated by the correctness of the solution at each time-step. Therefore, it is imperative that the solutions obtained be independent of convergence criteria.

A refinement method similar to that implemented above is adopted to test the solution dependence of convergence criteria. Successive simulations employing increasingly stringent convergence criteria are conducted utilizing identical grid size, time-step, and input data. A criteria refinement schedule decreasing by two-orders of magnitude is utilized, comprising criteria of  $10^{-2}$ ,  $10^{-4}$ ,  $10^{-6}$ , and  $10^{-8}$ , simulating 3000 seconds of operation. Figures 6.3 and 6.4 portray the effects of convergence criteria refinement with regard to transient temperature response and axial temperature distribution of the solution domain.

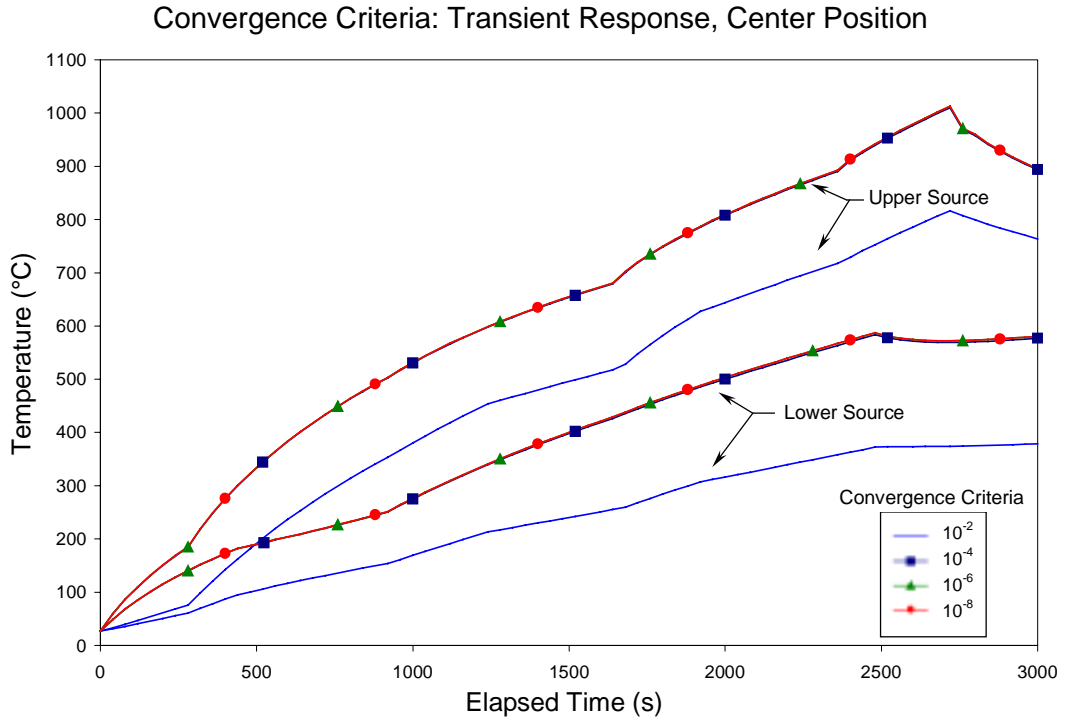


Figure 6.3 Convergence Criteria, Transient Response

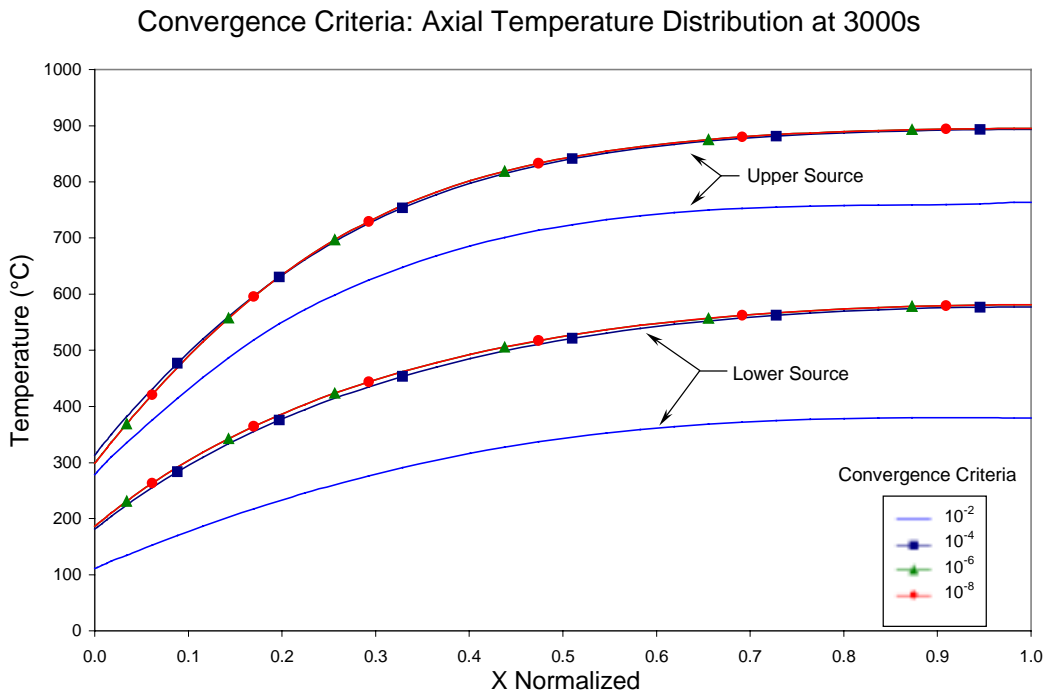


Figure 6.4 Convergence Criteria, Axial Temperature Distribution

In both scenarios, the most liberal criteria  $10^{-2}$  produces responses significantly removed from the accurate solutions illustrated by the convergence of  $10^{-4}$ ,  $10^{-6}$ , and  $10^{-8}$ . It is interesting to note the substantial change in accuracy imparted by two steps in criteria order. Obviously, a convergence criteria of  $10^{-4}$  is more than sufficient for the objectives sought within this project.

### 6.1.3 Time Dependence of Model Stability

Considering the pivotal role that the time-step plays in the development of a numerical solution to transient problems of this nature, a study of the stability criteria detailed in section 5.3.1 is most germane. Figure 6.5 presents the results of several simulations employing various degrees of stable time-steps.

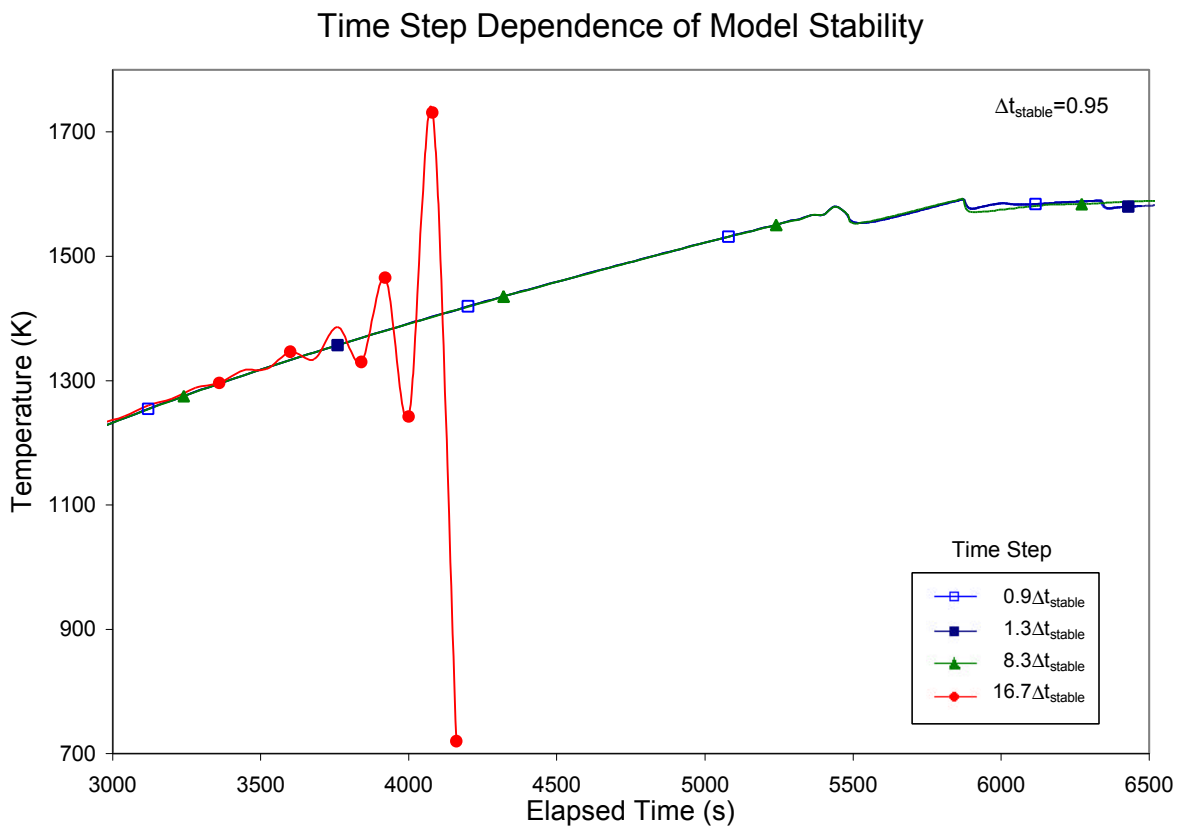


Figure 6.5 Time-Step Dependence of Stability

Using equation 5.17 defining the stability criteria, four simulations corresponding to  $0.9\Delta t_{stable}$ ,  $1.3\Delta t_{stable}$ ,  $8.3\Delta t_{stable}$ , and  $16.7\Delta t_{stable}$  are modeled using a value of  $\Delta t_{stable} = 0.95s$ . Note that these designations indicate the time-step utilized in the latter portion,  $T > 1573K$ , of the simulations. It is in this regime that stability issues are most prevalent.

Beginning with the least stable time-step selection, that of  $16.7\Delta t_{stable}$ , it is obvious that this choice leads to a numerically induced oscillation, not attributable to the model physics. Interestingly, little instability is incurred in the use of the  $8.3\Delta t_{stable}$  or the  $1.3\Delta t_{stable}$  time-steps save for minor wavering just prior to the time-step transition. Wherein, the time-step size is sufficiently close to stability that no discernable problems exist for the times and temperatures examined. Finally, almost as expected, the  $0.9\Delta t_{stable}$  solution exhibits little propensity for instability. However, the miniscule oscillation evidenced in each of the “stable” simulations prior to time-step reduction reveals that the efficiency enhancement of time-step reduction must be carefully applied. In that, the effect of the temperature term in the denominator of the stability equation requires that, to maintain stability, the time-step reduction must occur somewhat earlier in the simulation. This adjustment is instated prior to proceeding with the following set of case studies.

## 6.1.4 Case Studies

Following the stability investigation, the next phase of model validation is the numerical simulation of simple case studies. In this process, the numerical model is configured to emulate the behavior of a system having well known, basic inputs. Table 6.3 summarizes the case studies utilized in the numerical solution validation within this thesis.

Table 6.3 Case Studies for Model Validation

Case Study Number	Brief Descriptor	Input Summary
0.0.0	Null Case	Zero heat input, null boundary conditions
1.0.1	Convective Cooling	Zero heat input, convective cooling via boundaries and lumping only
1.1.1	Radiative Cooling	Zero heat input, radiative cooling at upper boundary only
2.2.0	Full Heat Input	All heat sources “on”, zero cooling
3.0.1	Evaporation Trial	Point heat source at midpoint of nodal network, zero cooling

Case study 0.0.0 is, by far, the most simplistic verification test implemented within this project. Quite simply, the numerical model is prepared with zero heat input and zero losses. Hence, an expected solution yielding the initial condition is anticipated.

Case 1.0.1 examines the effect of convective cooling, at the boundaries and through the lumping term, on the validity of the numerical solution. To achieve this scenario, all heat inputs remain zero, while the convection coefficient is reinstated to its prescribed

value of  $h_{eff} = 1900 \frac{W}{m^2 K}$ .

The radiative cooling trial, case 1.1.1, alludes to the imposition of radiative cooling as the sole heat loss mechanism. Again, the heat-input terms are left as zero; only the response elicited via radiation is desired.

Case 2.2.0 represents the first test of the heat input terms. In this vein of the investigation, all heat loss quantities are set to zero, while the effects of heating via the upper and lower heat sources is verified. By virtue of the system operation, this examination also explores the proper function of the internal radiation mechanism, as the vaporization vessel lower surface and the evaporant upper surface are heated almost entirely via this mode.

Finally, case 3.0.1 portrays a trial of the evaporation mechanism. The purpose of this isolated investigation is the validation of proper heating of the evaporant's exposed surface and the correct depletion of evaporant nodes. This test is accomplished by instating a point heat source near the grid midpoint of the upper heat source. Allowing both the internal radiation and the evaporation mechanisms to operate, without any other heat loss or gain, the system behavior is examined.

Figure 6.6, Panels a) and b), illustrate the system's transient response to the five prescribed case studies at the center position. Panel a) depicts the results of studies 0.0.0, the null case, and 3.0.1, the evaporation trial. Panel b) shows the response to cases 1.0.1, 1.1.1, and 2.2.0, the convection, radiation, and full heating cases, respectively.

The results within Panel a) are as anticipated. The null case transient response, for both the upper and lower heat sources, is steady at the initial temperature,  $T_i = 27^\circ C$ . The evaporant trial response for the upper heat source illustrates the gradual heating trend incurred by a distant heat input. Recall, that the point source providing heat to this simulation lies at the grid midpoint, which is one-half of the system away from the "center" position. The lower heat source, far removed from the point source within the upper heat source, shows no response to the heat input, as is expected.

### Case Studies: Transient Response, Center Position

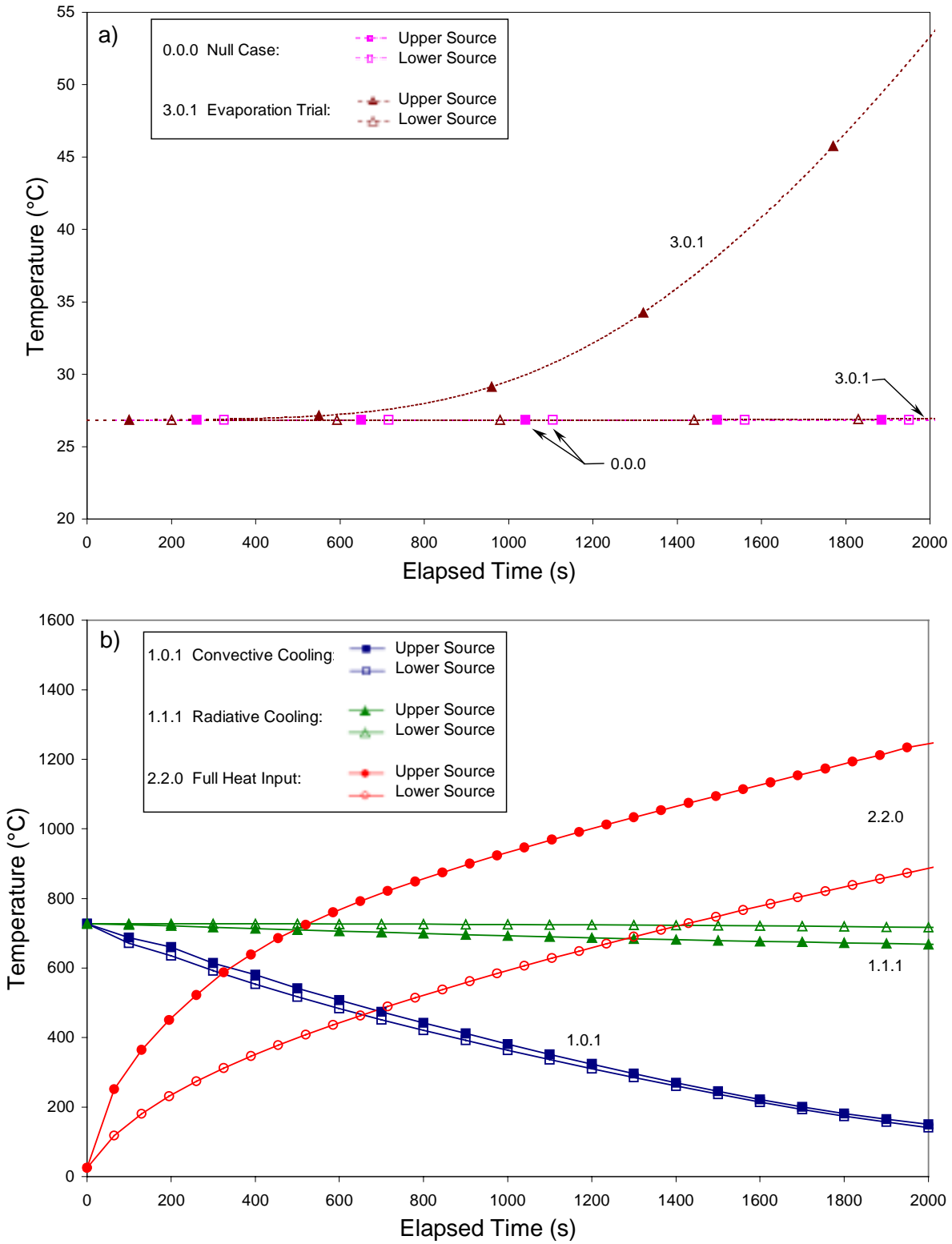


Figure 6.6 Case Studies: Transient Response, Center Position

Similarly, Panel b) evidences favorable responses for each of the test cases shown. Case 1.0.1 portrays the relatively fast temperature-decay of the upper heat source and lower heat source nodes coupled remotely to a convectively cooled boundary. Meanwhile, case 1.1.1 depicts the more gradual decline of the same nodal temperatures connected to a radiative boundary condition. Finally, the full heat input simulation is an obvious example of directly heated nodes having no cooling effects. Receiving a significantly increased power input, the upper heat source outpaces the lower heat source.

Figure 6.7, Panels a) and b), illustrate the elicited axial temperature distributions for the foregoing case studies at 2000 seconds. Note that case studies are grouped by graph scaling within Panels a) and b) for both Figure 6.6 and Figure 6.7.

Panel a) presents the output of the null case and the convectively cooled simulation. Wherein, having zero heat gains and losses, the null case displays no thermal gradients. Contrastingly, the convectively cooled scenario manifests thermal gradients relating a convectively cooled left boundary. Furthermore, the additional cooling sensed by the lower source facilitates the offset seen between the two distributions.

Panel b) of Figure 6.7 depicts the remaining case studies: radiative cooling, 1.1.1; full heat input, 2.2.0; and evaporation simulation, 3.0.1.

The axial temperature distribution generated for the radiative illustrates the proper behavior. As the upper heat source is closer proximity to the radiative boundary, more cooling is simulated. Furthermore, since the radiation boundary condition spans nearly the entire upper surface of the system, no discernable gradient is portrayed.

With respect to the full heating scenario, as the leftmost portion of the system is dominated by conduction, while the remainder is governed almost entirely by internal radiation, a slope toward the left boundary. Once again, the upper head source receives higher power input; this is again evidenced in the output of Panel b).

Case Studies: Axial Temperature Distribution at 2000s

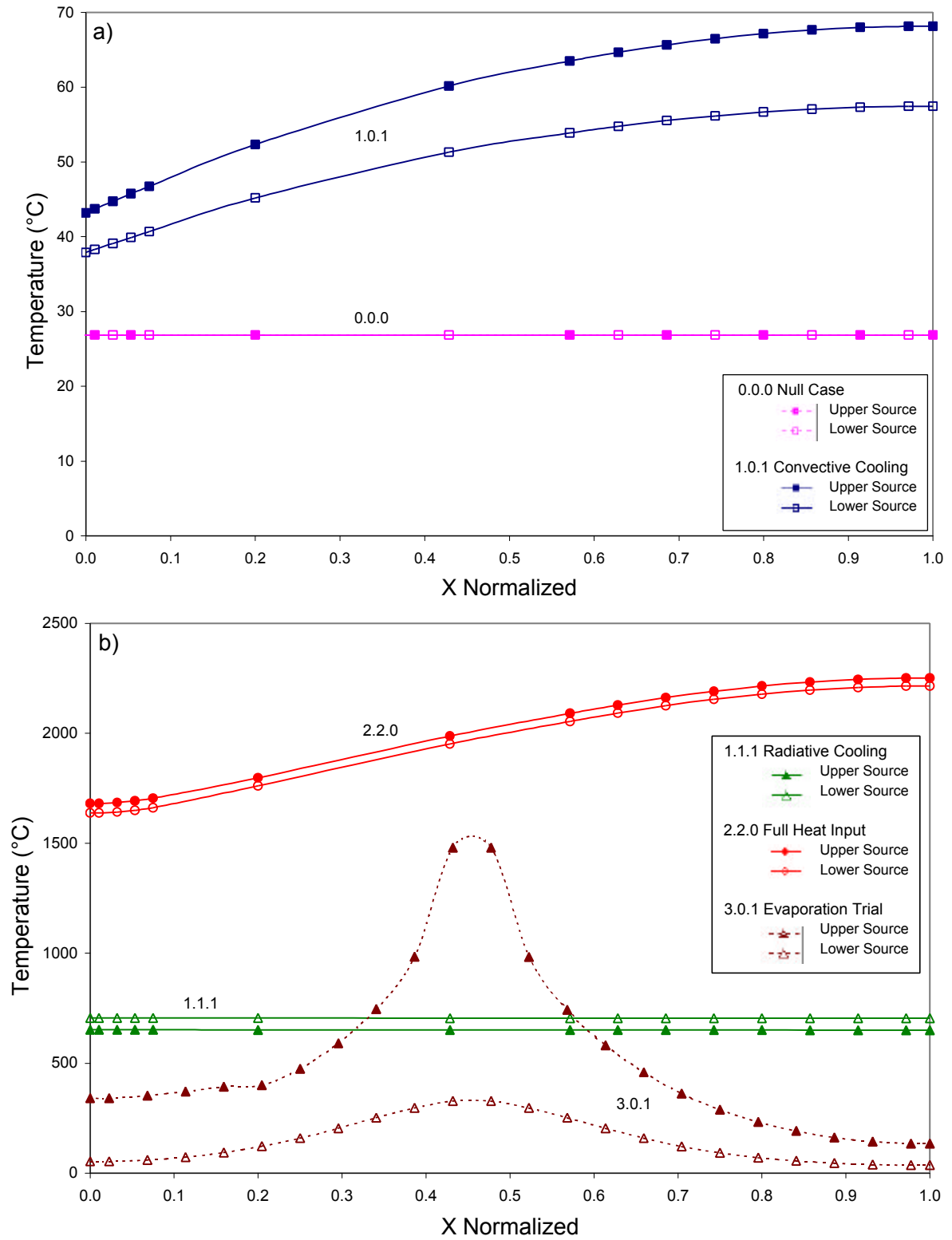


Figure 6.7 Case Studies: Axial Temperature Distribution, 2000 seconds

Finally, the most obviously correct trend within Figure 6.7, Panel b) takes the form of the axial distribution attributed to the evaporation trial. Specifically, containing the point heat source, the axial distribution of the upper heat source illustrates the conspicuous peak expected. A more mute distribution is seen in the lower heat source axial temperature distribution, attributable to the diffusion effects between the two locations.

Figure 6.8 maps the spatial temperature distribution of case 3.0.1. Wherein, the imposed point heat source is evident near the midpoint of the grid structure and is fully enclosed by contours of decreasing temperature.

### Spatial Temperature Distribution Case 3.0.1: Evaporation Trial

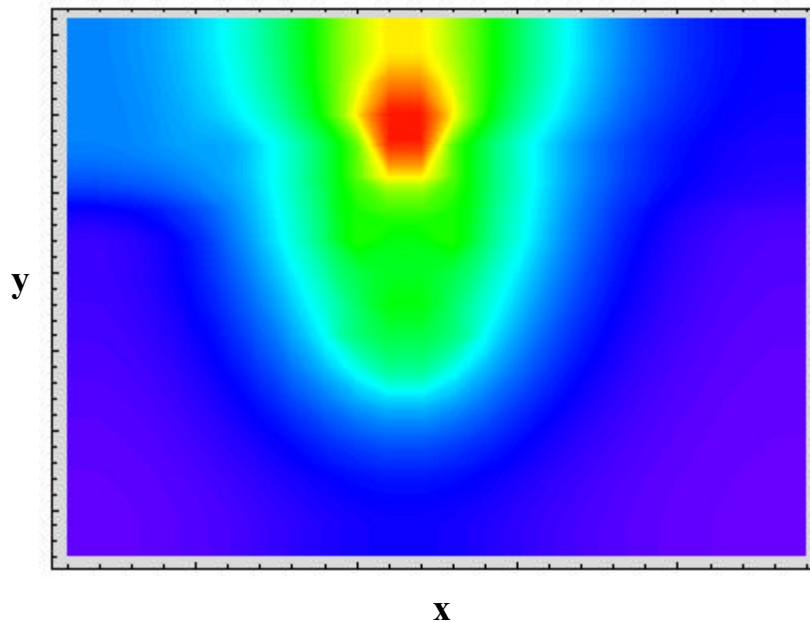


Figure 6.8 Spatial Temperature Distribution, Case Study 3.0.1

Figure 6.9 depicts the correct, anticipated systematic depletion of evaporant incurred by this trial. It is imperative to acknowledge that this plot does not portray any gradient information; the resolution contained is almost digital. In that, a node is either evaporant, evaporant-depleted, or neither. Thus, Figure 6.9 illustrates the absence of evaporant directly beneath the point heat source, the presence of nearby evaporant nodes, and the existence of heat source or void nodes in the upper bounding region.

## Spatial Evaporant Distribution Case 3.0.1: Evaporation Trial

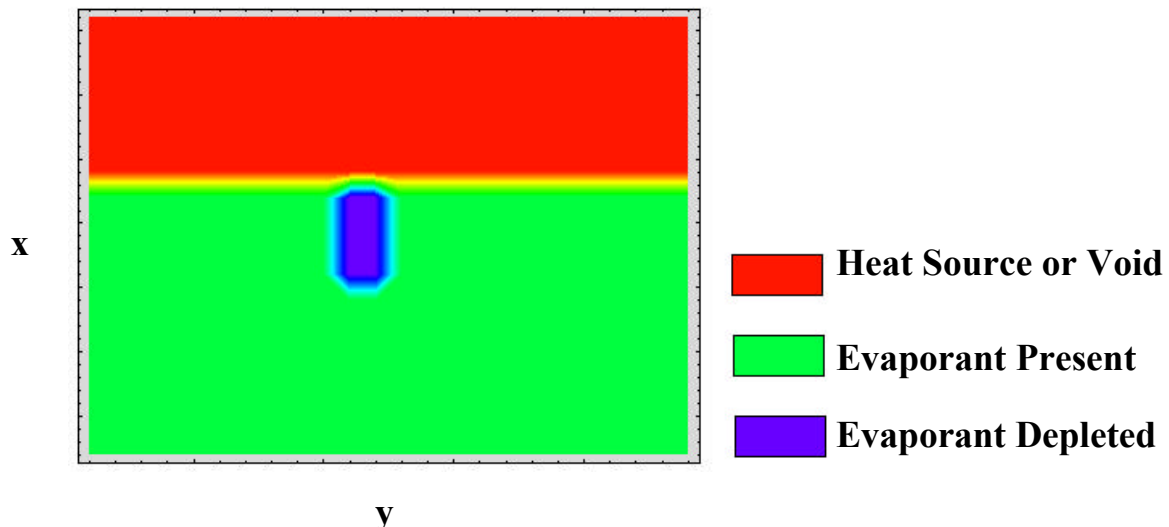


Figure 6.9 Contour Plot of Evaporant Depletion, Case Study 3.0.1

Thus, in all cases simulated, the developed numerical solution provides the correct behavior given the prescribed inputs.

### 6.1.5 Experimental Validation

Having established the basic validity of the numerical solution via the aforementioned studies, only experimental verification remains. Concisely, if the derived mathematical model and subsequent numerical solution are to predict hypothetical system behavior, sufficient proof must be provided assuring their accurate simulation of known system operation. To that end, two experimental operations data sets, as in section 3.2.7, are presented. These data describing the transient operation of the physical system are compared to their numerical predictions as generated using the foregoing solution methodology.

### ***Data Set I***

Figure 6.10, Panels a) and b) chart the transient response and respective power inputs of Data Set I, for the experimental and numerical systems, for the lower and upper heat sources at the center position.

Panel a) illustrates the numerical solution's simulation of the lower source transient response to the power input schedule of Data Set I. As compared to the experimental curve, the numerical prediction displays poor accuracy. Quantitatively, a mean deviation between the experimental and numerical response of  $269^{\circ}\text{C}$  is computed. A portion of this discrepancy may be attributed to the obvious lack of experimental oscillations in the numerical input. Hence, the numerical response fails to predict subsequent damped thermal response to these changes evident in the experimental plot. However, the suspect explanation for this discrepancy lies in the absence of conduction in the  $y$ –direction from the upper heat source to the vaporization vessel at the  $z$  boundary within the numerical model. Although the lumping term accounts for lateral conduction, this coupling of the upper heat source and lower model regions goes unaccounted.

Panel b) demonstrates the numerical simulation of the upper heat source transient response resulting from the numerical approximation of the shown experimental heating schedule. Qualitatively, this response fairs better, in comparison to the experimental behavior, than that of Panel a). In that, the numerical solution tracks the experimental response with surprising accuracy, considering the boundless opportunities for error introduction. Quantifying this behavior, a mean deviation from experimental performance of  $132^{\circ}\text{C}$  is obtained. Note, again, the absence of experimental oscillation within the numerical power input function. Furthermore, the saw-tooth peaks present in the upper heat source transient response bear consideration.

### Transient Response: Data Set I, Center Position

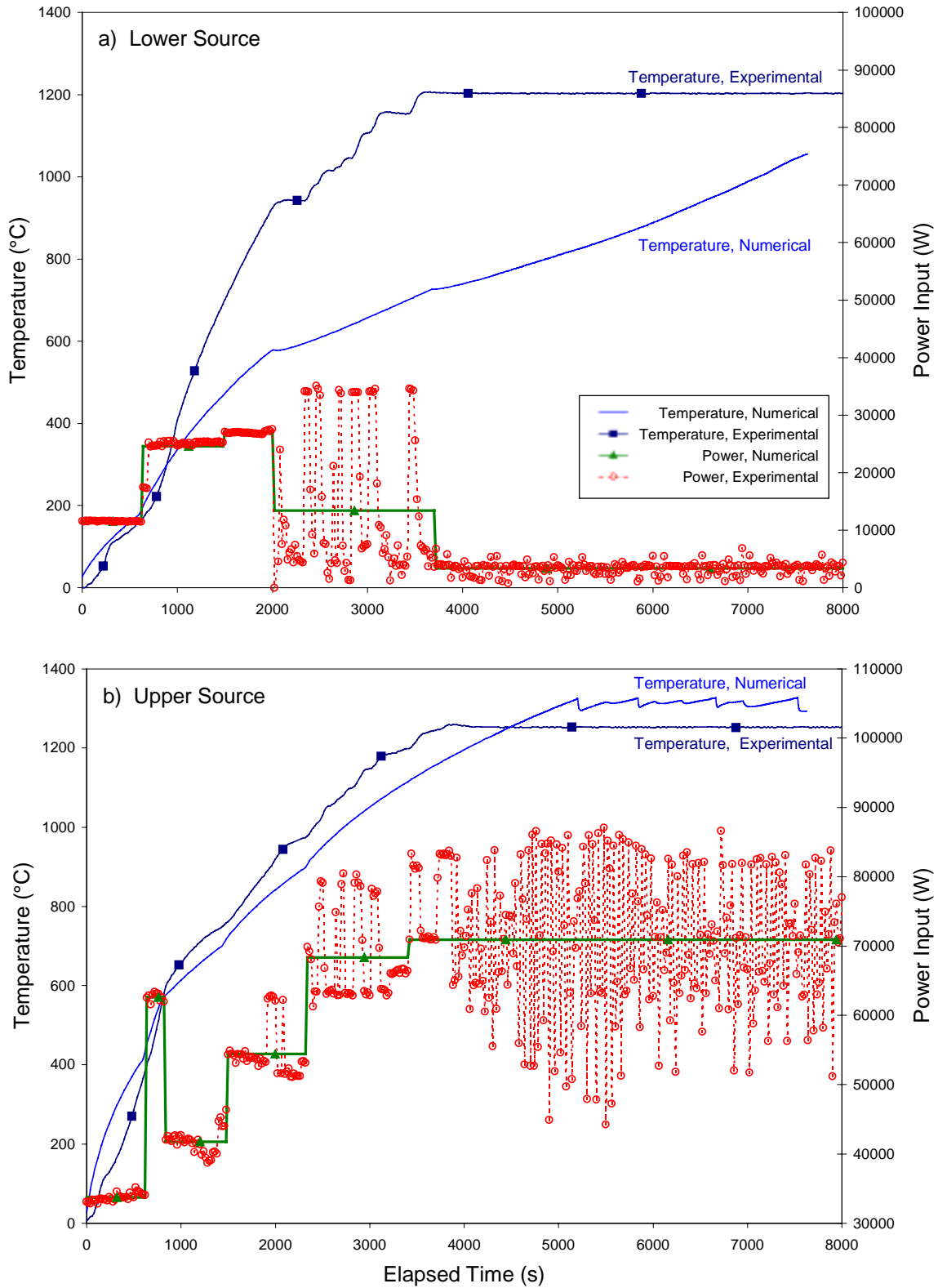


Figure 6.10 Numerical Simulation of Data Set I Transient Response, Center

Figures 6.11 and 6.12 render the axial temperature distribution and spatial temperature distribution resulting from the numerical simulation of Data Set I, as computed at 8000 seconds of operation. Lacking sufficient comparative experimental data, these figures are presented for qualitative examination and for standards of comparison for forthcoming proposed improvements.

The axial temperature distribution of Figure 6.11 exhibits performance to be expected in light of the given inputs. Specifically, both the upper and lower heat sources experience cooling due to a convective boundary condition at their left edge as predicted. The upper heat source receives indirect cooling via the upper surface radiative boundary condition. The vaporization vessel, insulated at the left boundary, shows an elevated temperature heated via conduction from the surrounding sources.

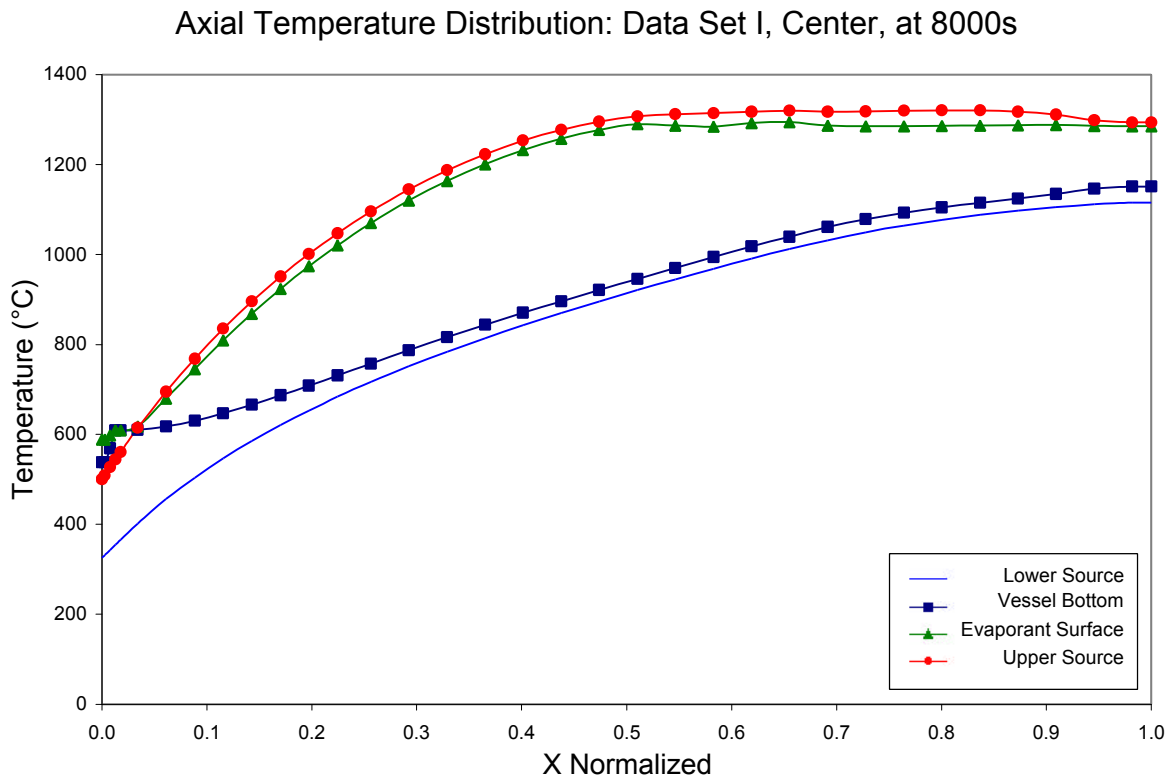


Figure 6.11 Axial Temperature Distribution, Data Set I, 8000 seconds

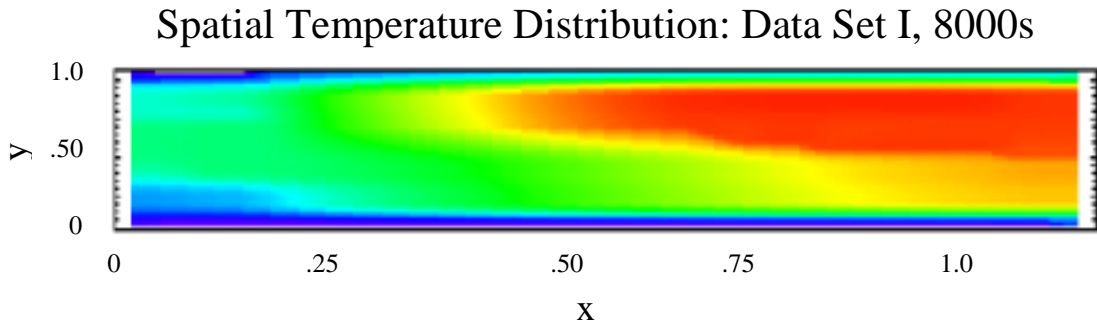


Figure 6.12 Spatial Temperature Distribution, Data Set I, 8000 seconds

Figure 6.12 provides easy visualization of the system performance outlined above. A useful revisit of Figure 4.1 depicting relevant model physics is warranted. Hence, cooling and heating trends anticipated from the model physics are faithfully replicated in the spatial temperature distribution.

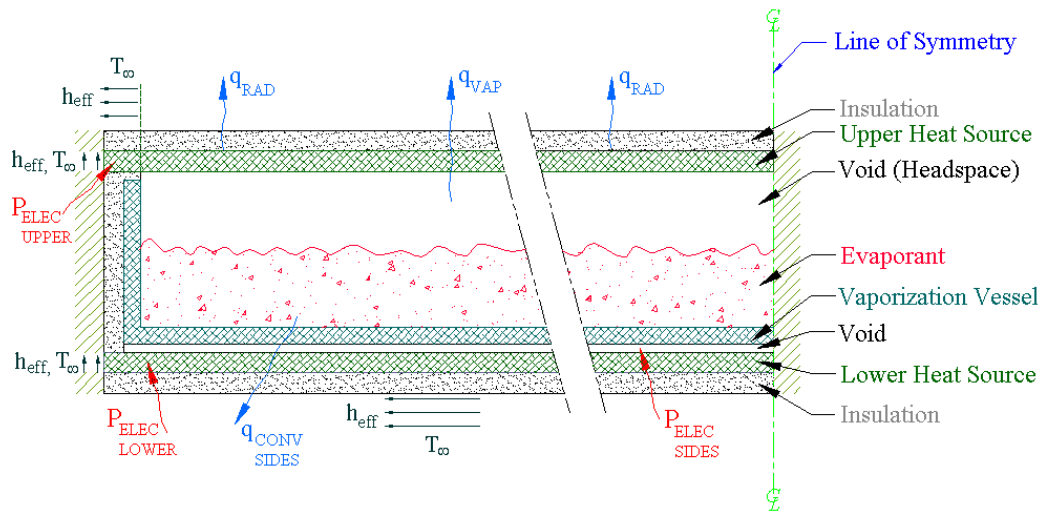


Figure 4.1 General Schematic Representation of Model Physics (revisited)

## ***Data Set II***

Figure 6.13, Panels a) and b), present the results of the numerical simulation of the transient response of the upper and lower heat sources of Data Set II at the center position.

Panel a) illustrates the numerical response of the model system to the numerical approximation of experimental heat input. The general trend regarding the accuracy of this solution is quite similar in its inadequacy to that of Data Set I. Although the sudden drop in experimental and numerical power input is sensed by the numerical solution, its response is subtle compared to the experimental result. The mean numerical deviation from experimental performance is found to be  $259^{\circ}C$ .

Much in the same fashion as Data Set I, Panel b) of Figure 6.13 fares better in replicating the experimental behavior of Data Set II than Panel a). Under quantitative inspection, the numerical solution closely approximates the experimental thermal response, capturing several sudden changes. In particular, the experimental behavior resulting from the sudden power drop occurring at 3000 seconds is surprisingly well predicted. In general, the majority of the transient response, through approximately 5000 seconds, is accurately simulated. Unfortunately, the overshoot in steady-state temperature found in the numerical solution produces a mean deviation from experimental data of  $201^{\circ}C$ .

### Transient Response: Data Set II, Center Position

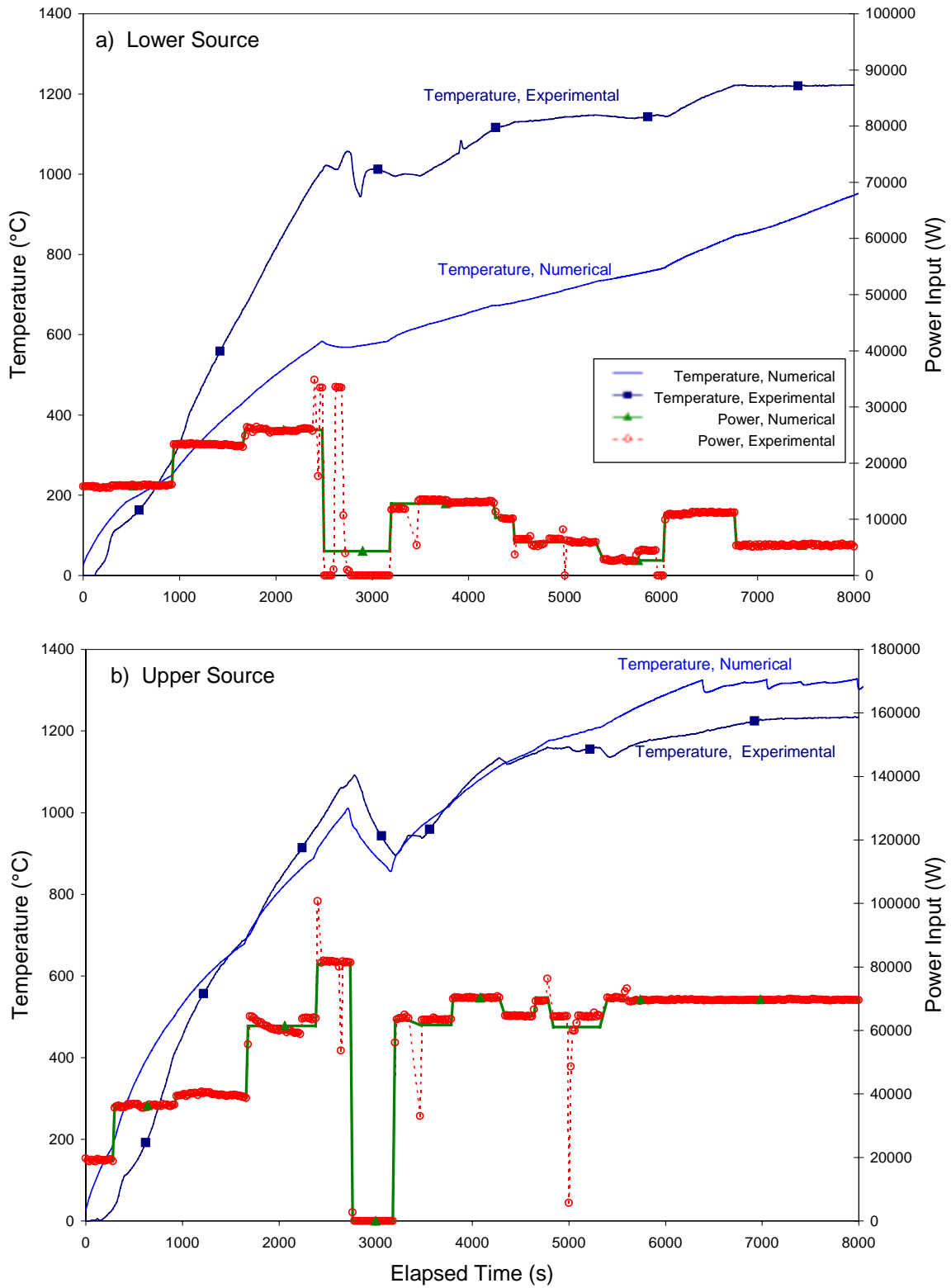


Figure 6.13 Numerical Simulation of Data Set II Transient Response, Center

As with Data Set I, figures depicting the axial and spatial temperature distributions for the simulations of Data Set II are provided for qualitative review and later comparison.

Figure 6.14 presents the axial temperature distribution for Data Set II experimental and numerical results. Figure 6.15 renders the complementary spatial temperature distribution.

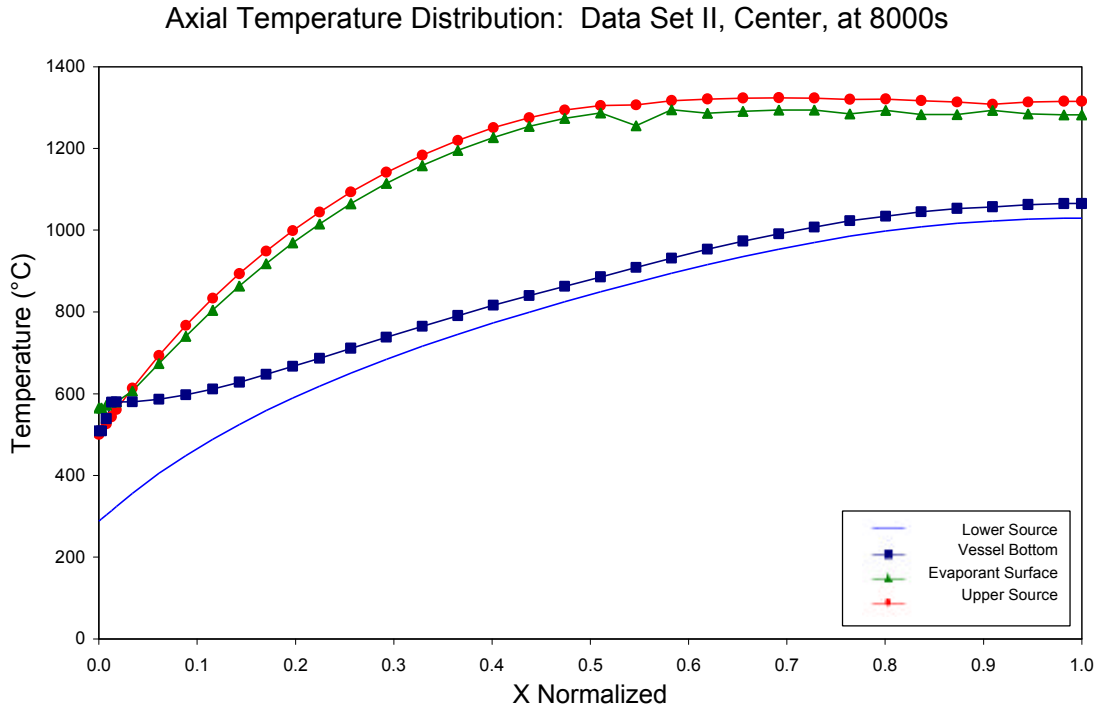


Figure 6.14 Axial Temperature Distribution, Data Set II, 8000 seconds

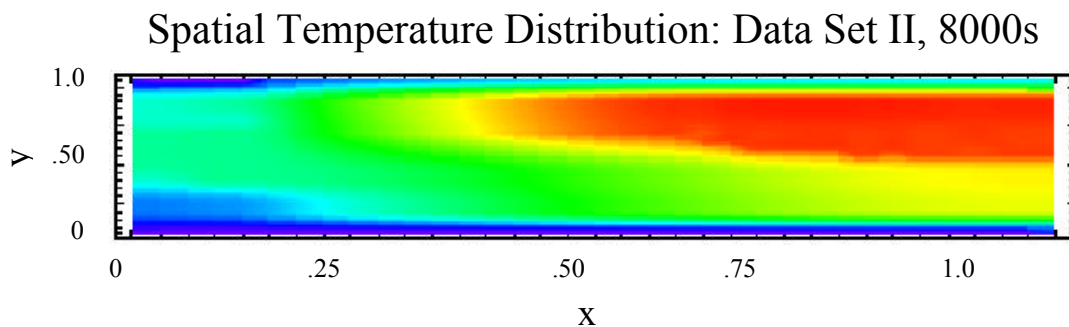


Figure 6.15 Spatial Temperature Distribution, Data Set II, 8000 seconds

### **6.1.6 Summary: Validity of the Numerical Solution**

Grid, convergence criteria, and stability criteria refinement are implemented to ensure the numerical validity of the mathematical model utilized to generate the numerical solution. Additionally, case studies and experimental validation are employed to verify the evolved model of the physical vaporization system. Each of these studies lends confidence to a particular aspect of solution validity.

#### ***Grid Refinement***

Grid refinement tests are presented within section 6.1.1 as Figures 6.1 and 6.2. The qualitative convergence of successively finer, more dense, nodal networks permits the affirmation that the densest, 64X the Coarse grid density, system offers a grid independent solution. Thus, by implementing this grid structure, the results obtained will indicate a spatially valid solution, virtually unchanged with subsequent grid refinement. However, for the reason of efficiency cited within section 6.1.1, a less dense construction of 4X Coarse grid density is selected. Considering, the computed deviations from the converged solution scheme of 64X Coarse grid density of  $\bar{d} = 46.2$  for the upper heat source and  $\bar{d} = 8.90$ , the largest tallied deviation is but 4% of the experimental full-scale temperature. For these reasons, the selection of the 4X Coarse grid density is deemed sufficiently accurate to attain the goals of this investigation.

#### ***Convergence Criteria***

Section 6.1.2 relates the outcome of convergence criteria refinement within the framework of the numerical solution. Proper asymptotic behavior of the responses utilizing increasingly more-stringent convergence criteria typifies an iteratively converged solution. Observing these results as presented in Figures 6.3 and 6.4, sufficient convergence is certainly evident. The data generated by all but the most relaxed criteria

are virtually indistinguishable. Hence, one concludes that the utilization of a computationally efficient convergence criteria of  $10^{-4}$  is of more than ample accuracy.

### ***Time Dependence of Model Stability***

The critical role of time-step selection is clearly demonstrated in section 6.1.3. Results indicate desirable and undesirable solution performance based on time-step size. As discussed within this section, for the time scale and temperature range germane to this study, all but the largest time-step provide a reasonably stable solution. In each case, the practice of employing a larger time-step in the early part of the solution, and reducing this number to “stable” size before instabilities ensue, is faithfully used. However, noting the minor oscillation discussed within this section, it is realized that utility of the stability criteria must be exploited. In other words, care must be exercised in selecting a point sufficiently early in the solution so that the reduction of the speed-enhancing time-step precedes any instability. Acknowledging that this improvement was initiated prior to further simulations, the computed stable time step and reduction method are considered valid within the confines of this project.

### ***Case Studies***

Section 6.1.4 portrays the simulated results of five simplified case studies. Each case evaluates the numerical simulation of an isolated particular aspect of the model physics. Applicable results are presented as Figures 6.6 and 6.7.

Case 0.0.0 examines the numerical simulation resulting from a null input set. The outcome parallels expectations of a null response. Hence, the numerical model properly simulates an input condition comprising zero heat input and zero heat loss.

Case 1.0.1 tests whether or not the numerical solution produces the correct cooling trend when subjected to only convective boundary conditions. As the simulations of Figures 6.6 and 6.7 illustrate, the derived numerical model correctly replicates the performance induced by purely convective boundary conditions.

Case 1.1.1 serves to determine the accuracy of radiative cooling emulations. Again, as with case 1.0.1, correct trend prediction is obtained from the numerical model.

The inputs of case 2.2.0 provide a full complement of heat inputs similar to those utilized in experimental validation. Figures 6.6 and 6.7 portray the expected heating trends for such an input domain. Hence, validity of heat input methodology is exhibited, while credence is gained for the application of internal radiation.

Case study 3.0.1 depicts the numerical solution performance subjected to a point heat source located near the midpoint of the upper heat source. This scenario is designed to further verify the application of internal radiation, while insuring proper evaporant heating and depletion. Acknowledging the columnar formulation of the internal radiation model, this behavior is correctly predicted. Hence, the validity of the evaporation and internal radiation mechanism is upheld.

### ***Experimental Validation***

As the evolved numerical solution is to be implemented in the prediction of hypothetical improvements, verification of the solution against experimental data offers confidence of validity. Section 6.1.5 explains the results of numerical simulations generated in comparison to experimental data having virtually identical inputs.

The results of the numerical response to the inputs of Data Set I are presented as Figures 6.10, 6.11, and 6.12. While, Figures 6.13, 6.14, and 6.15 portray the results obtained from the simulation of the inputs comprising Data Set II.

In general, the accuracy of lower heat source predictions is suspect. Although the proper upward heating trend is shown, the simulated transient responses are removed from the realm of correct experimental behavior. Moreover, the mean deviations from experimental data are  $\bar{d} = 269^{\circ}C$  and  $\bar{d} = 259^{\circ}C$ , for the Data Set I and Data Set II, respectively. This represents an offset of 21 % from the intended performance.

With respect to the simulated upper heat source behavior, predictions for both Data Set I and Data Set II exhibited improvement over that of the lower heat source. Concisely, both solutions offered qualitatively sound tracking of the experimental solution. If not for the overt offset in steady-state temperature predicted by the Data Set II numerical model, the mean deviation computed for Data Set II as  $\bar{d} = 201^{\circ}C$  would more closely resemble the  $\bar{d} = 132^{\circ}C$  mean deviation obtained from Data Set I.

Another noteworthy feature of these upper heat source transient response simulations is that of the periodic, saw-tooth peaks occurring in the steady-state regime of both simulations. Noting the temperature at their onset,  $T \approx 1570K$ , it becomes evident that this phenomenon is a manifestation of the numerical evaporation scheme, and not attributable to gross physical behavior. Specifically, within the employed numerical model, the depletion of an evaporant node incurs a sudden decrease in temperature of the absorptive evaporant surface, as a colder node beneath is “uncovered”. Hence, the sudden drop in nodal temperature is seen. As the formerly cold node begins heating, more heat is again transferred to its neighbors, until the next-hottest node vaporizes. This behavior is most representative of actual physics. However, in actuality, this process involves much smaller volumes of material being depleted. Consequently, the experimental exhibition of this volume depletion occurs on a much smaller scale, and the subsequent peaks are indistinguishable.

Despite the seemingly large values obtained for the mean deviations from experimental results, the foregoing simulations do ensure that the numerical model is of value in the prediction of hypothetical behavior. In that, recall that a key factor influencing uniformity of deposition is that of the temperature distribution about the upper surface of

the evaporant. Considering the internal radiative coupling of this surface to the emissive lower surface of the upper heat source, the value of the upper heat source predictions is favored over that of the lower heat source. Since these predictions are generally within two significant figures of the experimental simulation, at any given data point, the utility of this numerical solution in predicting accurate system trends is significant.

Thus, considering the aforementioned nature of anticipated model utilization, and the foregoing refinement and validation studies, the implementation of this numerical solution in the evaluation of proposed improvements is most acceptable.

## **6.2 Simulation of Proposed Improvements**

Eight hypothetical improvements are examined. Each case depicts the predicted system performance following a single modification to the existing system structure or operating parameters. In all cases, the design intent is the improvement of the uniformity of the axial temperature distribution. As such, an improvement providing the ideal temperature distribution will yield a perfectly horizontal axial temperature distribution plot. Specifically, a perfectly uniform temperature distribution necessitates a zero-slope, constant-temperature plot. This trait heralds a convenient method of statistical evaluation of proposed improvements.

### **6.2.1 Method of Comparison**

The sample standard deviation is defined by Beckwith and Marangoni (1990) as:

$$\mathbf{s} = \sqrt{\frac{\sum_{i=1}^n x_i^2 - n\bar{x}^2}{n-1}}, \quad [6.2]$$

where  $s$  signifies sample standard deviation,  $x_i$  represents the individual data values,  $\bar{x}$  is the sample mean, and  $n$  denotes the number of data points in the sample. This quantity cumulatively compares each data point within the sample to the sample mean. As such, a quantification of the scatter about a constant value is obtained. The mean for each possible improvement is taken to be the ideal temperature distribution. Thus, a numerical value describing the closeness of each simulation to a perfect solution at its mean is computed. Exploiting this method, hypothetical improvements may be evaluated based on their performance in comparison to the existing system represented by the inputs of Data Set II. The simulated axial temperature distribution for the lower heat source of Data Set II exhibits a standard deviation of  $s = 261^\circ C$ , while the simulated upper heat source distribution portrays a standard deviation of  $s = 302^\circ C$ . Those modifications yielding significant reduction in standard deviation when compared to the existing system are considered satisfactory. Hypothetical improvements failing to produce sufficiently reduced standard deviations are classified as unsatisfactory.

## 6.2.2 Unsatisfactory Proposed Improvements

Four potential modifications to the existing system are deemed unsatisfactory by the assessment of their standard deviation. The axial temperature distributions and the accompanying standard deviations for these failed improvements are shown in Figure 6.16, Panels a) and b). As with the foregoing sections, Panel a) depicts the results for the lower source; Panel b) illustrates those for the upper source.

### 1) *4% Oversized Heating System*

This trial examines a four-percent increase in the system length. It is intended to “move” the end effects further from the deposition zone. Yet, it offers a standard deviation of  $s = 230^{\circ}C$  for the lower heat source and  $s = 254^{\circ}C$  for the upper heat source. While certainly an improvement over the existing system, this change, although indicating a potential vein of betterment, does not provide an adequate improvement. The axial distribution for this case is plotted only for the original solution domain.

### 2) *Uniform System, Cooled Sources*

The imposition of a strictly  $y$ -zoned construction is denoted by this improvement case. This possibility eliminates the variant  $x$ -zoned structure at the left end of the system. Intending to reduce end effects, this trial yields a standard deviation of  $s = 262^{\circ}C$  for the lower heat source distribution and  $s = 301^{\circ}C$  with regard to the upper heat source distribution. Hence, this proposal is of little use in the improvement of the vaporization system.

### Unsatisfactory Proposed Improvements: Axial Temperature Distribution, 8000s

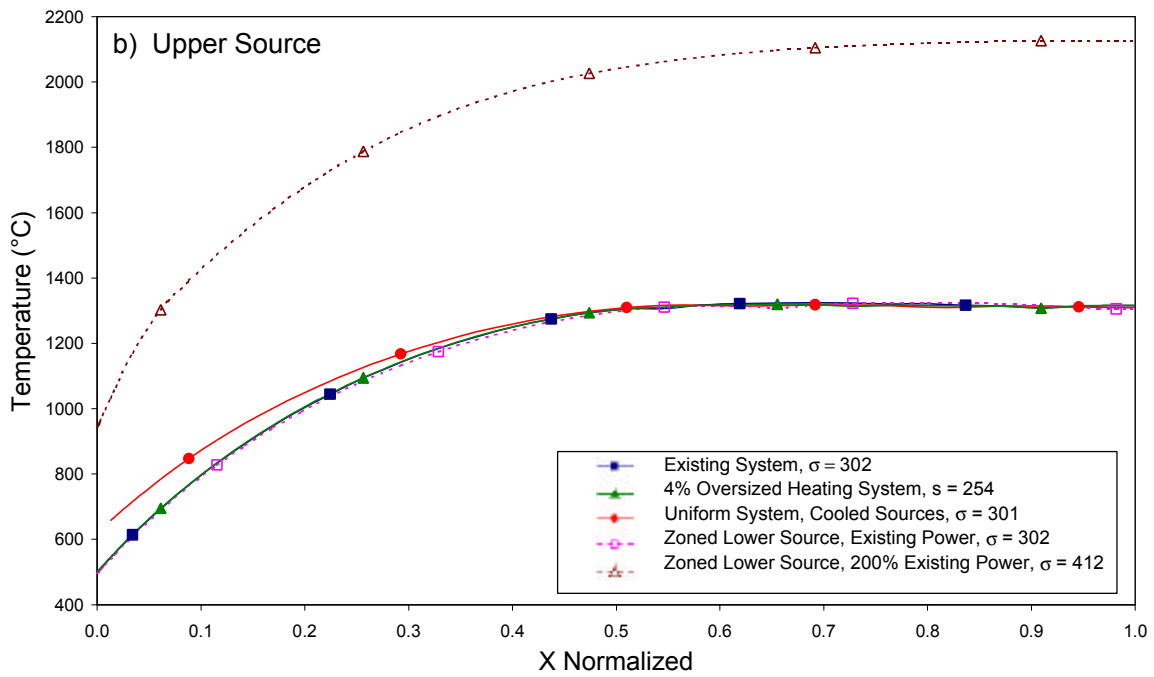
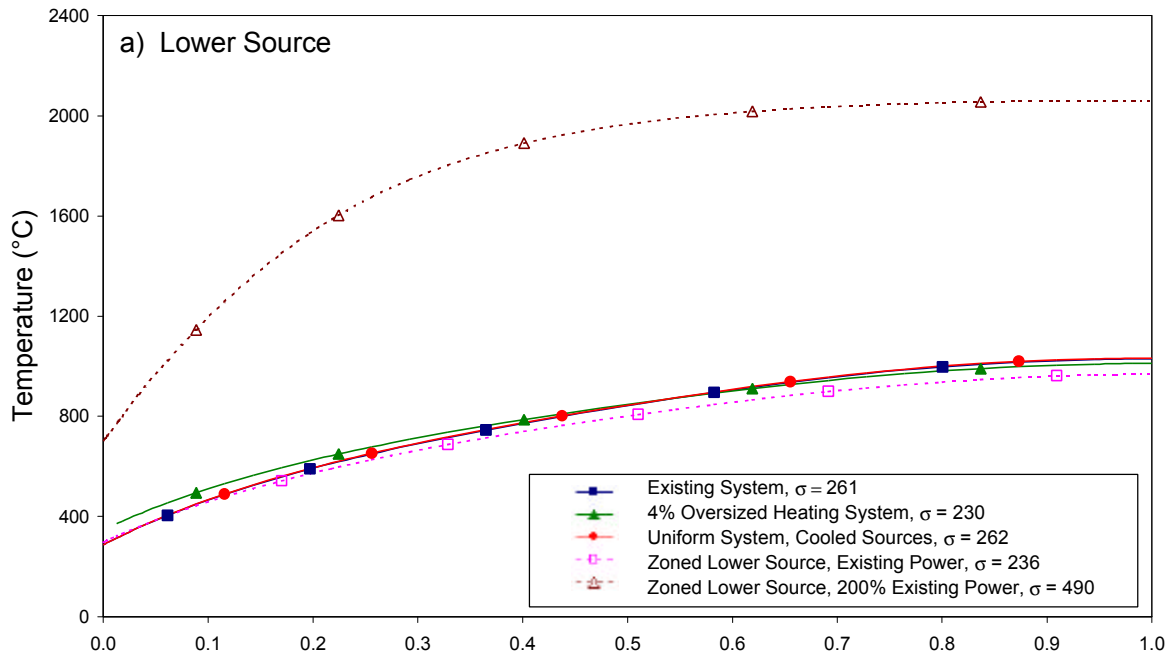


Figure 6.16 Unsatisfactory Proposed Improvements

### 3) *Zoned Lower Source, Existing Power*

The third unsatisfactory improvement case entails a zoned heating system, in which the lower heat source is resized to provide input to only first and second  $x$ -zones. Wherein, the existing power input schedule is applied to a lower heat source resized to fill only these leftmost zones. The remainder of the former lower heat source volume is replaced by insulation. This option provides a lower heat source standard deviation of  $s = 236^{\circ}C$  and a standard deviation for the upper heat source of  $s = 302^{\circ}C$ . This hypothesis also fails to provide ample improvement.

### 4) *Zoned Lower Source, 200% Existing Power*

Finally, the previous suggestion of a Zoned Lower Source is amended by implementing twice the existing lower heat source power input. This simulation exacerbates the nonuniformity of the existing system with standard deviations of  $s = 490^{\circ}C$  and  $s = 412^{\circ}C$ , for the lower heat source distribution and upper heat source distribution, respectively.

### 6.2.3 Satisfactory Proposed Improvements

Four potential modifications are presented as satisfactory improvements, following comparison of their standard deviation to that of the experimental system. The axial temperature distributions and the accompanying standard deviations for these desirable improvements are shown in Figure 6.17, Panels a) and b). As with Figure 6.16, Panel a) depicts the results for the lower source; Panel b) illustrates those for the upper source.

#### 1) *10% Oversized Heating System*

A successful proposed refinement of the existing system entails the imposition of a ten- percent increase in the length of the vaporization system, attained by enlarging the portion removed from the deposition area. The computed standard deviation for the lower heat source distribution is  $s = 151^{\circ}C$  ; for the upper heat source, it is  $s = 197^{\circ}C$  . These are significant improvements over their respective predecessors of  $s = 261^{\circ}C$  and  $s = 302^{\circ}C$  , respectively. The axial distribution for this case is plotted only for the original solution domain.

#### 2) *25% Existing Convection*

Another desirable proposed modification is created by reducing the existing convection coefficient to 25% of the existing value. This change produces striking reductions in standard deviation, with the lower source distribution having  $s = 153^{\circ}C$  , and the upper source distribution exhibiting  $s = 128^{\circ}C$  .

Satisfactory Proposed Improvements:  
Axial Temperature Distribution, 8000s

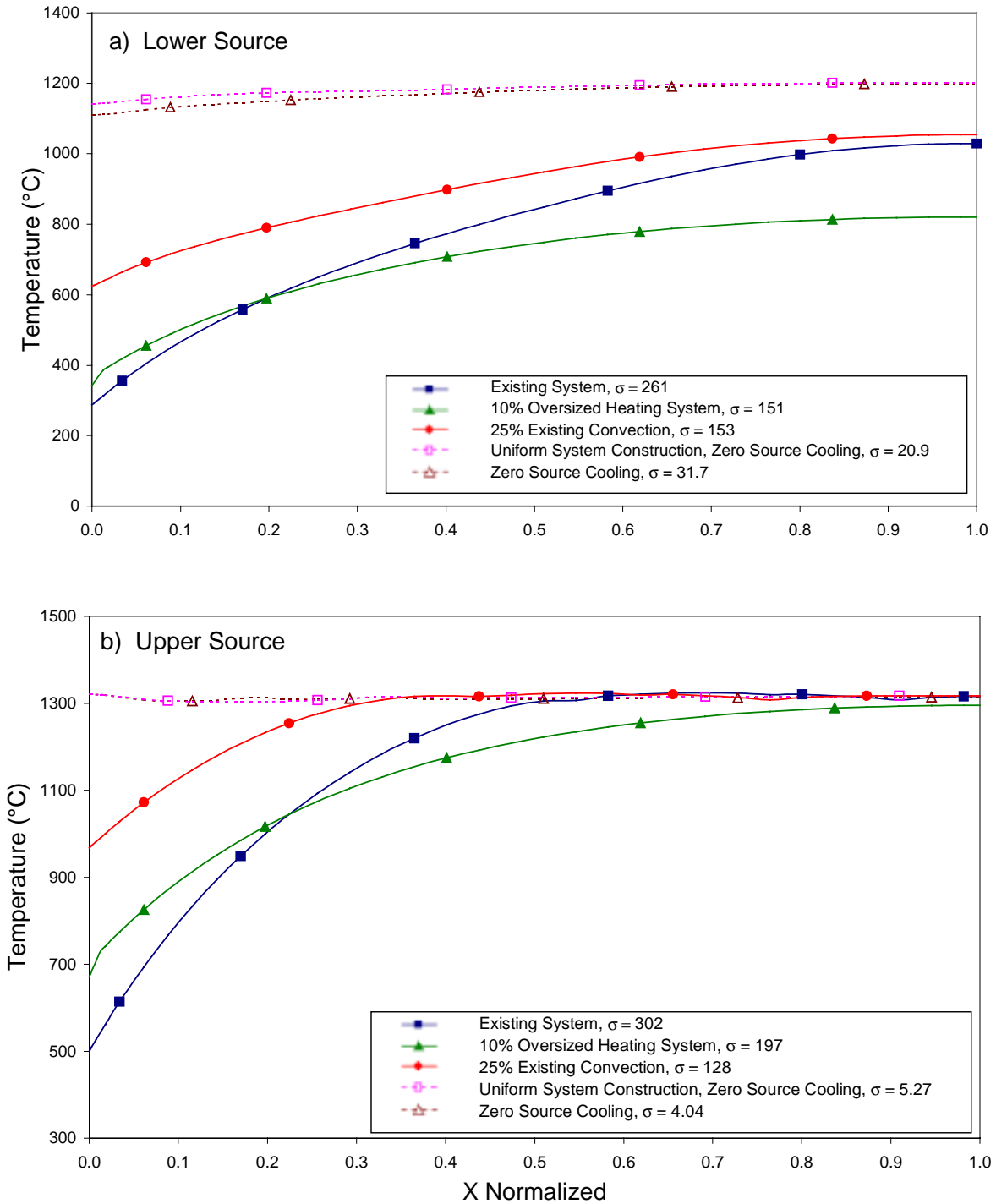


Figure 6.17 Satisfactory Proposed Improvements

### 3) *Uniform System Construction, Zero Source Cooling*

Superior to even the *25% Existing Convection* improvement, this potential enhancement promises substantial advancement in the quest for uniformity. This modification acts upon the *Uniform System Construction* option outlined earlier, removing the convective boundary conditions applied to the left boundaries of the heat sources. In so doing, the standard deviation for the lower heat source axial temperature distribution is reduced to  $s = 20.9^{\circ}C$ ; that of the upper heat source axial temperature distribution becomes  $s = 5.27^{\circ}C$ .

### 4) *Zero Source Cooling*

This final satisfactory potential improvement is actually a simplification of the existing system. Wherein, the sole change imposed is the removal of the convective boundary conditions from the left boundaries of the heat sources. This numerically uncomplicated refurbishment yields another exceptional decrease in standard deviation. In that, the standard deviation describing the lower heat source distribution drops to  $s = 31.7^{\circ}C$ , the standard deviation for the upper heat source distribution becomes a paltry  $s = 4.04^{\circ}C$ .

### *Spatial Temperature Distributions*

Allusion was previously made regarding the qualitative comparison of proposed improvements to the existing system using spatial temperature distributions. These contour plots are included as Figure 6.18. Upon inspection of these renderings, the need for the quantitative comparison of improvements is evidenced by the similarity of the contour graphs.

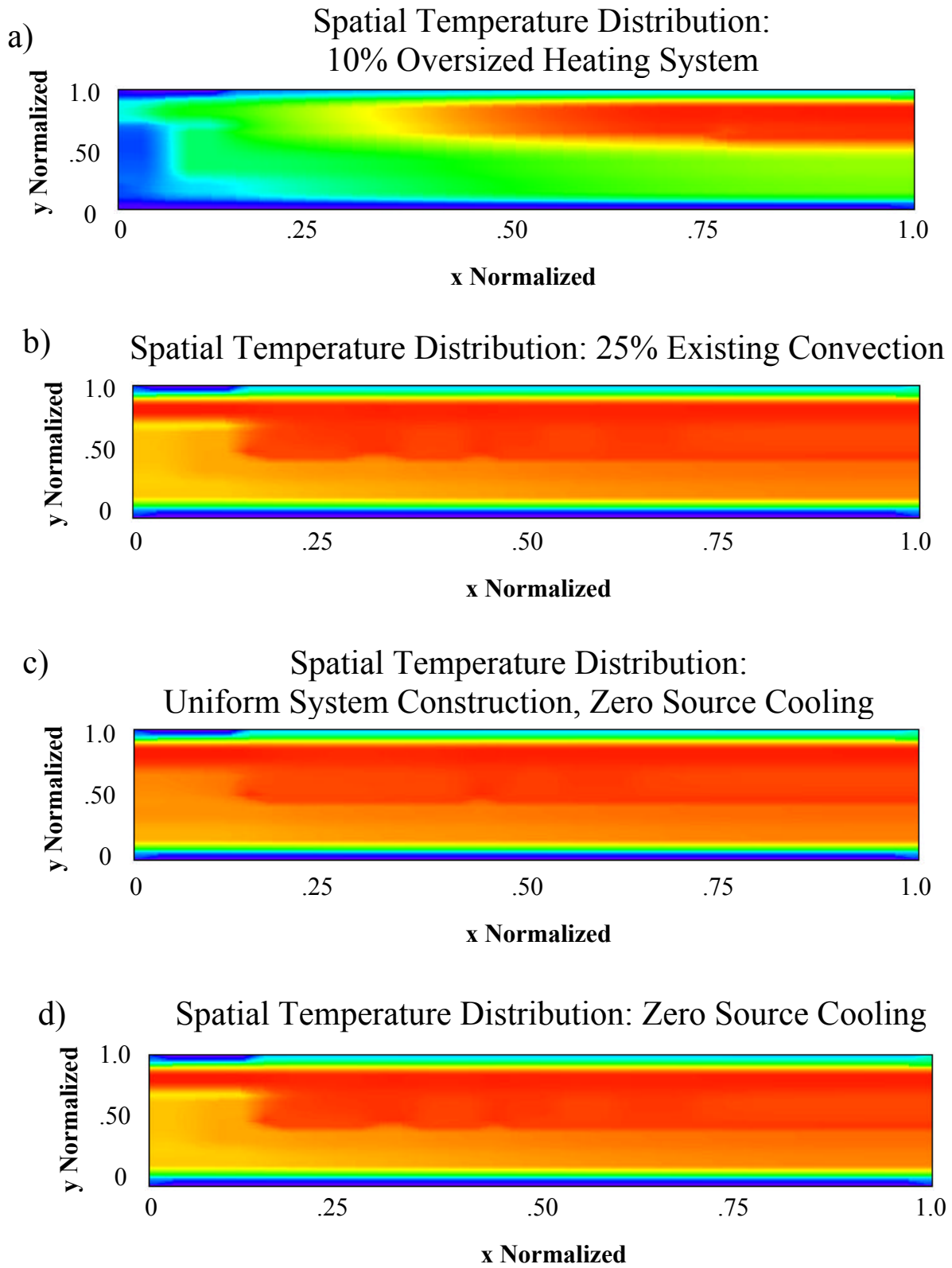


Figure 6.18 Spatial Temperature Distribution: Satisfactory Improvements

## 6.2.4 Summary: Evaluation of Proposed Improvements

Considering the simulations of proposed improvements detailed in section 6.2, several deductions of physical import are readily rendered.

### *Unsatisfactory Improvements*

As previously discussed within section 6.2.2, these simulations yield little or no improvement in axial temperature distribution uniformity, and one, in the case of the *Zoned Lower Source, 200% Existing Power*, produces a significant decrease in predicted uniformity. Both the *Uniform System Construction* case and the *Zoned Lower Source, Existing Power* simulation offer practically zero uniformity improvement. Worthy of note, the *4% Oversized Heating System* provides a modest improvement in uniformity in comparison to the existing system. This performance prompts the investigation of an enhanced version of this trial in the *10% Oversized Heating System* addressed below.

### *Satisfactory Improvements*

The remaining four proposed modifications explored in section 6.2.3 afford substantial enhancements in axial temperature uniformity.

Originating as an iteration following the *4% Oversized Heating System*, the *10% Oversized Heating System* generates improved temperature uniformity across both the upper and lower heat sources. As outlined in section 6.2.3, the computed standard deviation for the lower heat source distribution is  $s = 151^{\circ}C$ ; for the upper heat source, it is  $s = 197^{\circ}C$ . These are significant improvements over their respective existing system predecessors of  $s = 261^{\circ}C$  and  $s = 302^{\circ}C$ , respectively.

Even better results are demonstrated by the *25% Existing Convection* case. Wherein, this improvement boasts a reduction in the standard deviation for the upper heat source distribution of more than 57%. Such an enhancement will certainly have a positive impact on coating uniformity. Moreover, the physical implementation of an improvement of this nature is relatively uncomplicated. Hence, the 25% Existing Convection case offers a viable alternative for process enhancement.

A third potential system improvement is defined by *Uniform System Construction, Zero Source Cooling*. This adaptation affords, in the worst case, the realization of a 92% reduction in non-uniformity. Obviously, this possibility seems most attractive regarding process improvement. However, the attainment of such a scenario is a demanding engineering task. Therefore, this improvement is deemed highly desirable, yet difficult to implement. Comparatively, this option offers the largest overall decrease in non-uniformity.

The final potential system modification designed to improve temperature uniformity concerns a simplification of the previously mentioned *Uniform System Construction, Zero Source Cooling* instance. As outlined in section 6.2.3, the *Zero Source Cooling* simulation produces another substantial betterment of uniformity. Similar, yet somewhat, simpler than its predecessor, the utilization of this scenario is problematic due to the rules of energy conservation and electrical power generation. Simply, all power conductors, regardless of construction, exhibit heat generation via their inherent electrical resistivity.

# Chapter 7.0

## Conclusions and Recommendations

Summarizing the contributions offered by an investigation such as that portrayed within this thesis, it is most pertinent to address the conclusions drawn from the developed results and relevant recommendations for further study. The following sections submit conclusions and recommendations from those results put forth throughout the course of this project.

### 7.1 Conclusions

Considering the foregoing compilation of results, these conclusions are offered:

- 1) Examining the results of *Grid Refinement*, *Convergence Criteria Refinement*, and the *Stability Investigation*, the mathematical model and numerical solution are deemed parameter-independent.
- 2) Citing the results of the selected *Case Studies*, the mathematical model and numerical solution provide qualitatively sound simulations of the independent physical mechanisms explored.
- 3) Noting that the thermal behavior of the upper heat source more closely correlates to coating uniformity than the lower heat source, the *Experimental Validation* studies offer ample confidence that the mathematical model and numerical solution closely replicate the operation of the physical system.

- 4) Inferring from the above conclusion, the *Treatment of Voids*, *Treatment of Evaporation*, and modeling in *Internal Radiation* provide sufficiently accurate incorporation of their respective physical phenomena.
- 5) The enhancement in uniformity obtained by oversizing the heating system is significant. Note that as the heating system length is increased beyond that of the solution domain, the power density decreases. Thus, the power input to the domain is also diminished despite gains in uniformity. A compromise between power input and uniformity must be sought.
- 6) From the results of *Simulation of Proposed Improvements*, the benefit of minimizing heat source direct-cooling is most obvious. Although this means of improvement is intuitive, the degree of influence produced by specific changes in the convection coefficient is more abstract. A total elimination of cooling at the heat source ends yields a nearly optimal solution. However, the impracticality of an uncooled electrical conductor requires a moderation of this case. A compromise between the *Zero Source Cooling* extreme and the *25% Existing Convection* case would afford highly desirable, yet physically meaningful results.

## 7.2 Recommendations

Acknowledging the ongoing nature of research studies, it is pertinent to address recommendations regarding future work on this investigation.

With respect to the acquisition of data, two particular modifications would improve result and model quality. Primarily, a contemporary data acquisition system of proper design may enhance the quality of experimental data utilized for comparison. Proper voltage and current measurement, reliable thermocouple placement, and a larger array of axial data points will substantially enhance overall quality. Secondly, the accurate experimental determination of all critical material properties will surely add to the validity of any numerical model.

Next, reflection is given upon renovations to the modeling of the physical system. Therein, three applicable changes affecting model validity and accuracy are proposed.

- 1) Modify the model of evaporation to include incremental mass depletion.
- 2) Regenerate the solution as a three-dimensional system to account for the missing gradients discussed in section 6.1.5 or incorporate another lumped term to address this behavior.
- 3) Consider the refinement of the prescribed internal radiation model to include multiple interactive faces and non-columnar radiation paths.

Finally, four improvements entailing the numerical solution are notable.

- 1) Subsequent improvements in grid density, although not effecting grid refinement convergence, will tend to smooth the saw-tooth behavior evident in the present numerical simulations.

- 2) A rigorous formulation for time-step reduction or stretching should be investigated and implemented. This concept is commonplace within applicable literature; further research is recommended.
- 3) Consideration should be given to recoding the numerical solution program to incorporate a matrix-based solution scheme. The current multi-dimensional, subscripted, tabular format is excessively slow in comparison. Such an enhancement would pay large dividends in computational efficiency.
- 4) Further study on this topic might include a numerical optimization scheme to provide mathematically justified improvements to the system construction. Such a method would rigorously investigate possible system enhancements by systematically varying key parameters.

## References

Beckwith, T. J., and Marangoni, R. D. Mechanical Measurements. 4<sup>th</sup> ed. Massachusetts: Addison-Wesley, 1990.

Betts, P. L., and Kang, J. S. "On the Accuracy of the Boundary Element Method for Three-dimensional Conduction Problems." Numerical Methods in Heat Transfer. v.2. Ed. R. W. Lewis, K. Morgan, and B. A. Schrefler. New York: Wiley, 1981. 275-302.

Bobrow, Leonard S. Funamentals of Electrical Engineering. Fort Worth: Holt, Rinehart, and Winston, 1985.

Chapman, Brian, and Mangano, Stefano. "Introduction to Sputtering." Handbook of Thin-Film Deposition Processes and Techniques. Ed. Klaus K. Schuegraf. Park Ridge, New Jersey: Noyes, 1988. 291-317.

Corning Engineering Laboratory Services. "Differential Thermal Analysis." Thermal Properties Analysis. Corning, 1998. §12.1.1-12.1.6

Daniels, T. Thermal Analysis. London: Kogan Page, 1973.

Dusinberre, George Merrick. Heat Transfer Calculations by Finite Differences. Scranton: International Textbook, 1961.

Incropera, Frank P., and DeWitt, David P. Fundamentals of Heat Transfer. 3<sup>rd</sup> ed. New York: Wiley, 1990.

International Nuclear Safety Center. "Recommended Enthalpy Increments and Heat Capacities" in: [www.insc.anl.gov/matprop](http://www.insc.anl.gov/matprop). Argonne National Laboratory. 2000.

Kern, Werner, and Schuegraf, Klaus K. “Deposition Technologies and Applications: Introduction and Overview.” Handbook of Thin-Film Deposition Processes and Techniques. Ed. Klaus K. Schuegraf. Park Ridge, New Jersey: Noyes, 1988. 1-25.

Knight, Charles E., Jr. Introducing the Finite Element Method in Mechanical Design. Blacksburg: 1993.

Knodle, Walter S., and Chow, Robert. “Molecular Beam Epitaxy: Equipment and Practice.” Handbook of Thin-Film Deposition Processes and Techniques. Ed. Klaus K. Schuegraf. Park Ridge, New Jersey: Noyes, 1988. 170-233.

Konuma, Mitsuharu. Film Deposition by Plasma Techniques. Springer Series on Atoms and Plasmas 10. New York: Springer-Verlag, 1992.

Modest, Micheal F. Radiative Heat Transfer. New York: McGraw-Hill, 1993.

Ozisik, M. Necati. Finite Difference Methods in Heat Transfer. Ann Arbor: CRC Press, 1994.

Patankar, Suhas V. Computation of Conduction and Duct Flow Heat Transfer. Maple Grove: Innovative Research, 1991.

Perry, Robert H., and Green, Don W. Perry’s Chemical Engineers’ Handbook. 6<sup>th</sup> ed. New York: McGraw-Hill, 1984. 3-129.

Pitt, Valerie H. “Epitaxy.” Penguin Dictionary of Physics. Lawrence Urdang Associates Ltd. 1987 ed. 137.

Pope, M. I., and Judd, M. D. Differential Thermal Analysis: A Guide to the Technique and Its Applications. Bellmawr, New Jersey: Heyden, 1977.

Poulikakos, D. Conduction Heat Transfer. Englewood Cliffs: Prentice, 1994.

Powell, Carroll F. "Physical Vapor Deposition." Vapor Deposition. Ed. Carroll F. Powell, Joseph H. Oxley, and John M. Blocher, Jr. New York: Wiley, 1966. 221-248.

Powell, Carroll F. "Chemically Deposited Nonmetals." Vapor Deposition. Ed. Carroll F. Powell, Joseph H. Oxley, and John M. Blocher, Jr. New York: Wiley, 1966. 343-420.

Real, Vila, and Oliveira, Magalhaes. "Use of Polynomial Functions for Hierarchical Improvement of the Finite Element Solution for Transient Heat Conduction Problems with High Thermal Gradients." Numerical Methods in Thermal Problems. Eds. R. W. Lewis and K. Morgan. Proc. of the Sixth International Conference. 3-7 July 1989. Swinsea, U.K.: Pineridge, 1989. Vol.IV. Part 1. 227-240.

Rossi, Ronald C. "Low Pressure Chemical Vapor Deposition." Handbook of Thin-Film Deposition Processes and Techniques. Ed. Klaus K. Schuegraf. Park Ridge, New Jersey: Noyes, 1988. 80-111.

Runyan, Walter R. "Electronic Materials." Vapor Deposition. Ed. Carroll F. Powell, Joseph H. Oxley, and John M. Blocher, Jr. New York: Wiley, 1966. 593-611.

Schuegraf, Klaus K. Preface. Handbook of Thin-Film Deposition Processes and Techniques. Ed. Klaus K. Schuegraf. Park Ridge, New Jersey: Noyes, 1988. v-vi.

Singh, K. M., and Kalra, M. S. "A Least Squares Time Integration Scheme for the Dual Reciprocity BEM in Transient Heat Conduction." Numerical Methods in Thermal Problems. Ed. R. W. Lewis and K. Morgan. Proc. of the Sixth International Conference. 3-7 July 1989. Swinsea, U.K.: Pineridge, 1989. Vol.IV. Part 1. 221-226.

Smith, Donald L. Thin Film Deposition: Principles and Practice. New York: McGraw-Hill, 1995.

Stuart, R. V. Vacuum Technology, Thin Films, and Sputtering. New York: Academic Press, 1983.

Sunden, Bengt. "A Numerical Investigation of the Transient Temperature Distribution in a Three-layered Solid with Time-varying Boundary Conditions." Numerical Methods in Thermal Problems. Ed. R. W. Lewis and K. Morgan. Proc. of the Sixth International Conference. 3-7 July 1989. Swinsea, U.K.: Pineridge, 1989. Vol.IV. Part 1. 111-119.

Thornton, Earl A., Dechaumphai, Pramote, and Tamma, Kumar K. "Exact Finite Element Solutions for Linear Steady-state Thermal Problems." Numerical Methods in Heat Transfer. v.2. Ed. R. W. Lewis, K. Morgan, and B. A. Schrefler. New York: Wiley, 1981. 37-52.

Ullrich, Osmar A. "Optical Coatings." Vapor Deposition. Ed. Carroll F. Powell, Joseph H. Oxley, and John M. Blocher, Jr. New York: Wiley, 1966. 549-578.

Vick, Brian. "Finite Difference Method." Class Notes, Virginia Polytechnic Institute and State University. Blacksburg: 2000.

Wasa, Kiyotaka, and Hayakawa, Shigeru. Handbook of Sputter Deposition Technology. New Jersey: Noyes, 1992.

Wolfram Research, Inc. Mathematica, Version 3.0. Illinois: Wolfram Research, 1996.

Wolfram Research, Inc. [www.support.wolfram.com](http://www.support.wolfram.com). "How do I write a matrix of numbers to a file?" Illinois: Wolfram Research, 2000.

Wrobel, L. C., and Brebbia, C. A. "Boundary Elements in Thermal Problems." Numerical Methods in Heat Transfer. v.1. Ed. R. W. Lewis, K. Morgan, and O. C. Zienkiewicz. New York: Wiley, 1981. 91-114.

Zienkiewicz, O. C. "Finite Element Methods in Thermal Problems." Numerical Methods in Heat Transfer. v.1. Ed. R. W. Lewis, K. Morgan, and O. C. Zienkiewicz. New York: Wiley, 1981. 1-26.

# **Appendix A**

## **Tabular Property Data**

The following appendix contains the tabular data utilized to obtain temperature-dependent material property functions from nonlinear curve fits.

Table A1 Heater Property Data

Heat Source Properties			
T (C)	k (W/m K)	T (K)	Cp (J/kg K)
20	195.3	298	711.0
100	207.4	300	715.0
200	219.5	350	848.0
400	236.7	400	982.0
600	238.5	450	1108.0
800	224.6	500	1220.0
1000	210.8	600	1404.0
1200	202.2	700	1542.0
1400	188.4	800	1648.0
1600	178.0	900	1730.0
1700	169.3	1000	1795.0
1800	165.9	1100	1848.0
(Manuf.Data)		1200	1892.0
		1300	1929.0
		1400	1961.0
		1500	1988.0
		1600	2013.0
		1700	2035.0
		1800	2055.0
		1900	2073.0
		2000	2090.0
(INSC Data)			

Table A2 Insulation Property Data

Insulation Properties				
T (C)	k (W/m K)		T (K)	Cp (J / kg K)
250	0.09		298	774.8
525	0.12		400	919.9
800	0.16		600	1068.0
1075	0.19		800	1167.8
1350	0.23		1000	1253.5
1650	0.27		1200	1333.7
			1400	1411.3
			1600	1487.6
			1800	1563.0

# **Appendix B**

## **DTA Data**

The following appendix includes the raw DTA plot and the reduction utilized in the generation of a temperature-dependent function for the evaporant specific heat capacity.

**LABORATORY ANALYSIS REPORT**

CBL5 Client No.: 275227-001

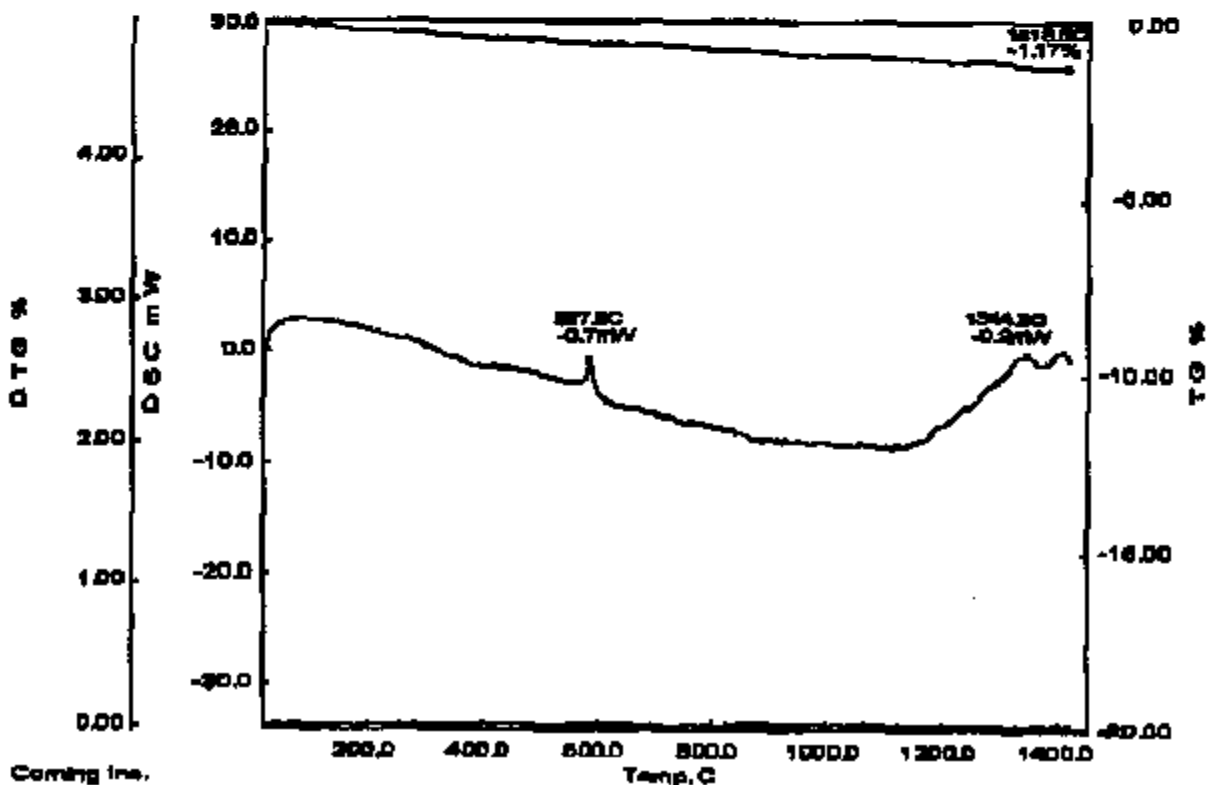
**Exhibit A : Thermal Gravimetric (TGA)/Differential Thermal (DTA) Analysis**

**Sample Description:**

Sample 1: Received 3-21-00

Folder No.: 33716-00

<< TGA/DTA >>  
Date Name: DDTGA1-0005  
Date: 07/22/00 10:00  
Sample: GRANULAR  
Release: A200  
Temperature Program: C] [Rate] [min] [Sec]  
1 20. 100 10 0 2  
Comments:  
Operator MJL  
Folder 33716  
B. BROZOVIC  
15.129 mg  
10 mg



## Derivation of $C_{evap}(T)$ from DTA Data

Taking the evaporant sample as the control volume, and assuming perfect heat transfer to the sample, the heat absorbed by the evaporant mass is:

$$q = \rho V C \frac{dT}{dt};$$

where:  $\rho$  represents mass density,

$V$  signifies volume,

$C$  denotes heat capacity, and

$\frac{dT}{dt}$  indicates the rate of temperature change of the control volume.

With regard to the DTA testing of interest, the following may be applied:

$\rho V = m$ , the mass of the sample being analyzed, [=]kg ,

$\frac{dT}{dt} \equiv \frac{\Delta T}{\Delta t}$ , the heating rate of the analysis experiment, [=] $\frac{K}{s}$  ,

$q$  is the output from the DTA, [=]mW , and

$C$  is the heat capacity of the sample, [=] $\frac{J}{kg \cdot K}$  .

Rearranging:

$$C = \frac{q}{\rho V \frac{dT}{dt}} = \frac{q}{m \frac{dT}{dt}},$$

Inserting DTA Results:

$$C(q_{DTA}) = 396.6 \cdot q_{DTA} \left( \frac{J}{kg \cdot K} \right) .$$

Starting with the data, a third order polynomial fit to the raw DTA data yields:

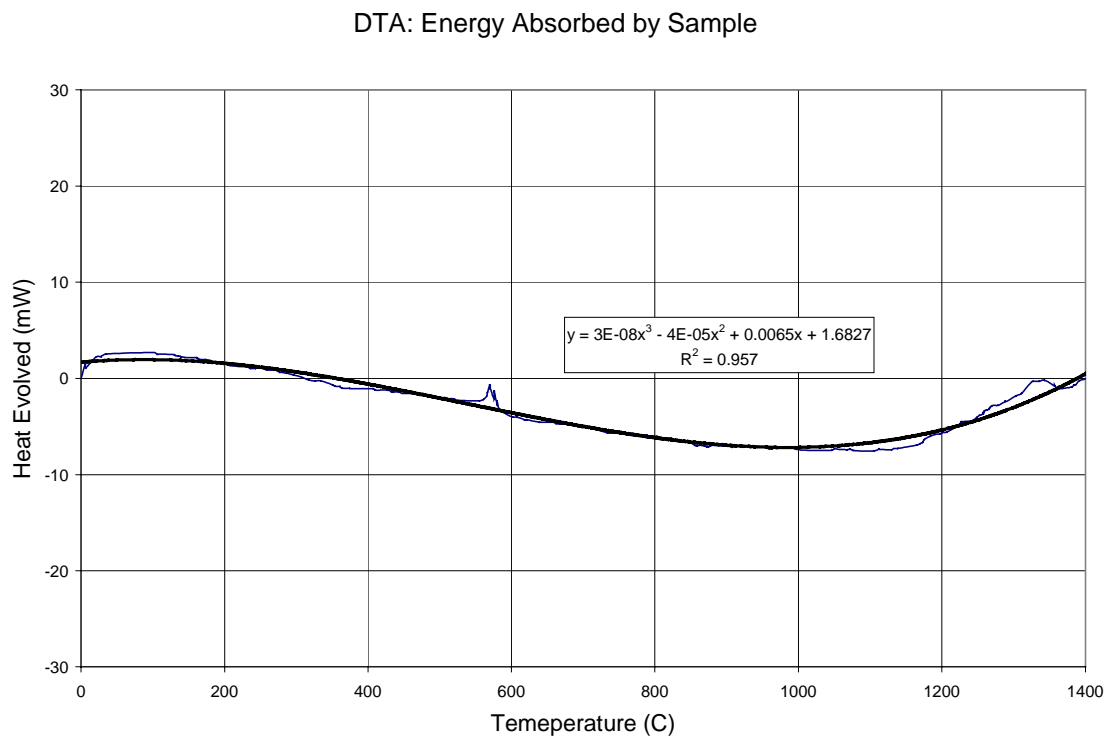


Figure B1 DTA: Energy Absorbed by Sample

Considering only the data at or above 25 °C (300K) and noting that the graphs depict heat evolved, the equation must be negated to obtain heat input:

$$q_{DTA}(T) = -3 \cdot 10^{-8} T^3 + 5 \cdot 10^{-5} T^2 - 0.0129T$$

Combining equations and converting to common units, a relation for  $C_p(T)$  may be acquired:

$$C_p(T) = -1.2 \cdot 10^{-5} T^3 + 0.0314 \cdot T^2 - 21.80 \cdot T + 4418$$

This equation is plotted as:

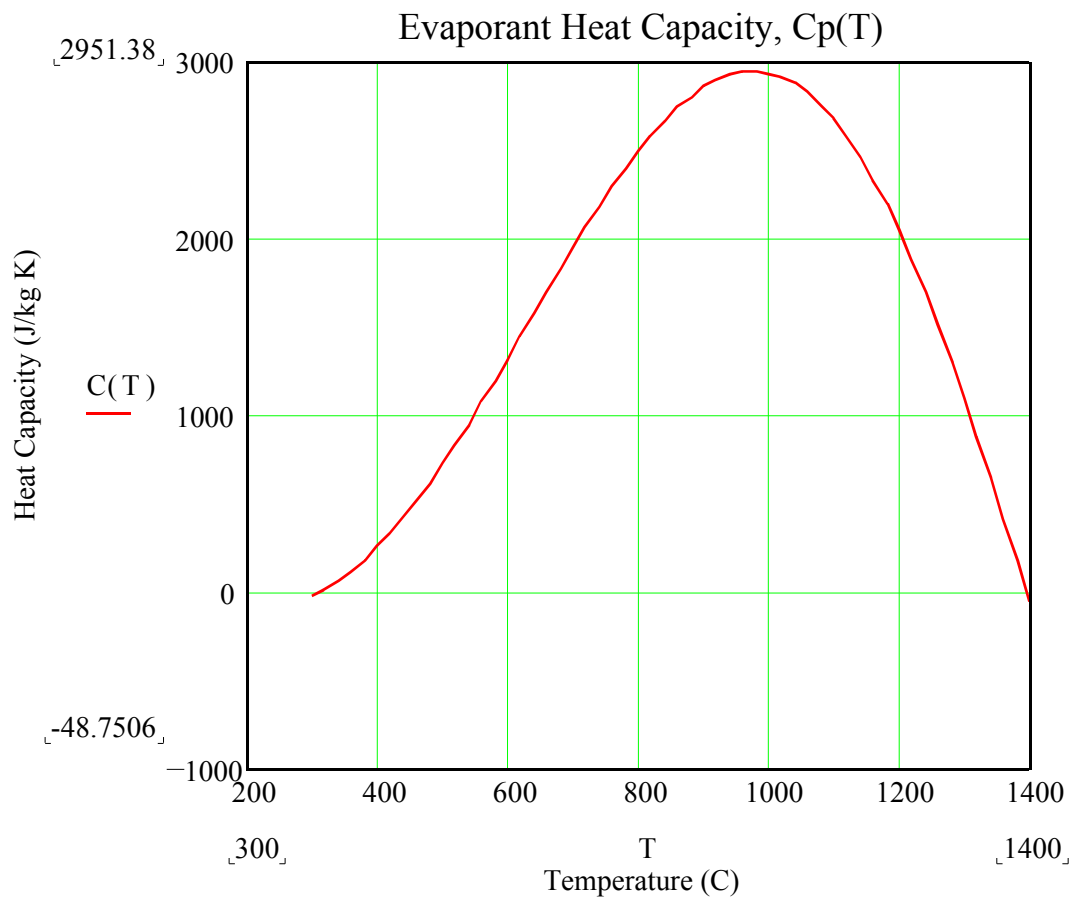


Figure B2 MathCAD Plot of Evaporant Heat Capacity

# **Appendix C**

## **Effective Convection Coefficient**

This appendix details the computation of the effective convection coefficient utilized within the foregoing numerical solution.

## Effective Convection Coefficient

Operations Data obtained from the physical system, for the cooling water:

$$\begin{array}{lll}
 Q \approx 1.26 \cdot 10^{-4} \frac{m^3}{s} & \mathbf{r} = 997 \frac{kg}{m^3} & Pr = 5.83 \\
 D_h = 0.015m & \mathbf{m} = 8.55 \cdot 10^{-4} \frac{N \cdot s}{m^2} & k = 0.613 \frac{W}{m \cdot K}
 \end{array}$$

Where:  $D_h = \frac{4A_{cs}}{P_w}$ , [4.3]

The Reynold's Number is found from:

$$\begin{aligned}
 Re_{D_h} &= \frac{u_m D_h}{\mathbf{n}} = \frac{\mathbf{r} u_m D_h}{\mathbf{m}} & [4.6] \\
 Re_{D_h} &= \frac{997 \frac{kg}{m^3} (0.4 \frac{m}{s}) 0.015m}{8.55 \cdot 10^{-4} \frac{N \cdot s}{m^2}} = 6996 & \text{(turbulent)}
 \end{aligned}$$

Utilizing the Gnielinski correlation:

$$\begin{aligned}
 Nu_{D_h} &= \frac{\left(\frac{f}{8}\right)(Re_{D_h} - 1000)Pr}{1 + 12.7\left(\frac{f}{8}\right)^{1/2}\left(Pr^{2/3} - 1\right)} & [4.4] \\
 Nu_{D_h} &= \frac{(0.026/8)(6680 - 1000)5.83}{1 + 12.7(0.026/8)^{1/2}(5.83^{2/3} - 1)}
 \end{aligned}$$

$$\underline{\underline{Nu_{D_h} = 40.1}}$$

Similarly, using Dittus-Boelter:

$$Nu_{D_h} = 0.023 Re_{D_h}^{4/5} Pr^n \quad [4.5]$$

$$Nu_{D_h} = 0.023(6680)^{4/5} 5.83^{0.4}$$

$$\underline{\underline{Nu_{D_h} = 53.4}}$$

Averaging the two:

$$\boxed{\bar{Nu}_{D_h} = 46.8}$$

Invoking equation 2.4:

$$Nu = \frac{hL}{k} \quad [2.4]$$

Substituting the characteristic length and average Nusselt value while instating  $h_{eff}$ :

$$\bar{Nu}_{D_h} = \frac{h_{eff} D_h}{k}$$

Rearranging:

$$h_{eff} = \frac{k \bar{Nu}_{D_h}}{D_h} = \frac{0.613 \frac{W}{m \cdot K} (46.8)}{0.015m}$$

Affords the employed value for  $h_{eff}$ :

$$\boxed{h_{eff} = 1916 \approx 1900 \frac{W}{m^2 \cdot K}}$$

# Appendix D

## Lumping in the z-Direction

This appendix contains the derivation of  $q_{in}$ , the amount of lateral heat input realized by the system.

# Lumping in the z-Direction

Begin with Figure 4.11:

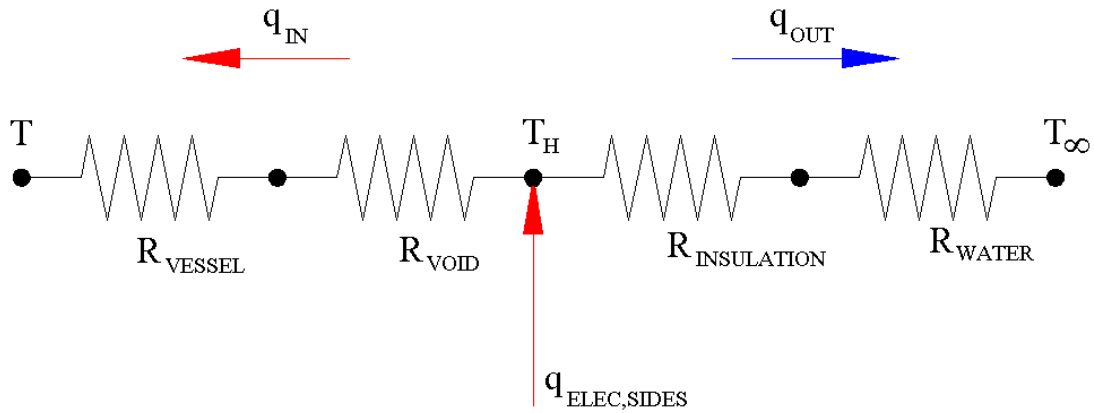


Figure D4.11 Equivalent Network Resistances, Lumping in the z-Direction

Energy Balance on Lower Heat Source, Lateral Input Junction:

$$(1) \quad q_{ELEC,SIDES} = q_{IN} + q_{OUT}$$

Portion of Lateral Electric Heating Input to System:

$$(2) \quad q_{IN} = \frac{T_h - T}{R_{VOID} + R_{VESSEL}}$$

Portion of Lateral Electric Heating Lost to Convection in Water Jacket:

$$(3) \quad q_{OUT} = \frac{T_h - T_\infty}{R_{INSULATION} + R_{WATER}}$$

Substituting (2) and (3) into (1):

$$(4) \quad q_{ELEC,SIDES} = \frac{T_h - T}{R_{VOID} + R_{VESSEL}} + \frac{T_h - T_\infty}{R_{INSULATION} + R_{WATER}}$$

Defining  $R_{IN}$  and  $R_{OUT}$  :

$$R_{IN} = R_{VOID} + R_{VESSEL}$$

$$R_{OUT} = R_{INSULATION} + R_{WATER}$$

Substituting into (4):

$$(4') \quad q_{ELEC,SIDES} = \frac{T_h - T}{R_{IN}} + \frac{T_h - T_\infty}{R_{OUT}}$$

Solving for  $T_H$  :

$$(5) \quad T_h = \frac{q_{ELEC,SIDES} + \frac{T_\infty}{R_{OUT}} + \frac{T}{R_{IN}}}{\left( \frac{1}{R_{IN}} + \frac{1}{R_{OUT}} \right)}$$

Substitute into equation (2):

$$(6) \quad q_{IN} = \frac{\left[ \frac{q_{ELEC,SIDES} + \frac{T_\infty}{R_{OUT}} + \frac{T}{R_{IN}}}{\left( \frac{1}{R_{IN}} + \frac{1}{R_{OUT}} \right)} \right] - T}{R_{IN}}$$

# **Appendix E**

## **Discretization of Governing Equation**

The following appendix explains the discretization of the governing equation utilized in the numerical solution within.

## Discretization of Governing Equation

$$\int_{t_{p-1}}^{t_p} \int_S \int_W^E \left[ \frac{\partial}{\partial x} \left( k \frac{\partial T}{\partial x} \right) + \frac{\partial}{\partial y} \left( k \frac{\partial T}{\partial y} \right) + Sc(x, y, t) - Sp(x, y, t) T - rC_p \frac{\partial T}{\partial t} \right] dx dy dt = 0$$

$$\int_{t_{p-1}}^{t_p} \int_S \int_W^E \left[ \underbrace{\frac{\partial}{\partial x} \left( k \frac{\partial T}{\partial x} \right)}_I + \underbrace{\frac{\partial}{\partial y} \left( k \frac{\partial T}{\partial y} \right)}_{II} + \underbrace{Sc(x, y, t) - Sp(x, y, t) T}_{III} - \underbrace{rC_p \frac{\partial T}{\partial t}}_{IV} \right] dx dy dt = 0$$

Term I:

$$\int_{t_{p-1}}^{t_p} \int_S \int_W^E \left[ \frac{\partial}{\partial x} \left( k \frac{\partial T}{\partial x} \right) \right] dx dy dt = 0$$

Integrating using discretization:

$$\int_{t_{p-1}}^{t_p} \int_S \left[ \left( k \frac{\partial T}{\partial x} \right)_E - \left( k \frac{\partial T}{\partial x} \right)_W \right] dy dt = 0$$

$$\left[ \left[ \left( k \frac{\partial T}{\partial x} \right)_E - \left( k \frac{\partial T}{\partial x} \right)_W \right] \Delta y \right]_{t_{p-1}}^{t_p} = 0$$

$$\left[ \left( k \frac{\partial T}{\partial x} \right)_E - \left( k \frac{\partial T}{\partial x} \right)_W \right] \Delta y \Delta t_p = 0$$

$$\left[ \left( k \frac{\Delta T}{\Delta x} \right)_E - \left( k \frac{\Delta T}{\Delta x} \right)_W \right] \Delta y \Delta t_p = 0$$

$$I = \left[ k_E \frac{T_{i+1,j,p} - T_{i,j,p}}{\Delta x_E} - k_W \frac{T_{i,j,p} - T_{i-1,j,p}}{\Delta x_W} \right] \Delta y_{i,j} \Delta t_p$$

Similarly, for Term II:

$$II = \left[ k_N \frac{T_{i,j+1,p} - T_{i,j,p}}{\Delta y_N} - k_S \frac{T_{i,j,p} - T_{i,j-1,p}}{\Delta y_S} \right] \Delta x_{i,j} \Delta t_p$$

Term III:

$$III = [(Sc_{i,j} - Sp_{i,j} T_{i,j,p}) \Delta x_{i,j} \Delta y_{i,j} \Delta t_p]$$

Term IV:

$$IV = [rCp(T_{i,j,p} - T_{i,j,p-1}) \Delta x_{i,j} \Delta y_{i,j}]$$

**General Interior Node:**

$$\left[ k_E \left( \frac{T_{i+1,j,p} - T_{i,j,p}}{\Delta x_E} \right) - k_W \left( \frac{T_{i,j,p} - T_{i-1,j,p}}{\Delta x_W} \right) \right] \Delta y_{i,j} \Delta t_p + \left[ k_N \left( \frac{T_{i,j+1,p} - T_{i,j,p}}{\Delta y_N} \right) - k_S \left( \frac{T_{i,j,p} - T_{i,j-1,p}}{\Delta y_S} \right) \right] \Delta x_{i,j} \Delta t_p + [(Sc_{i,j} - Sp_{i,j} T_{i,j,p}) \Delta x_{i,j} \Delta y_{i,j} \Delta t_p] - [rCp(T_{i,j,p} - T_{i,j,p-1}) \Delta x_{i,j} \Delta y_{i,j}] = 0$$

**Expand:**

$$\begin{aligned} & \left[ \left( \frac{k_E T_{i+1,j,p} \Delta y_{i,j} \Delta t_p - k_E T_{i,j,p} \Delta y_{i,j} \Delta t_p}{\Delta x_E} \right) - \left( \frac{k_W T_{i,j,p} \Delta y_{i,j} \Delta t_p - k_W T_{i-1,j,p} \Delta y_{i,j} \Delta t_p}{\Delta x_W} \right) \right] \\ & + \left[ \left( \frac{k_N T_{i,j+1,p} \Delta x_{i,j} \Delta t_p - k_N T_{i,j,p} \Delta x_{i,j} \Delta t_p}{\Delta y_N} \right) - \left( \frac{k_S T_{i,j,p} \Delta x_{i,j} \Delta t_p - k_S T_{i,j-1,p} \Delta x_{i,j} \Delta t_p}{\Delta y_S} \right) \right] + \\ & \left[ (Sc_{i,j} \Delta x_{i,j} \Delta y_{i,j} - Sp_{i,j} T_{i,j,p} \Delta x_{i,j} \Delta y_{i,j}) \Delta t_p \right] - \left[ (rCp T_{i,j,p} \Delta x_{i,j} \Delta y_{i,j} - rCp T_{i,j,p-1} \Delta x_{i,j} \Delta y_{i,j}) \right] = 0 \end{aligned}$$

**Divide by  $\Delta t_p$  and Expand:**

$$\begin{aligned} & \left[ \left( \frac{k_E T_{i+1,j,p} \Delta y_{i,j} - k_E T_{i,j,p} \Delta y_{i,j}}{\Delta x_E} \right) - \left( \frac{k_W T_{i,j,p} \Delta y_{i,j} - k_W T_{i-1,j,p} \Delta y_{i,j}}{\Delta x_W} \right) \right] \\ & + \left[ \left( \frac{k_N T_{i,j+1,p} \Delta x_{i,j} - k_N T_{i,j,p} \Delta x_{i,j}}{\Delta y_N} \right) - \left( \frac{k_S T_{i,j,p} \Delta x_{i,j} - k_S T_{i,j-1,p} \Delta x_{i,j}}{\Delta y_S} \right) \right] + \\ & \left[ (Sc_{i,j} \Delta x_{i,j} \Delta y_{i,j} - Sp_{i,j} T_{i,j,p} \Delta x_{i,j} \Delta y_{i,j}) \right] - \left[ \left( \frac{rCp}{\Delta t_p} T_{i,j,p} \Delta x_{i,j} \Delta y_{i,j} - \frac{rCp}{\Delta t_p} T_{i,j,p-1} \Delta x_{i,j} \Delta y_{i,j} \right) \right] = 0 \end{aligned}$$

$$\begin{aligned} & \left( \frac{k_E T_{i+1,j,p} \Delta y_{i,j} - k_E T_{i,j,p} \Delta y_{i,j}}{\Delta x_E} \right) - \left( \frac{k_W T_{i,j,p} \Delta y_{i,j} - k_W T_{i-1,j,p} \Delta y_{i,j}}{\Delta x_W} \right) \\ & + \left( \frac{k_N T_{i,j+1,p} \Delta x_{i,j} - k_N T_{i,j,p} \Delta x_{i,j}}{\Delta y_N} \right) - \left( \frac{k_S T_{i,j,p} \Delta x_{i,j} - k_S T_{i,j-1,p} \Delta x_{i,j}}{\Delta y_S} \right) + \\ & \left[ (Sc_{i,j} \Delta x_{i,j} \Delta y_{i,j} - Sp_{i,j} T_{i,j,p} \Delta x_{i,j} \Delta y_{i,j}) \right] - \left( \frac{rCp}{\Delta t_p} T_{i,j,p} \Delta x_{i,j} \Delta y_{i,j} - \frac{rCp}{\Delta t_p} T_{i,j,p-1} \Delta x_{i,j} \Delta y_{i,j} \right) = 0 \end{aligned}$$

$$\begin{aligned}
& \frac{k_E \Delta y_{i,j}}{\Delta x_E} T_{i+1,j,p} - \frac{k_E \Delta y_{i,j}}{\Delta x_E} T_{i,j,p} - \frac{k_W \Delta y_{i,j}}{\Delta x_W} T_{i,j,p} + \frac{k_W \Delta y_{i,j}}{\Delta x_W} T_{i-1,j,p} + \frac{k_N \Delta x_{i,j}}{\Delta y_N} T_{i,j+1,p} - \frac{k_N \Delta x_{i,j}}{\Delta y_N} T_{i,j,p} \\
& - \frac{k_S \Delta x_{i,j}}{\Delta y_S} T_{i,j,p} + \frac{k_S \Delta x_{i,j}}{\Delta y_S} T_{i,j-1,p} + Sc_{i,j} \Delta x_{i,j} \Delta y_{i,j} - Sp_{i,j} T_{i,j,p} \Delta x_{i,j} \Delta y_{i,j} - \frac{rCp}{\Delta t_p} T_{i,j,p} \Delta x_{i,j} \Delta y_{i,j} \\
& + \frac{rCp}{\Delta t_p} T_{i,j,p-1} \Delta x_{i,j} \Delta y_{i,j} = 0
\end{aligned}$$

**Assign Coefficients:**

$$\begin{aligned}
& \underbrace{\frac{k_E \Delta y_{i,j}}{\Delta x_E} T_{i+1,j,p}}_{aE_{i,j}} - \underbrace{\frac{k_E \Delta y_{i,j}}{\Delta x_E} T_{i,j,p}}_{aE_{i,j}} - \underbrace{\frac{k_W \Delta y_{i,j}}{\Delta x_W} T_{i,j,p}}_{aW_{i,j}} + \underbrace{\frac{k_W \Delta y_{i,j}}{\Delta x_W} T_{i-1,j,p}}_{aW_{i,j}} + \underbrace{\frac{k_N \Delta x_{i,j}}{\Delta y_N} T_{i,j+1,p}}_{aN_{i,j}} - \underbrace{\frac{k_N \Delta x_{i,j}}{\Delta y_N} T_{i,j,p}}_{aN_{i,j}} \\
& - \underbrace{\frac{k_S \Delta x_{i,j}}{\Delta y_S} T_{i,j,p}}_{aS_{i,j}} + \underbrace{\frac{k_S \Delta x_{i,j}}{\Delta y_S} T_{i,j-1,p}}_{aS_{i,j}} + Sc_{i,j} \Delta x_{i,j} \Delta y_{i,j} - Sp_{i,j} T_{i,j,p} \Delta x_{i,j} \Delta y_{i,j} - \underbrace{\frac{rCp}{\Delta t_p} \Delta x_{i,j} \Delta y_{i,j} T_{i,j,p}}_{aO_{i,j}} \\
& + \underbrace{\frac{rCp}{\Delta t_p} \Delta x_{i,j} \Delta y_{i,j} T_{i,j,p-1}}_{aO_{i,j}} = 0
\end{aligned}$$

**Collect and Simplify:**

$$\begin{aligned}
& aE_{i,j} T_{i+1,j,p} - aE_{i,j} T_{i,j,p} - aW_{i,j} T_{i,j,p} + aW_{i,j} T_{i-1,j,p} + aN_{i,j} T_{i,j+1,p} - aN_{i,j} T_{i,j,p} - aS_{i,j} T_{i,j,p} + aS_{i,j} T_{i,j-1,p} \\
& + Sc_{i,j} \Delta x_{i,j} \Delta y_{i,j} - Sp_{i,j} T_{i,j,p} \Delta x_{i,j} \Delta y_{i,j} - aO_{i,j} T_{i,j,p} + aO_{i,j} T_{i,j,p-1} = 0
\end{aligned}$$

$$\begin{aligned}
& - \underbrace{(aO_{i,j} + aE_{i,j} + aW_{i,j} + aN_{i,j} + aS_{i,j} + Sp_{i,j} \Delta x_{i,j} \Delta y_{i,j})}_{a_{i,j}} T_{i,j,p} + aE_{i,j} T_{i+1,j,p} + aW_{i,j} T_{i-1,j,p} + aN_{i,j} T_{i,j+1,p} \\
& + aS_{i,j} T_{i,j-1,p} + Sc_{i,j} \Delta x_{i,j} \Delta y_{i,j} + aO_{i,j} T_{i,j,p-1} = 0
\end{aligned}$$

$$- a_{i,j} T_{i,j,p} + aE_{i,j} T_{i+1,j,p} + aW_{i,j} T_{i-1,j,p} + aN_{i,j} T_{i,j+1,p} + aS_{i,j} T_{i,j-1,p} + Sc_{i,j} \Delta x_{i,j} \Delta y_{i,j} + aO_{i,j} T_{i,j,p-1} = 0$$

**Separate and Simplify:**

$$a_{i,j}T_{i,j,p} - aE_{i,j}T_{i+1,j,p} - aW_{i,j}T_{i-1,j,p} - aN_{i,j}T_{i,j+1,p} - aS_{i,j}T_{i,j-1,p} = \underbrace{Sc_{i,j}\Delta x_{i,j}\Delta y_{i,j} + aO_{i,j}T_{i,j,p-1}}_{b_{i,j}}$$

**General 2D Transient Discretization Equation:**

$$a_{i,j}T_{i,j,p} - aE_{i,j}T_{i+1,j,p} - aW_{i,j}T_{i-1,j,p} - aN_{i,j}T_{i,j+1,p} - aS_{i,j}T_{i,j-1,p} = b_{i,j}$$

**where:**

$$aE_{i,j} = \frac{k_E \Delta y_{i,j}}{\Delta x_E}$$

$$aW_{i,j} = \frac{k_W \Delta y_{i,j}}{\Delta x_W}$$

$$aN_{i,j} = \frac{k_N \Delta x_{i,j}}{\Delta y_N}$$

$$aS_{i,j} = \frac{k_S \Delta x_{i,j}}{\Delta y_S}$$

$$aO_{i,j} = \frac{rCp}{\Delta t_p} \Delta x_{i,j} \Delta y_{i,j}$$

$$b_{i,j} = Sc_{i,j} \Delta x_{i,j} \Delta y_{i,j} + aO_{i,j} T_{i,j,p-1}$$

$$a_{i,j} = aO_{i,j} + aE_{i,j} + aW_{i,j} + aN_{i,j} + aS_{i,j} + Sp_{i,j} \Delta x_{i,j} \Delta y_{i,j}$$

### Nodal Spacing:

$$\Delta x_E = \frac{\Delta x_{i,j}}{2} + \frac{\Delta x_{i+1,j}}{2} \quad \Delta x_W = \frac{\Delta x_{i,j}}{2} + \frac{\Delta x_{i-1,j}}{2}$$

$$\Delta y_N = \frac{\Delta y_{i,j}}{2} + \frac{\Delta y_{i,j+1}}{2} \quad \Delta y_S = \frac{\Delta y_{i,j}}{2} + \frac{\Delta y_{i,j-1}}{2}$$

### Interface Conductivities:

$$k_E = \frac{2k_{i,j}k_{i+1,j}}{\left(k_{i+1,j} \frac{\Delta x_{i,j}}{\Delta x_E}\right) + \left(k_{i,j} \frac{\Delta x_{i+1,j}}{\Delta x_E}\right)} \quad k_W = \frac{2k_{i,j}k_{i-1,j}}{\left(k_{i-1,j} \frac{\Delta x_{i,j}}{\Delta x_W}\right) + \left(k_{i,j} \frac{\Delta x_{i-1,j}}{\Delta x_W}\right)}$$

$$k_N = \frac{2k_{i,j}k_{i,j+1}}{\left(k_{i,j+1} \frac{\Delta y_{i,j}}{\Delta y_N}\right) + \left(k_{i,j} \frac{\Delta y_{i,j+1}}{\Delta y_N}\right)} \quad k_S = \frac{2k_{i,j}k_{i,j-1}}{\left(k_{i,j-1} \frac{\Delta y_{i,j}}{\Delta y_S}\right) + \left(k_{i,j} \frac{\Delta y_{i,j-1}}{\Delta y_S}\right)}$$

### Substitute Nodal Spacing into Conductivities...

$$k_E = \frac{2k_{i,j}k_{i+1,j}}{\left(k_{i+1,j} \frac{\Delta x_{i,j}}{\frac{\Delta x_{i,j}}{2} + \frac{\Delta x_{i+1,j}}{2}}\right) + \left(k_{i,j} \frac{\Delta x_{i+1,j}}{\frac{\Delta x_{i,j}}{2} + \frac{\Delta x_{i+1,j}}{2}}\right)}$$

$$k_E = \frac{2k_{i,j}k_{i+1,j}}{\left(\frac{2k_{i+1,j}\Delta x_{i,j}}{\Delta x_{i,j} + \Delta x_{i+1,j}}\right) + \left(\frac{2k_{i,j}\Delta x_{i+1,j}}{\Delta x_{i,j} + \Delta x_{i+1,j}}\right)}$$

$$k_E = \frac{2k_{i,j}k_{i+1,j}}{\left(\frac{2k_{i+1,j}\Delta x_{i,j} + 2k_{i,j}\Delta x_{i+1,j}}{\Delta x_{i,j} + \Delta x_{i+1,j}}\right)}$$

### Simplified Interface Conductivity:

#### East Face:

$$k_E = \frac{k_{i,j}k_{i+1,j}(\Delta x_{i,j} + \Delta x_{i+1,j})}{k_{i+1,j}\Delta x_{i,j} + k_{i,j}\Delta x_{i+1,j}}$$

#### West Face:

$$k_W = \frac{k_{i,j}k_{i-1,j}(\Delta x_{i,j} + \Delta x_{i-1,j})}{k_{i-1,j}\Delta x_{i,j} + k_{i,j}\Delta x_{i-1,j}}$$

#### North Face:

$$k_N = \frac{k_{i,j}k_{i,j+1}(\Delta y_{i,j} + \Delta y_{i,j+1})}{k_{i,j+1}\Delta y_{i,j} + k_{i,j}\Delta y_{i,j+1}}$$

#### South Face:

$$k_S = \frac{k_{i,j}k_{i,j-1}(\Delta y_{i,j} + \Delta y_{i,j-1})}{k_{i,j-1}\Delta y_{i,j} + k_{i,j}\Delta y_{i,j-1}}$$

## **Appendix F**

### **Table of Discretized Boundary Conditions**

The following table presents the relevant discretization coefficients resulting from various boundary conditions.

# Table F1: Boundary Condition Cases

(adapted from Vick, 2000)

Boundary @  $x = 0$

BCx0	Boundary Inputs	$aE_{1,j}$	$a_{1,j}$	$b_{1,j}$
1	$Tx_{0j}$	0	1	$Tx_{0j}$
2	$qx_{0j}$	$\frac{k_{2,j}}{\Delta x_2 / 2}$	$aE_{1,j}$	$qx_{0j}$
3	$T^\infty x_{0j}, hx_{0j}$	$\frac{k_{2,j}}{\Delta x_2 / 2}$	$aE_{1,j} + hx_{0j}$	$hx_{0j} \bullet T^\infty x_{0j}$

Boundary @  $x = L$

BCxL	Boundary Inputs	$aW_{L,j}$	$a_{L,j}$	$b_{L,j}$
1	$Tx_{Lj}$	0	1	$Tx_{Lj}$
2	$qx_{Lj}$	$\frac{k_{iLast1,j}}{\Delta x_{iLast1} / 2}$	$aW_{L,j}$	$qx_{Lj}$
3	$T^\infty x_{Lj}, hx_{Lj}$	$\frac{k_{iLast1,j}}{\Delta x_{iLast1} / 2}$	$aW_{L,j} + hx_{Lj}$	$hx_{Lj} \bullet T^\infty x_{Lj}$

**Table F1: Boundary Condition Cases (cont'd)**

Boundary @  $y = 0$

BC <sub>y0</sub>	Boundary Inputs	$a_{N_{i,1}}$	$a_{i,1}$	$b_{i,1}$
1	$Ty_{0i}$	0	1	$Ty_{0i}$
2	$qy_{0i}$	$\frac{k_{i,2}}{\Delta y_2 / 2}$	$a_{N_{i,0}}$	$qy_{0i}$
3	$T^\infty y_{0i}, hy_{0i}$	$\frac{k_{i,2}}{\Delta y_2 / 2}$	$a_{N_{i,0}+ hy_{0i}}$	$hy_{0i} \bullet T^\infty y_{0i}$

Boundary @  $y = L$

BC <sub>yL</sub>	Boundary Inputs	$a_{S_{i,L}}$	$a_{i,L}$	$b_{i,L}$
1	$Ty_{Li}$	0	1	$Ty_{Li}$
2	$qy_{Li}$	$\frac{k_{i,jLast1}}{\Delta y_{jLast1} / 2}$	$a_{S_{i,L}}$	$qy_{Li}$
3	$T^\infty y_{Li}, hy_{Li}$	$\frac{k_{i,jlast1}}{\Delta y_{jlast1} / 2}$	$a_{N_{i,jlast1}+ hy_{Li}}$	$hy_{Li} \bullet T^\infty y_{Li}$

# **Appendix G**

## **Derivation of the Stability Criteria**

This appendix details the derivation of the stability criteria used in the foregoing numerical solution.

# Derivation of the Stability Criteria

Beginning with Figure 5.7:

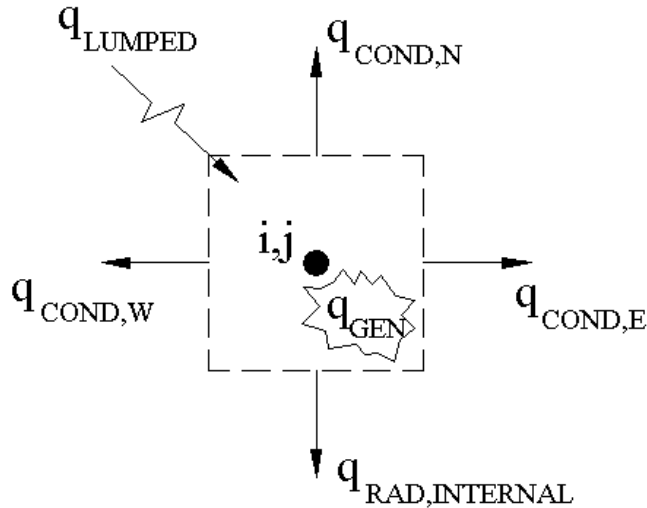


Figure G5.7 Schematic of Internal Radiation Node

Performing an energy balance on the control volume surrounding the node:

$$\dot{E}_{IN} - \dot{E}_{OUT} + \dot{E}_{GEN} = \frac{dE_{ST}}{dt}$$

Substituting appropriate quantities and defining  $q_{cond}$  (note the substitution of  $q_{IN}$ ):

$$q_{cond} = q_{cond,E} + q_{cond,W} + q_{cond,N}$$

$$q_{in} + q_{gen} - q_{rad} - q_{cond} = \mathbf{r}V C_p \frac{dT}{dt}$$

Defining  $C_1$ :

$$C_1 = \mathbf{r}V C_p$$

$$q_{in} + q_{gen} - q_{rad} - q_{cond} = C_1 \frac{dT}{dt}$$

From previous derivations:

$$q_{in} = \frac{\left[ \frac{q_{ELEC,SIDES} + \frac{T_{\infty}}{R_{OUT}} + \frac{T}{R_{IN}}}{\left( \frac{1}{R_{IN}} + \frac{1}{R_{OUT}} \right)} \right] - T}{R_{IN}} \quad [4.9]$$

$$q_{rad, internal} \Big|_{\substack{\text{EMISSIVE} \\ \text{SURFACE}}} = \epsilon A (T_1^4 - T_2^4) = q_{rad} \quad [4.7]$$

$$q_{gen} = p = Ri^2 \quad [2.9]$$

$$q_{cond} = \frac{kA}{L} (T_1 - T_2) \quad \text{From discretization of [2.2]}$$

And for the transient part:

$$C_1 \frac{dT}{dt} = \frac{C_1 (T_p - T_{p-1})}{\Delta t}$$

Utilize the discretized forms of  $q_{cond,E}$ ,  $q_{cond,W}$ , and  $q_{cond,N}$ :

$$q_{cond,E} = \frac{k_E \Delta y \Delta z}{\Delta x_E} (T_{p-1} - T_E)$$

$$q_{cond,W} = \frac{k_W \Delta y \Delta z}{\Delta x_W} (T_{p-1} - T_W)$$

$$q_{cond,N} = \frac{k_N \Delta x \Delta z}{\Delta y_N} (T_{p-1} - T_N)$$

Manipulating  $q_{in}$ :

$$q_{in} = \frac{q_{ELEC,SIDES} R_{OUT} + T_{\infty}}{R_{IN} + R_{OUT}} - \frac{1}{R_{IN} + R_{OUT}} T_{p-1}$$

Substitution yields:

$$\frac{q_{ELEC,SIDES} R_{OUT} + T_{\infty}}{R_{IN} + R_{OUT}} - \frac{1}{R_{IN} + R_{OUT}} T_{p-1} + q_{gen} - q_{rad} - \frac{k_E \Delta y \Delta z}{\Delta x_E} (T_{p-1} - T_E) -$$

$$\frac{k_W \Delta y \Delta z}{\Delta x_W} (T_{p-1} - T_W) - \frac{k_N \Delta x \Delta z}{\Delta y_N} (T_{p-1} - T_N) = \frac{C_1 (T_p - T_{p-1})}{\Delta t}$$

Defining  $K_E$ ,  $K_W$ , and  $K_N$ :

$$K_E = \frac{k_E \Delta y \Delta z}{\Delta x_E}$$

$$K_W = \frac{k_W \Delta y \Delta z}{\Delta x_W}$$

$$K_N = \frac{k_N \Delta x \Delta z}{\Delta y_N}$$

Letting:

$$K_{lumped} = \frac{q_{ELEC,SIDES} R_{OUT} + T_{\infty}}{R_{IN} + R_{OUT}}$$

Applying the guesses from the previous iteration, obtain:

$$K_{lumped} - \frac{1}{R_{IN} + R_{OUT}} T_{p-1} + q_{gen} - \mathbf{sA} (T_{p-1}^4 - T_{2,p-1}^4) - K_E (T_{p-1} - T_E) -$$

$$K_W (T_{p-1} - T_W) - K_N (T_{p-1} - T_N) = \frac{C_1 (T_p - T_{p-1})}{\Delta t}$$

Factoring the radiation term:

$$(T_{p-1}^4 - T_{2,p-1}^4) = (T_{p-1} - T_{2,p-1}) (T_{p-1} + T_{2,p-1}) (T_{p-1}^2 - T_{2,p-1}^2)$$

Substituting:

$$K_{lumped} - \frac{1}{R_{IN} + R_{OUT}} T_{p-1} + q_{gen} - \mathbf{sA} (T_{p-1} - T_{2,p-1}) (T_{p-1} + T_{2,p-1}) (T_{p-1}^2 - T_{2,p-1}^2)$$

$$- K_E (T_{p-1} - T_E) - K_W (T_{p-1} - T_W) - K_N (T_{p-1} - T_N) = \frac{C_1 (T_p - T_{p-1})}{\Delta t}$$

Performing copious algebra and grouping terms:

$$T_p = \frac{\Delta t}{C_1} [K_{lumped} + q_{gen} + K_E T_E + K_W T_W + K_N T_N + \mathbf{se}_1 A_1 T_{2,p-1}^4] +$$

$$T_{p-1} \left[ 1 - \frac{\Delta t}{C_1} \left( \frac{1}{R_{IN} + R_{OUT}} + \mathbf{sAT}_{p-1}^3 + K_E + K_W + K_N \right) \right]$$

Noting that the coefficient acting on  $T_{p-1}$  must be positive, the stability criteria is obtained:

$$\Delta t < \frac{C_1}{\left( \frac{1}{R_{in} + R_{out}} \right) + \mathbf{sAT}_{i,j,p-1}^3 + K_E + K_W + K_N} \quad [5.17]$$

where  $\Delta t$  is the stable time-step,  $C_1 = \mathbf{r}_{i,j} V_{i,j} Cp_{i,j}$ , and  $K_E = \frac{k_E \Delta y_{i,j}}{\Delta x_E}$ ;  $K_W$  and  $K_N$  are similarly formulated.

# Appendix H

## Mathematica<sup>®</sup> Code

This appendix contains the Mathematica<sup>®</sup> code used in the foregoing numerical solution.

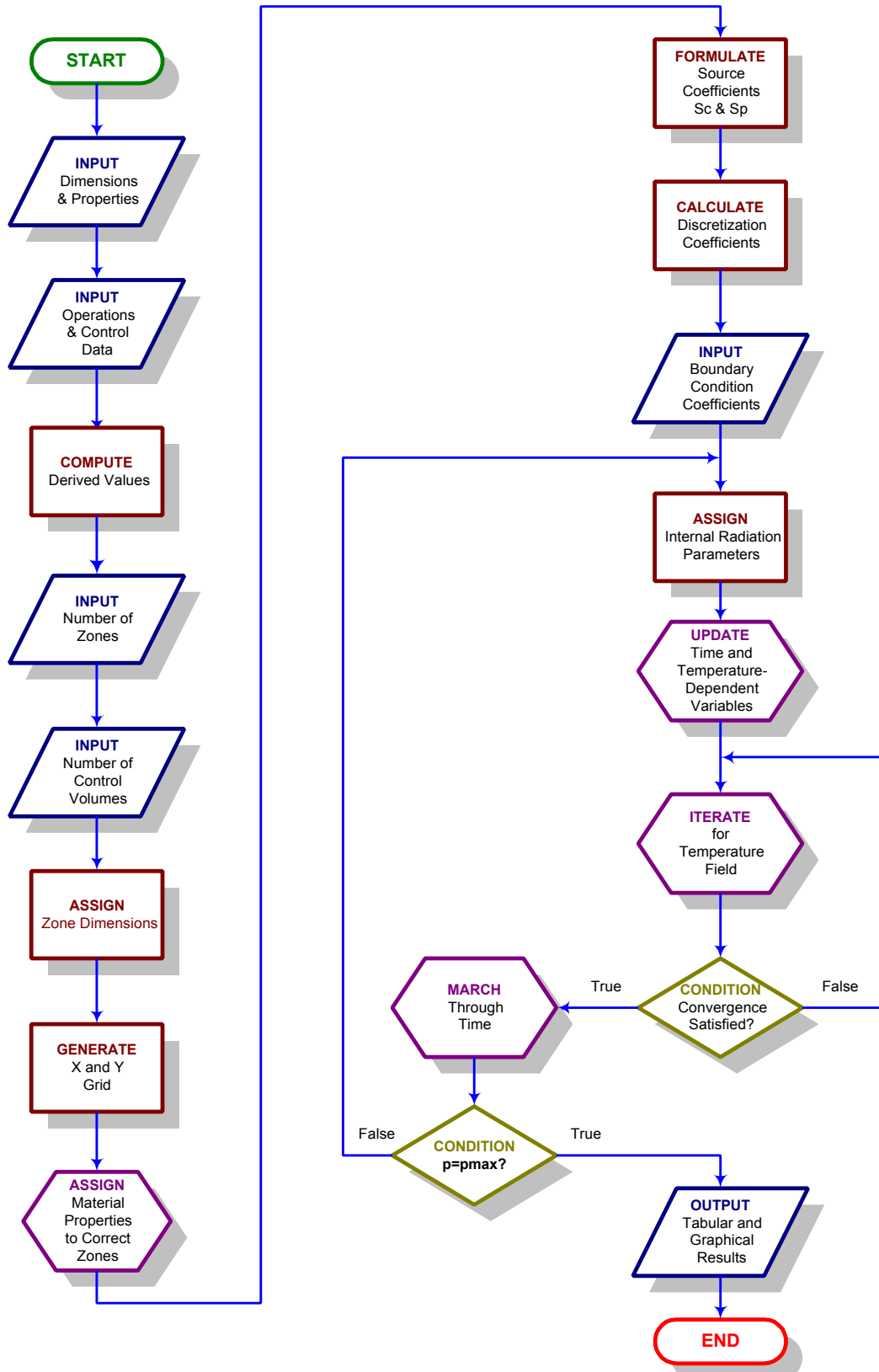


Figure H5.8 Simplified Flow Chart of Numerical Solution

# Thermal Analysis of a Vaporization Source for Inorganic Coatings

## An Application of the Finite Difference Method In Two Dimensions

*Research Model 10-0*

---

Non-uniform, zoned grid; non-uniform, temperature-  
dependent properties; and radiative, convective,  
conductive, and evaporative transfer

by

Brian V. Nutter

*Note to User*

*The input data and constants contained herein have been altered to protect the proprietary interests of this project. Please forgive any inconvenience.*

# Program Initialization

## Clear All

```
Clear[NCVX, NCVY, a, aE, aW, aN, aS, aO, b, Sc, Sp, XKnown, YKnown,
XDiagonal, XSubDiag, XSuperDiag, YDiagonal, YSubDiag, YSuperDiag,
TempvectorX, TempvectorY, T, Tlast, Tprev, change, delta,
difference, transience, Temperature, t, Δt, i, j, p, k, Cp, ρ,
ΔxZone, ΔyZone, start, stop, Zone, ktime, Cptime, ρtime, MinTemp,
MaxTemp, step, HuntDown, EvaporantPresent, MassTransferLoss,
BoundarySources, InternalSourcesSc, InternalSourcesSp,
GlobalΔEnergyStorage, MeanEvapTemp, LowerSourceVolume,
UpperLowerSourceVolume, LumpedLowerSourceVolume,
UpperConvectionVolume, LowerConvectionVolume, Speleclumped,
qelecLdistSS, LumpedConstantConvectionOnly, Spconvlower,
Scconvupper, Spconvupper, Tmass, LowerEvaporantSurface,
UpperEvaporantSurface, UpperRadiantSurface, LowerRadiantSurface,
VesselAbsorptiveSurface, VesselLateralBoundary, InternalRadiation,
plast, EvaporationTime, Sczone, Spzone, qelecH, qelecL, Δtnew,
TimeStretch, ComputationTime, StartTime, TimeStorage, Δtime];

Clear[R1, R2, ΔxE, ΔxW, ΔyN, Capacity, Tstability, ConductanceE,
ConductanceW, ConductanceN, TimeStepMax, Tcriteria];
```

## Initialize Timer

```
StartTime = TimeUsed[];
```

---

## Load Mathematica Packages

```
<< LinearAlgebra`Tridiagonal`
```

```
<< Calculus`DiracDelta`
```

```
<< Graphics`Graphics3D`
```

```
<< Graphics`Animation`
```

```
<< Graphics`MultipleListPlot`
```

```
SetOptions[ListPlot,  
  PlotJoined → True,  
  PlotRange → All,  
  PlotStyle → {Thickness[0.007], Hue[1]},  
  Frame → True,  
  GridLines → Automatic,  
  ImageSize -> {300, 210},  
  Background → GrayLevel[1]  
];
```

```
SetOptions[MultipleListPlot,  
  PlotJoined → True,  
  PlotRange → All,  
  PlotStyle → {Thickness[.002], Hue[1]},  
  Frame → True,  
  GridLines → Automatic,  
  ImageSize -> {300, 210},  
  Background → GrayLevel[1]  
];
```

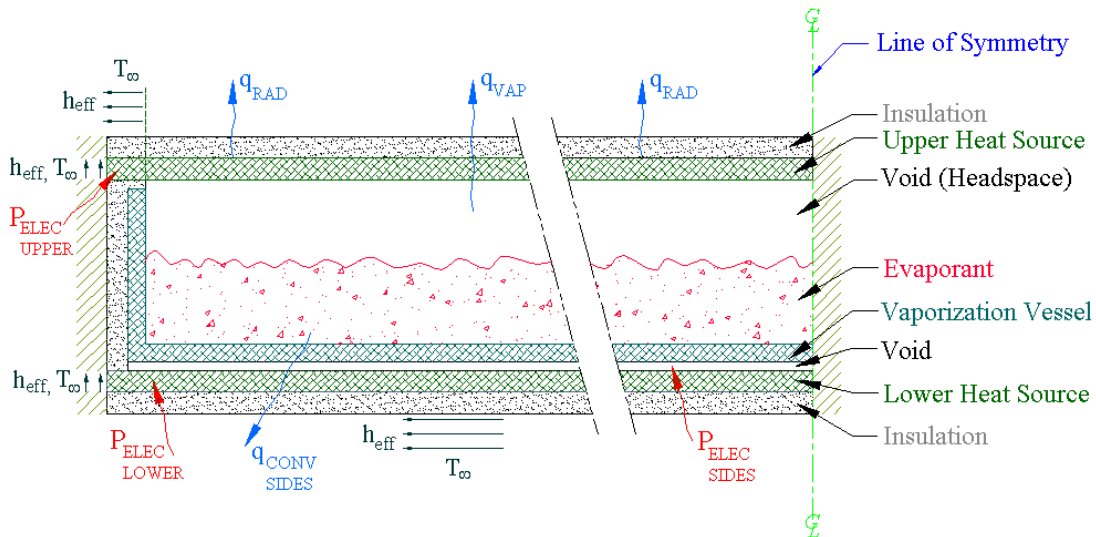
# User Input-Model Setup

## Set File Output Directory

```
SetDirectory["D:\MSME Models\Mathematica Output\OutputDir"]
```

## Geometry Data

## Model Schematic



---

## Enter Model Physical Dimensions (Using Schematic as a Reference)

```
WaterJacketInsulThk = .1 ;
LowerSourceThickness = .1 ;
LowerSourceVesselInsulThk = .1 ;
VesselBottThk = .1 ;
EvaporantDepth = 1. ;
VesselHeadspace = 1.2 ;
VesselUpperSourceInsulThk = .1 ;
UpperSourceThickness = .1 ;
UpperSourceInsulThk = .3 ;
VesselEndThk = .1 ;
VesselEndInsulThk = .1 ;
Zone3Width = 1. ;
Zone4Width = 1. ;
Zone5Width = 1. ;
Zone6Width = 1. ;
Zone7Width = 1. ;
Zone8Width = 1. ;
Zone9Width = 1. ;
Zone10Width = 1. ;
Zone11Width = 1. ;
Zone12Width = 1. ;
```

---

## Thermal Data

---

### Physical Properties of Model Materials

#### ▼ Temperature Limit of Property Functions

```
PropertyLimit = 2400 ;
```

## ▼ Conductivity

```
LowerSourcek[T_] := (-3.0 * 10-11 * T4) + (2.0 * 10-7 * T3) -  
  (0.0005 * T2) + (0.4713 * T) + 94.777; (* W/(m K) *)  
Vesselk[T_] := (-3.0 * 10-11 * T4) + (2.0 * 10-7 * T3) -  
  (0.0005 * T2) + (0.4713 * T) + 94.777; (* W/(m K) *)  
UpperSourcek[T_] := (-3.0 * 10-11 * T4) + (2.0 * 10-7 * T3) -  
  (0.0005 * T2) + (0.4713 * T) + 94.777; (* W/(m K) *)  
Insulationk[T_] :=  
  0.0196348435582817959` + 0.000129263803680981915` T; (* W/(m K) *)  
Evaporantk[T_] :=  
  Which[0 < T < TmaxEvap, 1.380 + (0.0 * T), True, 10-100];  
Voidk[T_] := 10-100;
```

## ▼ Specific Heat

```
LowerSourceCp[T_] := (-3 * 10-10 * T4) + (2 * 10-6 * T3) -  
  (0.0049 * T2) + (5.5271 * T) - 560.88; (* J/(kg K) *)  
VesselCp[T_] :=  
  (-3 * 10-10 * T4) + (2 * 10-6 * T3) - (0.0049 * T2) + (5.5271 * T) - 560.88;  
UpperSourceCp[T_] :=  
  (-3 * 10-10 * T4) + (2 * 10-6 * T3) - (0.0049 * T2) + (5.5271 * T) - 560.88;  
InsulationCp[T_] := (3 * 10-7 * T3) - (0.001 * T2) + (1.6001 * T) + 398.64;  
EvaporantCp[T_] :=  
  Which[0 < T < 580, 37.556, 580 <= T < TmaxEvap, -1.2 * 10-5 * T3 +  
    0.03144456 * T2 - 21.802373 * T + 4417.5691, True, 0 * T];  
VoidCp[T_] := (0 * T);
```

## ▼ Density

```
LowerSourceρ[T_] := 1790 (* kg/m3 *);  
Vesselρ[T_] := 1790;  
UpperSourceρ[T_] := 1790;  
Insulationρ[T_] := 480;  
Evaporantρ[T_] := Which[0 < T < TmaxEvap, 1025, True, 0 * T];  
Voidρ[T_] := (0 * T);
```

## ▼ Vaporization Cessation Temperature

```
TmaxEvap = 1573;
```

# Physical System Operations Data

## ▼ Water Cooling Data from Physical System

▽ Bulk mean temperature of cooling water

```
Tmean = 292.87; (* 292.87 K or 19.7 C° *)
```

▽ Convection coefficient

```
heffective = 1900; (*  $\frac{W}{m^2 K}$  *)
```

## ▼ Vaporization Data

▽ Operation Setpoint

```
TempSetpoint = 1373.15 (* K *)
```

▽ Mean Evaporant Temperature

```
MeanEvapTemp :=  
Sum[Ti, UpperEvaporantSurface, p, {i, VesselLateralBoundary + 1, i2}] /  
(i2 - VesselLateralBoundary);
```

## ▼ Radiation Data

▽ Enclosure Temperature

```
Tsurr = 298.15 (* 25 °C *)
```

▽ Linearized Radiation Coefficient

```
hradiation[T_] :=  $\epsilon_{ext} * \sigma * (T + Tsurr) * (T^2 + Tsurr^2)$ ;
```

▽ Internal View Factor Between Control Volume Faces

```
 $\sigma = 5.67 * 10^{-8}$  (* Stefan-Boltzmann Constant  $\frac{W}{m^2 K^4}$  *) ;  
F = 1 ;
```

▽ External Emissivity

```
 $\epsilon_{ext} = 0.95$ ;
```

## ▼ Internal Radiation

### ▽ Search Routine to Locate Evaporant Level

```
HuntDown := Module[{},
  step = 0;
  While [UpperEvaporantSurface - step >= LowerEvaporantSurface &&
    EvaporantPresenti,UpperEvaporantSurface-step != 1, step++];
  step];
```

### ▽ Internal Radiation Coefficients

```
InternalRadiation := Module[{},
  Do [
    SCi,LowerRadiantSurface = SCi,LowerRadiantSurface -  $\left( \frac{\sigma F}{\Delta Y_{\text{LowerRadiantSurface}}} \right)$ 
      (Ti,LowerRadiantSurface,p4 - Ti,VesselAbsorptiveSurface,p4);

    SCi,VesselAbsorptiveSurface =
    SCi,VesselAbsorptiveSurface +  $\left( \frac{\sigma F}{\Delta Y_{\text{VesselAbsorptiveSurface}}} \right)$ 
      (Ti,LowerRadiantSurface,p4 - Ti,VesselAbsorptiveSurface,p4);

    SCi,UpperRadiantSurface = SCi,UpperRadiantSurface -  $\left( \frac{\sigma F}{\Delta Y_{\text{UpperRadiantSurface}}} \right)$ 
      (Ti,UpperRadiantSurface,p4 - Ti,UpperEvaporantSurface-HuntDown,p4);

    SCi,UpperEvaporantSurface-HuntDown =
    SCi,UpperEvaporantSurface-HuntDown +  $\left( \frac{\sigma F}{\Delta Y_{\text{UpperEvaporantSurface-HuntDown}}} \right)$ 
      (Ti,UpperRadiantSurface,p4 - Ti,UpperEvaporantSurface-HuntDown,p4);

    , {i, VesselLateralBoundary + 1, ilast1}];
  ];
```

## ▼ Thermal Resistances

```
Rvessel := (VesselEndThk * 0.0254 / (Vesselk[Ti,j,p] * Δxi * Δyj));
Rinsulation := (VesselUpperSourceInsulThk *
  0.0254 / (Insulationk[Ti,j,p] * Δxi * Δyj));
Rconv := (1 / (heffective * Δxi * Δyj));
RconvUpper := (1 / (2 * heffective * Δxi * Δyj));

Rout := Rinsulation + Rconv;
RoutUpper := Rinsulation + RconvUpper;
Rin := Rvessel;
```

## ▼ Power Input Functions

### ▽ Upper Source Transient Step Data

```
NumberTimeStepsUpper = 13;  
Uppert1 = 0; UpperInput1 = 11987 / 2;  
Uppert2 = 300; UpperInput2 = 10713 / 2;  
Uppert3 = 940; UpperInput3 = 2162 / 2;  
Uppert4 = 1680; UpperInput4 = 13567 / 2;  
Uppert5 = 2400; UpperInput5 = 12205 / 2;  
Uppert6 = 2760; UpperInput6 = -50634 / 2;  
Uppert7 = 3200; UpperInput7 = 39386 / 2;  
Uppert8 = 3480; UpperInput8 = -833 / 2;  
Uppert9 = 3800; UpperInput9 = 5365 / 2;  
Uppert10 = 4340; UpperInput10 = -3476 / 2;  
Uppert11 = 4660; UpperInput11 = 3513 / 2;  
Uppert12 = 4840; UpperInput12 = -5781 / 2;  
Uppert13 = 5400; UpperInput13 = 5428 / 2;
```

### ▽ Lower Source Transient Step Data

```
NumberTimeStepsLower = 10;  
Lowert1 = 0; LowerInput1 = 9963 / 2;  
Lowert2 = 940; LowerInput2 = 4603 / 2;  
Lowert3 = 1680; LowerInput3 = 1622 / 2;  
Lowert4 = 2500; LowerInput4 = -13484 / 2;  
Lowert5 = 3200; LowerInput5 = 5316 / 2;  
Lowert6 = 4280; LowerInput6 = -1592;  
Lowert7 = 480; LowerInput7 = -2722 / 2;  
Lowert8 = 5400; LowerInput8 = -2015 / 2;  
Lowert9 = 6040; LowerInput9 = 5221 / 2;  
Lowert10 = 6780; LowerInput10 = -3543 / 2;
```

### ▽ Transient Rate Functions

```
qelecL := Module[{n}, Sum[UpperInputn * UnitStep[t[p] - Uppertn],  
  {n, 1, NumberTimeStepsUpper}]];  
qelecH := Module[{n}, Sum[LowerInputn * UnitStep[t[p] - Lowertn],  
  {n, 1, NumberTimeStepsLower}]];]
```

▽ Constant Volumetric Source Terms

*Lower Source Bottom Surface Contribution*

$$S_{\text{elecLower}} := \frac{\frac{2}{3} * q_{\text{elecH}}}{\text{LowerSourceVolume}} ;$$

*Lumped (Side) Lower Source Contribution*

$$S_{\text{elecLumped}} := \frac{\left( \frac{R_{\text{out}} * \frac{1}{3} * q_{\text{elecH}}}{R_{\text{in}} + R_{\text{out}}} \right) + \left( \frac{T_{\text{mean}}}{R_{\text{in}} + R_{\text{out}}} \right)}{\text{LumpedLowerSourceVolume}} ;$$

*Upper Heat Source Contribution*

$$S_{\text{elecUpper}} := \frac{q_{\text{elecL}}}{\text{UpperSourceVolume}} ;$$

*Lower Cooling Jacket Convection*

$$S_{\text{convLower}} := \frac{\left( \frac{T_{\text{mean}}}{R_{\text{in}} + R_{\text{out}}} \right)}{\text{LowerConvectionVolume}} ;$$

*Upper Cooling Jacket Convection*

$$S_{\text{convUpper}} := \frac{\left( \frac{T_{\text{mean}}}{R_{\text{in}} + R_{\text{outUpper}}} \right)}{\text{UpperConvectionVolume}} ;$$

▽ Proportional Volumetric Source Terms

*Lumped (Side) LowerSource Contribution*

$$S_{\text{elecLumped}} := \frac{\left( \frac{1}{R_{\text{in}} + R_{\text{out}}} \right)}{\text{LumpedLowerSourceVolume}} ;$$

*Lower Cooling Jacket Convection*

$$S_{\text{convLower}} := \frac{\left( \frac{1}{R_{\text{in}} + R_{\text{out}}} \right)}{\text{LowerConvectionVolume}} ;$$

*Upper Cooling Jacket Convection*

$$S_{\text{convUpper}} := \frac{\left( \frac{1}{R_{\text{in}} + R_{\text{outUpper}}} \right)}{\text{UpperConvectionVolume}} ;$$

## ▼ Energy Budget

```

GlobalEnergyBudget := Module[{},

BoundarySources[p] =
Sum[ $\frac{k_{2,j} * \Delta Y_j * (T_{2,j,p} - T_{1,j,p}) * \Delta t}{(\Delta x_2 / 2)}$ , {j, 2, jlast1}] +
Sum[ $\frac{k_{i,last1,j} * \Delta Y_j * (T_{i,last1,j,p} - T_{i2,j,p}) * \Delta t}{(\Delta x_{i,last1} / 2)}$ , {j, 2, jlast1}] +
Sum[ $\frac{k_{i,2} * \Delta x_i * (T_{i,2,p} - T_{i,1,p}) * \Delta t}{(\Delta Y_2 / 2)}$ , {i, 2, ilast1}] +
Sum[ $\frac{k_{i,jlast1} * \Delta x_i * (T_{i,jlast1,p} - T_{i,j2,p}) * \Delta t}{(\Delta Y_{jlast1} / 2)}$ , {i, 2, ilast1}];

InternalSourcesSc[p] =
Sum[ $\Delta x_i * \Delta Y_j * \Delta t * SC_{i,j}$ , {j, 2, jlast1}, {i, 2, ilast1}];

InternalSourcesSp[p] =
Sum[ $\Delta x_i * \Delta Y_j * \Delta t * SP_{i,j} * T_{i,j,p}$ , {j, 2, jlast1}, {i, 2, ilast1}];

GlobalDeltaEnergyStorage[p] = Sum[ $\rho_{i,j} * \Delta x_i * \Delta Y_j * Cp_{i,j} * (T_{i,j,p} - T_{i,j,p-1})$ , {j, 2, jlast1}, {i, 2, ilast1}];

NodalEnergyBudget[p] = Table[ $\rho_{i,j} * \Delta x_i * \Delta Y_j * Cp_{i,j} * (T_{i,j,p} - T_{i,j,p-1}) - \Delta x_i * \Delta Y_j * \Delta t * SC_{i,j} + \Delta x_i * \Delta Y_j * \Delta t * SP_{i,j} * T_{i,j,p}$ ,
{j, jlast1, 2, -1}, {i, 2, ilast1}];
];

```

```

TemperatureChange :=
Table[ $\Delta Temperature_{i,j,p} = T_{i,j,p} - T_{i,j,p-1}$ , {j, 1, j2}, {i, 1, i2}];

```

## ▼ Time Step Storage

```

TimeStorage := Module[{},
  Δtimep = Δt;
];

```

---

## Solution Control Parameters

---

### Set Temporal Inputs

#### ▼ Set time-step, Initialize time counter, & Set maximum time count

```
NumberTimeSteps = 550;  
Δtinitial = 40;  
TimeStretch = .2;  
Δt = Δtinitial;  
Δtnew = TimeStretch * Δtinitial;  
Δtime0 = 0;  
  
t[p_] := ∑pp=0p Δtimepp;  
  
tmax = NumberTimeSteps * Δt;
```

#### ▼ Integer times

```
p = 0;  
pmax = NumberTimeSteps;
```

---

### Set Iteration Criteria

#### ▼ Maximum number of iterations

```
iterationp = 0;  
iterationmax = 300;
```

#### ▼ Convergence criteria

```
change = 1.0;  
convergence = 1.0 * 10-4;
```

---

## Initialize Variables

### ▼ Initial condition

```
Tinitial = 300;  
MinTemp = Tinitial;  
MaxTemp = MinTemp;
```

### ▼ Initialize Temperature Array

```
InitializeTemps := Module[{i, j},  
  Table[EvaporantPresenti,j = 2, {j, 1, j2}, {i, 1, i2}];  
  
  Table[EvaporantPresenti,j = 1, {j, Sum[NCVYn, {n, 1, 4}] + 2,  
    UpperEvaporantSurface}, {i, Sum[NCVXm, {m, 1, 2}] + 2, i2}];  
  
  Table[Ti,j,p = Tinitial, {p, 0, 0}, {j, j2, 1, -1}, {i, 1, i2}];  
];
```

---

## Check Evaporant Status

```
SameTemp := Module[{}];  
SetFlags := Module[{},  
  EvaporantPresenti,j = 0;  
  EvaporationTimei,j = t[p];  
];
```

```
EvaporantFlag := Module[{},  
  Do[  
    If[Ti,last1,UpperRadiantSurface,p-1 > 1500, Δt = Δtnew];  
    Which[  
      EvaporantPresenti,j == 1 &&  
      VesselLateralBoundary < i <= i2 &&  
      LowerEvaporantSurface < j <= UpperEvaporantSurface &&  
      Ti,j,p >= TmaxEvap, SetFlags ,  
      True, SameTemp],  
    {j, j2}, {i, i2}];  
];
```

---

## Plot aspect ratio

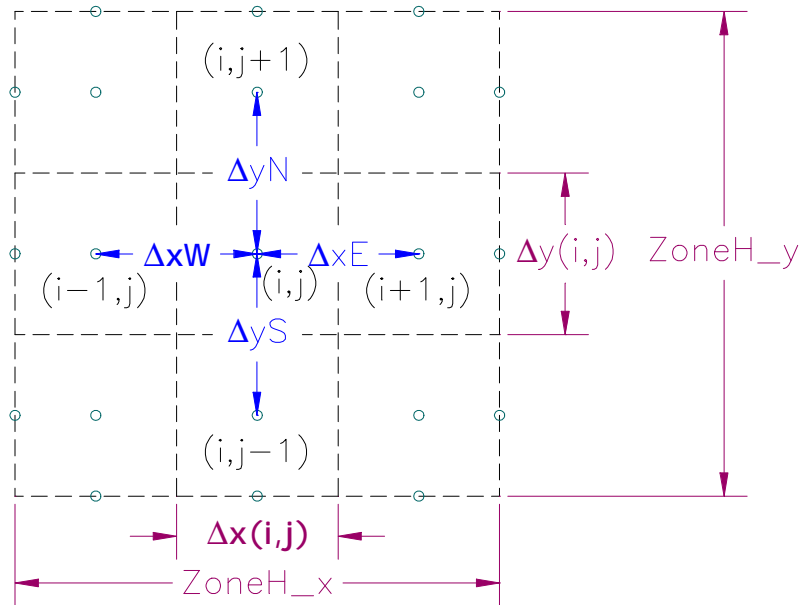
```
Aspect = HH / LL;
```

---

## Zonal Information

---

### General Nodal Schematic



---

## Number of Zones

```
NZx = 11; (*Number of Zones in x-Direction*)
NZy = 8; (*Number of Zones in y-Direction*)
```

---

## Select Property Variation Scenario

*For Property Variations in the x-direction, set PVS=1,*

*For Property Variations in the y-direction, set PVS=2,*

*For Random Property Variations, set PVS=3.*

```
(* PVS=1; *)
PVS = 2;
(* PVS=3; *)
```

---

## Zone Dimensions

### ▼ Zone Widths, x-Direction

```
ZoneWidth1 := VesselEndInsulThk;  
ZoneWidth2 := VesselEndThk;  
ZoneWidth3 := Zone3Width;  
ZoneWidth4 := Zone4Width;  
ZoneWidth5 := Zone5Width;  
ZoneWidth6 := Zone6Width;  
ZoneWidth7 := Zone7Width;  
ZoneWidth8 := Zone8Width;  
ZoneWidth9 := Zone9Width;  
ZoneWidth10 := Zone10Width;  
ZoneWidth11 := Zone11Width;  
ZoneWidth12 := Zone12Width;
```

### ▼ Zone Heights, y-Direction

```
ZoneHeight1 := WaterJacketInsulThk;  
ZoneHeight2 := LowerSourceThickness;  
ZoneHeight3 := LowerSourceVesselInsulThk;  
ZoneHeight4 := VesselBottThk;  
ZoneHeight5 := EvaporantDepth;  
ZoneHeight6 := VesselHeadspace;  
ZoneHeight7 := UpperSourceThickness;  
ZoneHeight8 := UpperSourceInsulThk;
```

### ▼ Overall Length and Height

```
LL = Sum[Lm, {m, 1, NZx}];  
HH = Sum[Hn, {n, 1, NZy}];
```

---

## Number of Control Volumes per Zone

### ▼ Number of Control Volumes in x-Direction by Zone

```
NCVX1 = 2; (*Number of Control Volumes in x-Direction Zone 1*)  
NCVX2 = 2;  
NCVX3 = 4;  
NCVX4 = 4;  
NCVX5 = 3;  
NCVX6 = 3;  
NCVX7 = 3;  
NCVX8 = 3;  
NCVX9 = 3;  
NCVX10 = 3;  
NCVX11 = 3;  
NCVX12 = 3;
```

### ▼ Number of Control Volumes in y-Direction by Zone

```
NCVY1 = 2; (*Number of Control Volumes in y-Direction Zone 1*)  
NCVY2 = 2;  
NCVY3 = 2;  
NCVY4 = 2;  
NCVY5 = 5;  
NCVY6 = 2;  
NCVY7 = 2;  
NCVY8 = 2;
```

---

## Material Boundaries

$$\text{LowerEvaporantSurface} = 1 + \sum_{n=1}^4 \text{NCVY}_n;$$

$$\text{UpperEvaporantSurface} = 1 + \sum_{n=1}^5 \text{NCVY}_n;$$

$$\text{UpperRadiantSurface} = 2 + \sum_{n=1}^6 \text{NCVY}_n;$$

$$\text{LowerRadiantSurface} = 1 + \sum_{n=1}^2 \text{NCVY}_n;$$

$$\text{VesselAbsorptiveSurface} = 2 + \sum_{n=1}^3 \text{NCVY}_n;$$

$$\text{VesselLateralBoundary} = 1 + \sum_{m=1}^2 \text{NCVX}_m;$$

$$\text{LeftThermocouple} = 1 + \sum_{m=1}^5 \text{NCVX}_m;$$

---

## Zonal Property Application

## ▼ Zonal Property Values

```
kzone1[T_] := Insulationk[T];
Cpzone1[T_] := InsulationCp[T];
ρzone1[T_] := Insulationρ[T];

kzone2[T_] := LowerSourcek[T];
Cpzone2[T_] := LowerSourceCp[T];
ρzone2[T_] := LowerSourceρ[T];

kzone3[T_] := Voidk[T];
Cpzone3[T_] := VoidCp[T];
ρzone3[T_] := Voidρ[T];

kzone4[T_] := Vesselk[T];
Cpzone4[T_] := VesselCp[T];
ρzone4[T_] := Vesselρ[T];

kzone5[T_] := Evaporantk[T];
Cpzone5[T_] := EvaporantCp[T];
ρzone5[T_] := Evaporantρ[T];

kzone6[T_] := Voidk[T];
Cpzone6[T_] := VoidCp[T];
ρzone6[T_] := Voidρ[T];

kzone7[T_] := LowerSourcek[T];
Cpzone7[T_] := LowerSourceCp[T];
ρzone7[T_] := LowerSourceρ[T];

kzone8[T_] := Insulationk[T];
Cpzone8[T_] := InsulationCp[T];
ρzone8[T_] := Insulationρ[T];

kzone9[T_] := 1 + (0.0 * T);
Cpzone9[T_] := 10 + (0.0 * T);
ρzone9[T_] := 100 + (0.0 * T);

kzone10[T_] := 2 + (0.0 * T);
Cpzone10[T_] := 10 + (0.0 * T);
ρzone10[T_] := 100 + (0.0 * T);

kzone11[T_] := 3 + (0.0 * T);
Cpzone11[T_] := 10 + (0.0 * T);
ρzone11[T_] := 100 + (0.0 * T);

kzone12[T_] := 4 + (0.0 * T);
Cpzone12[T_] := 10 + (0.0 * T);
ρzone12[T_] := 100 + (0.0 * T);
```

## ▼ Zonal Property Variances

```
PropertyAnomalies := Module[{i, j, m, n},

Do[
  ki,j = Insulationk[Ti,j,p];
  Cpi,j = InsulationCp[Ti,j,p];
  ρi,j = Insulationρ[Ti,j,p];,
  {j, LowerRadiantSurface + 1, UpperRadiantSurface - 1},
  {i, 2, Sum[NCVXm, {m, 1, 1}] + 1}}];

Do[
  ki,j = Vesselk[Ti,j,p];
  Cpi,j = VesselCp[Ti,j,p];
  ρi,j = Vesselρ[Ti,j,p];,
  {j, LowerEvaporantSurface + 1, Sum[NCVYn, {n, 1, 5}] + 1},
  {i, Sum[NCVXm, {m, 1, 1}] + 2, Sum[NCVXm, {m, 1, 2}] + 1}}];

Do[
  ki,j = Insulationk[Ti,j,p];
  Cpi,j = InsulationCp[Ti,j,p];
  ρi,j = Insulationρ[Ti,j,p];,
  {j, Sum[NCVYn, {n, 1, 5}] + 2, UpperRadiantSurface - 1},
  {i, Sum[NCVXm, {m, 1, 1}] + 2, Sum[NCVXm, {m, 1, 2}] + 1}}];

Do[
  ki,j = Insulationk[Ti,j,p];
  Cpi,j = InsulationCp[Ti,j,p];
  ρi,j = Insulationρ[Ti,j,p];,
  {j, LowerRadiantSurface + 1, Sum[NCVYn, {n, 1, 3}] + 1},
  {i, Sum[NCVXm, {m, 1, 1}] + 2, Sum[NCVXm, {m, 1, 2}] + 1}}];

Do[
  ktimei,j,p = ki,j;
  Cptimei,j,p = Cpi,j;
  ρtimei,j,p = ρi,j;,
  {j, 2, jlast1}, {i, 2, ilast1}}];

];
```

# Zonal Source Application

## ▼ Zonal Source Terms

```
Sczone1 := Scconvlower;  
Spzone1 := Spconvlower;  
  
Sczone2 := Sceclelower + Sceleclumped;  
Spzone2 := Speleclumped;  
  
Sczone3 := 0;  
Spzone3 := 0;  
  
Sczone4 := Sceleclumped;  
Spzone4 := Speleclumped;  
  
Sczone5 := 0;  
Spzone5 := 0;  
  
Sczone6 := 0;  
Spzone6 := 0;  
  
Sczone7 := Scelecupper + Scconvupper;  
Spzone7 := Spconvupper;  
  
Sczone8 := Scconvupper;  
Spzone8 := Spconvupper;
```

```
Table[Sczonem, {m, 1, NZy}] // TableForm;
```

```
Table[Spzonem, {m, 1, NZy}] // TableForm;
```

## ▼ Zonal Source Variances

```
SourceAnomalies := Module[{i, j, m, n},  
  Do [  
    Sci,j =  
    Scconvlower;  
    Spi,j =  
    Spconvlower;;  
    {j, 2 +  $\sum_{n=1}^2$  NCVYn, 1 +  $\sum_{n=1}^6$  NCVYn}, {i, 2, 1 +  $\sum_{m=1}^2$  NCVXm}]  
  ];
```

---

# Boundary Conditions

---

## Vertical Boundaries

```
VerticalBoundaries := Module[{i, j},

  Do[
    aE1,j = (k2,j / (Δx2 / 2)); aEi2,j = 0;
    aW1,j = 0; aWi2,j = (kilast1,j / (Δxilast1 / 2));
    aN1,j = 0; aNi2,j = 0;
    aS1,j = 0; aSi2,j = 0;
    a1,j = aE1,j; ai2,j = aWi2,j;
    b1,j = 0; bi2,j = 0;,
    {j, 2, jlast1}];

  Do[
    aE1,j = (k2,j / (Δx2 / 2)); aEi2,j = 0;
    aW1,j = 0; aWi2,j = (kilast1,j / (Δxilast1 / 2));
    aN1,j = 0; aNi2,j = 0;
    aS1,j = 0; aSi2,j = 0;
    a1,j = aE1,j + heffective; ai2,j = aWi2,j;
    b1,j = heffective * Tmean; bi2,j = 0;,
    {j, Sum[NCVYn, {n, 1, 1}] + 2, Sum[NCVYn, {n, 1, 2}] + 1}];

  Do[
    aE1,j = (k2,j / (Δx2 / 2)); aEi2,j = 0;
    aW1,j = 0; aWi2,j = (kilast1,j / (Δxilast1 / 2));
    aN1,j = 0; aNi2,j = 0;
    aS1,j = 0; aSi2,j = 0;
    a1,j = aE1,j + heffective; ai2,j = aWi2,j;
    b1,j = heffective * Tmean; bi2,j = 0;,
    {j, Sum[NCVYn, {n, 1, 6}] + 2, Sum[NCVYn, {n, 1, 7}] + 1}];

];
```

## Horizontal Boundaries

```
HorizontalBoundaries := Module[{i, j},

Do[
  aNi,1 = (ki,2 / (ΔY2 / 2)); aNi,j2 = 0;
  aSi,1 = 0; aSi,j2 = (ki,jlast1 / (ΔYjlast1 / 2));
  aEi,1 = 0; aEi,j2 = 0;
  aWi,1 = 0; aWi,j2 = 0;
  ai,1 = aNi,1 + heffective; ai,j2 = aSi,j2 + heffective;
  bi,1 = heffective * Tmean; bi,j2 = heffective * Tmean;;
  {i, 2, Sum[NCVXm, {m, 1, 2}] + 1}];

Do[
  aNi,1 = (ki,2 / (ΔY2 / 2)); aNi,j2 = 0.0;
  aSi,1 = 0; aSi,j2 = (ki,jlast1 / (ΔYjlast1 / 2));
  aEi,1 = 0; aEi,j2 = 0;
  aWi,1 = 0; aWi,j2 = 0;
  ai,1 = aNi,1 + heffective; ai,j2 = aSi,j2 + hradiation[Ti,j2,p];
  bi,1 = heffective * Tmean; bi,j2 = hradiation[Ti,j2,p] * Tsurr;;
  {i, Sum[NCVXm, {m, 1, 2}] + 2, ilast1}];
];
```

Program Kernel -- No User  
Interaction

---

## Generate Grid

---

### Nodal Index Limits

```
ilast = Sum[NCVXm, {m, 1, NZx}];  
jlast = Sum[NCVYn, {n, 1, NZy}];  
ilast1 = ilast + 1;  
jlast1 = jlast + 1;  
i2 = ilast1 + 1;  
j2 = jlast1 + 1;
```

```
TableForm[{ilast1, jlast1, i2, j2}, TableHeadings ->  
{"ilast1 =", "jlast1 =", "i2 =", "j2 ="}]
```

---

### Generate $x$ -Grid

```
Clear[ΔxZone, Δx]
```

```
Table[ΔxZonexZone = (LxZone / NCVXxZone), {xZone, 1, NZx}] // TableForm;  
Δx1 = 0; Δxi2 = 0;
```

```
start := 2;  
Do[  
  stop = Sum[NCVXm, {m, 1, xZone}] + 1;  
  Do[Δxi = ΔxZonexZone, {i, start, stop}];  
  start = stop + 1;  
  , {xZone, 1, NZx}];
```

```
x1 = 0;  
Table[xi = xi-1 +  $\left(\frac{\Delta x_{i-1} + \Delta x_i}{2}\right)$ , {i, 2, i2}];
```

```
TableForm[Table[{i, Δxi, xi, (xi / 0.0254)}, {i, 1, i2}],  
TableHeadings -> {None, {"i", "Δxi", "xi (m)", "xi (in)"}]}
```

---

## Generate y-Grid

```
Clear[ΔyZone, Δy]
```

```
Table[ΔyZone_yZone = (HyZone / NCVY_yZone), {yZone, 1, NZy}];  
Δy1 = 0; Δy_j2 = 0;
```

```
start := 2;  
Do[  
  stop = Sum[NCVY_n, {n, 1, yZone}] + 1;  
  Do[Δy_j = ΔyZone_yZone, {j, start, stop}];  
  start = stop + 1;  
  , {yZone, 1, NZy}];
```

```
y1 = 0;  
Table[y_j = y_{j-1} +  $\left(\frac{\Delta y_{j-1} + \Delta y_j}{2}\right)$ , {j, 2, j2}];
```

```
TableForm[Table[{j, Δy_j, y_j, (y_j / 0.0254)}, {j, 1, j2}],  
TableHeadings -> {None, {"j", "Δy_j", "y_j (m)", "y_j (in)"}}]
```

---

## Assign Properties to Nodes

---

### Initialize Temperature Array

```
InitializeTemps;
```

## X-Variant Property Assignment Structure

```
xProperties :=
Module[{i, j, Zone, m, start, stop},
start = 2;
Do[stop = Sum[NCVXm, {m, 1, Zone}] + 1;
Do[
ki,j = kzonezone[Ti,j,p];
Cpi,j = Cpzonezone[Ti,j,p];
ρi,j = ρzonezone[Ti,j,p];
SCi,j = Sczonezone;
Spi,j = Spzonezone;
{i, start, stop}, {j, 2, jlast1}];
start = stop + 1;,
{Zone, 1, NZx}];
];
```

## Y-Variant Property Assignment Structure

```
yProperties :=
Module[{i, j, Zone, n, start, stop},
start = 2;
Do[stop = Sum[NCVYn, {n, 1, Zone}] + 1;
Do[
ki,j = kzonezone[Ti,j,p];
Cpi,j = Cpzonezone[Ti,j,p];
ρi,j = ρzonezone[Ti,j,p];
SCi,j = Sczonezone;
Spi,j = Spzonezone;
, {j, start, stop}, {i, 2, ilast1}];
start = stop + 1;,
{Zone, 1, NZy}];
];
```

## Apply Zonal Properties to Individual Nodes

```
Properties := Module[{i, j},
  Which[
    PVS == 1, xProperties,
    PVS == 2, yProperties,
    PVS == 3, SetPropertyByNode,
    True, "Invalid PVS Entry"
  ];
  PropertyAnomalies;
  SourceAnomalies;
  InternalRadiation;
];
```

## Graphical Property Values

```
Properties;
```

```
TableForm[Table[ki,j, {j, j2, 1, -1}, {i, 1, i2}]]
```

```
kvalue = Transpose[Table[ki,j, {i, 2, ilast1}, {j, 2, jlast1}]];
ContourGraph =
  ListContourPlot[
    kvalue, AspectRatio → Aspect, Contours → 50, ColorFunction → Hue,
    ContourLines → False, PlotLabel -> "Conductivity";
```

```
TableForm[Table[Cpi,j, {j, j2, 1, -1}, {i, 1, i2}]]
```

```
Cpvalue = Transpose[Table[Cpi,j, {i, 2, ilast1}, {j, 2, jlast1}]];
ContourGraph =
  ListContourPlot[
    Cpvalue, AspectRatio → Aspect, Contours → 50, ColorFunction → Hue,
    ContourLines → False, PlotLabel -> "Specific Heat";
```

```
TableForm[Table[ρi,j, {j, j2, 1, -1}, {i, 1, i2}]]
```

```
ρvalue = Transpose[Table[ρi,j, {i, 2, ilast1}, {j, 2, jlast1}]];
ContourGraph =
  ListContourPlot[ρvalue, AspectRatio → Aspect, Contours → 50,
    ColorFunction → Hue, ContourLines → False, PlotLabel -> "Density";
```

---

## Discretization Coefficients

---

### Time Independent Coefficients

```
TimeIndependentCoefficients :=  
Module[{i, j},  
  Table[aEi,j = aWi+1,j = Δyj *  $\frac{2 * k_{i,j} * k_{i+1,j}}{\Delta x_i * k_{i+1,j} + \Delta x_{i+1} * k_{i,j}}$ ,  
    {j, 1, j2}, {i, 1, ilast1}];  
  
  Table[aNi,j = aSi,j+1 = Δxi *  $\frac{2 * k_{i,j} * k_{i,j+1}}{\Delta y_j * k_{i,j+1} + \Delta y_{j+1} * k_{i,j}}$ ,  
    {j, 1, jlast1}, {i, 1, i2}];  
];
```

---

### Initialize Boundary Conditions

```
VerticalBoundaries;  
HorizontalBoundaries;
```

---

### Update Time and Temperature Dependent Coefficients

#### ▼ Matrix Coefficients

```
MatrixValues :=  
Module[{i, j},  
  TimeIndependentCoefficients;  
  Do[  
    aOi,j = (ρi,j * Cpi,j * Δxi * Δyj) / Δt;  
    ai,j = aOi,j + aEi,j + aWi,j + aNi,j + aSi,j + (Spi,j * Δxi * Δyj);  
    bi,j = (Sci,j * Δxi * Δyj) + (aOi,j * Ti,j,p-1);  
    {j, 2, jlast1}, {i, 2, ilast1}];  
];
```

## ▼ Update Function

```
UpdateValues := Module[{i, j},  
  Properties;  
  MatrixValues;  
  VerticalBoundaries;  
  HorizontalBoundaries];  
  
UpdateValues;
```

---

## Solution Methodology

## Iterate for Temperatures

```

IterativeSolver :=
While[(iteration_p < iterationmax && change > convergence),

  (* Save temperatures from last iteration *)

  Table[Tlasti,j = Ti,j,p, {j, 1, j2}, {i, 1, i2}];
  iteration_p = iteration_p + 1;

  (* Sweep "up" in x *)

  Do[
    SubDiag = Table[-aSi,j, {j, 2, j2}];
    Diagonal = Table[ai,j, {j, 1, j2}];
    SuperDiag = Table[-aNi,j, {j, 1, jlast1}];
    Known = Table[bi,j + aEi,jTi+1,j,p + aWi,jTi-1,j,p, {j, 1, j2}];
    Tempvector = TridiagonalSolve[SubDiag, Diagonal, SuperDiag, Known];
    Table[Ti,j,p = Tempvector[[j]], {j, 1, j2},
      {i, 2, ilast1}];

  (* Sweep "up" in y *)

  Do[
    SubDiag = Table[-aWi,j, {i, 2, i2}];
    Diagonal = Table[ai,j, {i, 1, i2}];
    SuperDiag = Table[-aEi,j, {i, 1, ilast1}];
    Known = Table[bi,j + aNi,jTi,j+1,p + aSi,jTi,j-1,p, {i, 1, i2}];
    Tempvector = TridiagonalSolve[SubDiag, Diagonal, SuperDiag, Known];
    Table[Ti,j,p = Tempvector[[i]], {i, 1, i2},
      {j, 2, jlast1}];

  (* Sweep "down" in x *)

  Do[
    SubDiag = Table[-aSi,j, {j, 2, j2}];
    Diagonal = Table[ai,j, {j, 1, j2}];
    SuperDiag = Table[-aNi,j, {j, 1, jlast1}];
    Known = Table[bi,j + aEi,jTi+1,j,p + aWi,jTi-1,j,p, {j, 1, j2}];
    Tempvector = TridiagonalSolve[SubDiag, Diagonal, SuperDiag, Known];
    Table[Ti,j,p = Tempvector[[j]], {j, 1, j2},
      {i, ilast1, 2, -1}];

  (* Sweep "down" in y *)

  Do[
    SubDiag = Table[-aWi,j, {i, 2, i2}];
    Diagonal = Table[ai,j, {i, 1, i2}];
    SuperDiag = Table[-aEi,j, {i, 1, ilast1}];
    Known = Table[bi,j + aNi,jTi,j+1,p + aSi,jTi,j-1,p, {i, 1, i2}];
    Tempvector = TridiagonalSolve[SubDiag, Diagonal, SuperDiag, Known];
    Table[Ti,j,p = Tempvector[[i]], {i, 1, i2},
      {j, jlast1, 2, -1}];

    (* Compute relative error *)
    AverageChange = Sum[Abs[Ti,j,p - Tlasti,j], {j, 1, j2}, {i, 1, i2}] / ((i2) (j2));
    AverageTemp = Sum[Ti,j,p, {j, 1, j2}, {i, 1, i2}] / ((i2) (j2));
    change =  $\frac{\text{AverageChange}}{\text{AverageTemp}}$ ;

    increment_p = change;
  ];

```

---

## March Through Time

```
While[p < pmax && MaxTemp < PropertyLimit,  
  
  p = p + 1;  
  TimeStorage;  
  Table[Ti,j,p = Ti,j,p-1, {j, 1, j2}, {i, 1, i2}];  
  UpdateValues;  
  
  change = convergence + 1;  
  iterationp = 0;  
  
  IterativeSolver;  
  EvaporantFlag;  
  
  MinTemp = Min[Table[Ti,j,p, {j, 2, jlast1}, {i, 2, ilast1}]];  
  MaxTemp = Max[Table[Ti,j,p, {j, 2, jlast1}, {i, 2, ilast1}]];  
  MeanEvapTemp;  
  
  transience = Max[Table[differencei,j = Abs[Ti,j,p - Ti,j,p-1],  
    {j, 2, jlast1}, {i, 2, ilast1}]];  
  GlobalEnergyBudget;  
  
];
```

---

## Assign Corner Temperatures

```
T1,1,p = ((T1,2,p + T2,1,p) / 2);  
T1,j2,p = ((T1,jlast1,p + T2,j2,p) / 2);  
Ti2,1,p = ((Ti2,2,p + Tilast1,1,p) / 2);  
Ti2,j2,p = ((Tilast1,j2,p + Ti2,jlast1,p) / 2);
```

```
TableForm[{T1,1,p, T1,j2,p, Ti2,1,p, Ti2,j2,p}, TableHeadings ->  
  {"Lower Left Corner Temp =", "Upper Left Corner Temp =",  
   "Lower Right Corner Temp =", "Upper Right Corner Temp ="}]
```

---

## Computational Information

```
ComputationTime = TimeUsed[] - StartTime;  
plast = p;
```

# Output Tabular and Graphical Results

## Tabular Results

### Reset Void Temperatures for Output

```
PercentageError[p_] :=  
  ((GlobalΔEnergyStorage[p] - InternalSourcesSc[p] +  
    BoundarySources[p] + InternalSourcesSp[p]) /  
    InternalSourcesSc[p]) *  
  100;
```

```
ResetVoids := Module[{},  
  Table[Ti,j,plast = 0,  
    {j, LowerRadiantSurface + 1, VesselAbsorptiveSurface - 1},  
    {i, VesselLateralBoundary + 1, i2}];  
  Table[Ti,j,plast = 0, {j, UpperEvaporantSurface + 1,  
    UpperRadiantSurface - 1}, {i, VesselLateralBoundary + 1, i2}];  
  Table[ If[EvaporantPresenti,j == 0, Ti,j,plast = 0, SameTemp],  
    {j, LowerEvaporantSurface, UpperEvaporantSurface},  
    {i, VesselLateralBoundary + 1, i2}];  
];
```

### Summary of Solution Data

```
TableForm[{{i2 * j2, Δtime1, Δtimeplast, plast, t[p],  
  transience, MaxTemp, MinTemp, MeanEvapTemp, iterationp,  
  convergence, change, ComputationTime}, TableHeadings ->  
  {"Number of Nodes      =", "Initial Time Step      =",  
    "Final Time Step      =", "Number of Time Steps =",  
    "Total Time (s)       =", "Transience          =",  
    "Maximum Temp         =", "Minimum Temp         =",  
    "Mean Evaporant Temp  =", "Iterations Last Time =",  
    "Conv. Criteria        =", "Convergence Test     =",  
    "Computation Time     ="}]}
```

## Iteration Table

```
TableForm[Table[
  {p, t[p], iterationp, incrementp}, {p, 0, plast}], TableHeadings ->
  {None, {"Time Step", "Time(s)", "# Iterations", "Change"}}]
```

## Evaporant Status

```
TableForm[Table[EvaporationTimei,j,
  {j, UpperEvaporantSurface, LowerEvaporantSurface + 1, -1},
  {i, VesselLateralBoundary + 1, i2}]]
```

```
Table[EvaporantPresenti,j, {j, j2, 1, -1}, {i, 1, i2}] // MatrixForm
```

## Energy Budget

### ▼ Tabular Data

```
TableForm[Table[{p, t[p], Δtimep, GlobalΔEnergyStorage[p],
  InternalSourcesSc[p], InternalSourcesSp[p], BoundarySources[p],
  GlobalΔEnergyStorage[p] - InternalSourcesSc[p] +
  BoundarySources[p] + InternalSourcesSp[p],
  PercentageError[p]}, {p, 1, plast}],
  TableHeadings -> {None, {"p", "Time(s)", "Time Step (s)",
  "ΔEst", "Sc", "Sp", "Boundary", "Balance", "Error (%)"}]}
```

### ▼ Energy Budget Plot

```
list1 = Table[{t[p], GlobalΔEnergyStorage[p]}, {p, 1, plast}];
list2 = Table[{t[p], -InternalSourcesSc[p]}, {p, 1, plast}];
list3 = Table[{t[p], InternalSourcesSp[p]}, {p, 1, plast}];
list4 = Table[{t[p], BoundarySources[p]}, {p, 1, plast}];
```

```
MultipleListPlot[list1, list2, list3, list4, PlotLegend ->
  {"ΔE Storage", "Sc*Δt*V", "Sp*T*Δt*V", "Boundaries"},
  Background -> GrayLevel[0.9999], PlotJoined -> True]
```

---

## Tabular Temperature Distribution

```
VoidTemps;
```

```
TemperatureTable[p_] :=  
  TableForm[Table[Ti,j,p, {j, j2, 1, -1}, {i, 1, i2}]]
```

```
TemperatureTable[0]
```

```
TemperatureTable[plast - 1]
```

```
TemperatureTable[plast]
```

---

## Graphical Results

---

### Graphical Plot Data Tables

```
data = Transpose[Table[Ti,j,p, {i, 1, i2}, {j, 1, j2}]];
```

```
TableForm[data[plast]];
```

---

### Temperature Distribution History

```
TempXlist[p_] := Table[{i, Ti,UpperRadiantSurface,p}, {i, 2, ilast1}]
```

```
MultipleListPlot[TempXlist[0], TempXlist[5],  
  TempXlist[10], TempXlist[15], TempXlist[20], TempXlist[30],  
  TempXlist[40], TempXlist[60], TempXlist[80], TempXlist[100],  
  TempXlist[140], TempXlist[180], TempXlist[220], TempXlist[260],  
  TempXlist[300], PlotLegend -> {"p=0", "p=5", "p=10", "p=15",  
  "p=20", "p=30", "p=40", "p=60", "p=80", "p=100",  
  "p=140", "p=180", "p=220", "p=260", "p=300"},  
  Background -> GrayLevel[0.9999], PlotJoined -> True];
```

---

## Thermal Contour Plot

```
ListContourPlot[data, AspectRatio → Aspect, Contours → 300,  
ColorFunction → (Hue[.75 (1 - #)]&), ContourLines → False,  
PlotLabel -> StyleForm["Spatial Temperature Distribution",  
FontFamily → Times, FontSize → 16]]];
```

---

## Evaporant Contour Plot

```
Evaporantdata = Table[EvaporantPresenti,j, {j, 1, j2}, {i, 1, i2}];
```

```
ListContourPlot[Evaporantdata, AspectRatio → Aspect, Contours → 2,  
ColorFunction → (Hue[0.75 (1 - #)]&), ContourLines → False,  
PlotLabel -> StyleForm["Spatial Evaporant Distribution",  
FontFamily → Times, FontSize → 16]]];
```

---

## Power Input Functions

### ▼ *Upper Source Power Input Function*

```
ListPlot[Table[{t[p], qelecL}, {p, 0, plast}], PlotJoined -> True,  
Frame -> True, Background -> GrayLevel[0.9999]]
```

### ▼ *Lower Source Power Input Function*

```
ListPlot[Table[{t[p], qelecH}, {p, 0, plast}], PlotJoined -> True,  
Frame -> True, Background -> GrayLevel[0.9999]]
```

```
Table[{t[p], qelecH}, {p, 0, plast}] // TableForm;
```

---

## Transient Response, Left Temperatures

### ▼ Lower Source, Left Temperature

```
ListPlot[Table[{t[p], TLeftThermocouple, LowerRadiantSurface, p},  
  {p, 0, plast}], PlotRange -> All,  
  PlotJoined -> True, Frame -> True, Background -> GrayLevel[0.9999]]
```

### ▼ Material Container, Left Temperature

```
ListPlot[  
  Table[{t[p], TLeftThermocouple, Sum[NCVYn, {n, 1, 3}] + 2, p}, {p, 0, plast}],  
  PlotJoined -> True, Frame -> True, Background -> GrayLevel[0.9999]]
```

### ▼ Upper Source, Left Temperature

```
ListPlot[  
  Table[{t[p], TLeftThermocouple, Sum[NCVYn, {n, 1, 6}] + 2, p}, {p, 0, plast}],  
  PlotJoined -> True, Frame -> True, Background -> GrayLevel[0.9999]]
```

---

## Transient Response, Center Temperatures

### ▼ Upper Source, Center Temperature

```
ListPlot[Table[{t[p], Tilast1, UpperRadiantSurface, p}, {p, 0, plast}],  
  PlotJoined -> True, Frame -> True, Background -> GrayLevel[0.9999]]
```

```
ListPlot[Table[{t[p], Tilast1, UpperRadiantSurface, p}, {p, 100, plast}],  
  PlotJoined -> True, Frame -> True, Background -> GrayLevel[0.9999]]
```

```
(* TableForm[  
  Table[{t[p], Tilast1, UpperRadiantSurface, p}, {p, 40, plast-50}]] *)
```

### ▼ Material Container, Center Temperature

```
ListPlot[Table[{t[p], Tilast1, LowerEvaporantSurface, p}, {p, 0, plast}],  
  PlotJoined -> True, Frame -> True, Background -> GrayLevel[0.9999]]
```

### ▼ Lower Source, Center Temperature

```
ListPlot[Table[{t[p], Ti2, Sum[NCVYn, {n, 1, 2}] + 1, p}, {p, 0, plast}],  
  PlotJoined -> True, Frame -> True, Background -> GrayLevel[.9999]]
```

# Temperature Distribution Along Section Through Center-Line

## ▼ Material Vessel Lower Surface

```
ListPlot[Table[{xi / 0.0254, Ti,sum[NCVYm, {m,1,4}], p}], {i, 1, i2}],  
Frame -> True, Background -> GrayLevel[0.9999], PlotJoined -> True]
```

## ▼ Lower Source Upper Surface

```
ListPlot[Table[{xi / 0.0254, Ti,sum[NCVYm, {m,1,2}], p}], {i, 1, i2}],  
PlotJoined -> True, Frame -> True, Background -> GrayLevel[0.9999]]
```

## ▼ Upper Source Lower Surface

```
ListPlot[Table[{xi / 0.0254, Ti,sum[NCVYm, {m,1,7}]+1, p}], {i, 1, i2}],  
PlotJoined -> True, Background -> GrayLevel[0.9999]]
```

## ▼ Material Surface

```
ListPlot[Table[{xi / 0.0254, Ti,sum[NCVYm, {m,1,5}]+1, p}], {i, 1, i2}],  
PlotJoined -> True, Frame -> True, Background -> GrayLevel[0.9999]]
```

---

## Surface Plot

```
SurfacePlot[p_] :=  
ListSurfacePlot3D[  
  Table[{xi, yj, Ti,j,p}, {i, 1, i2}, {j, 1, j2}],  
  BoxRatios -> {LL, HH, (LL + HH) / 4},  
  PlotRange -> {MinTemp - 1, MaxTemp + 1},  
  ColorFunction -> (Hue[0.75 (1 - #)]&),  
  Axes -> True,  
  AxesLabel -> {  
    StyleForm["x", FontFamily -> Times, FontSize -> 16] ,  
    StyleForm[" y", FontFamily -> Times, FontSize -> 16],  
    StyleForm[  
      "    T(x,y,t) Kelvin ", FontFamily -> Times, FontSize -> 16] }  
  ]
```

```
SurfacePlot[plast]
```

```
(* Animate[SurfacePlot[pp], {pp, 0, 100, 10}]; *)
```

---

## Conductivity vs. Time

### ▼ Define Plots

```
LowerSourcekHistory := ListPlot[  
  Table[{t[p], ktimeilast1, Sum[NCVYn, {n, 1, 2}]+1, p}, {p, 0, plast}],  
  PlotJoined -> True, Frame -> True, Background -> GrayLevel[0.9999],  
  PlotLabel -> "LowerSource Conductivity History";
```

```
InsulationkHistory :=  
ListPlot[Table[{t[p], ktimeilast1, Sum[NCVYn, {n, 1, 1}], p}, {p, 0, plast}],  
PlotJoined -> True, Frame -> True, Background -> GrayLevel[0.9999],  
PlotLabel -> "Insulation Conductivity History";
```

## ▼ Graphical Histories

```
GraphicsArray[{LowerSourcekHistory, InsulationkHistory}]
```

## Specific Heat vs. Time

```
ListPlot[Table[{t[p],  
  CptimeVesselLateralBoundary+1,UpperEvaporantSurface,p}, {p, 0, plast}],  
PlotJoined -> True, Frame -> True, Background -> GrayLevel[0.9999]]
```

## Density vs. Time

```
ListPlot[Table[{t[p], ρtime5,5,p}, {p, 0, plast}],  
PlotJoined -> True, Frame -> True, Background -> GrayLevel[0.9999]]
```

## Export Data

### Define Output Function (Taken from Wolfram Research FAQ Web Site)

```
Options[WriteMatrix] =  
{ColumnSeparator -> "\t", FormatType -> Identity};
```

```
WriteMatrix[filename_String, data_List, opts___] :=  
Block[{myfile, op, colsep, ff}, myfile = OpenWrite[filename];  
  colsep = ColumnSeparator /. {opts} /. Options[WriteMatrix];  
  ff = FormatType /. {opts} /. Options[WriteMatrix];  
  Scan[(WriteString[myfile, ff[First[#1]]];  
    Scan[WriteString[myfile, colsep, ff[#1]]&, Rest[#1]];  
    WriteString[myfile, "\n"]&, data];  
  Close[myfile]]
```

---

## Center-Line Section Axial Temperature Profiles

```
AxialUpper = Table[{xi / 0.0254, Ti,UpperRadiantSurface,p}, {i, 1, i2}];
AxialLower = Table[{xi / 0.0254, Ti,LowerRadiantSurface,p}, {i, 1, i2}];
AxialVesselBottom =
  Table[{xi / 0.0254, Ti,VesselAbsorptiveSurface,p}, {i, 1, i2}];
AxialMatlSurface =
  Table[{xi / 0.0254, Ti,UpperEvaporantSurface,p}, {i, 1, i2}];

WriteMatrix["AxialUpper.txt", AxialUpper];
WriteMatrix["AxialLower.txt", AxialLower];
WriteMatrix["AxialVesselBottom.txt", AxialVesselBottom];
WriteMatrix["AxialMatlSurface.txt", AxialMatlSurface];
```

---

## Transient Response, Various Locations Corresponding to Empirical Data Acquisition Points

```
TransLowerLeft =
  Table[{t[p], TLeftThermocouple,LowerRadiantSurface,p}, {p, 0, plast}];
TransVesselLeft =
  Table[{t[p], TLeftThermocouple,VesselAbsorptiveSurface,p}, {p, 0, plast}];
TransUpperLeft =
  Table[{t[p], TLeftThermocouple,UpperRadiantSurface,p}, {p, 0, plast}];
TransLowerCenter = Table[{t[p], Ti2,LowerRadiantSurface,p}, {p, 0, p}];
TransVesselCenter =
  Table[{t[p], Ti2,VesselAbsorptiveSurface,p}, {p, 0, plast}];
TransUpperCenter =
  Table[{t[p], Ti2,UpperRadiantSurface,p}, {p, 0, plast}];

WriteMatrix["TransLowerLeft.txt", TransLowerLeft];
WriteMatrix["TransVesselLeft.txt", TransVesselLeft];
WriteMatrix["TransUpperLeft.txt", TransUpperLeft];
WriteMatrix["TransLowerCenter.txt", TransLowerCenter];
WriteMatrix["TransVesselCenter.txt", TransVesselCenter];
WriteMatrix["TransUpperCenter.txt", TransUpperCenter];
```

---

## Power Input Functions

### ▼ Upper Source, Power Input Function (Transient)

```
UpperPwrInput = Table[{t[p], qelecL}, {p, 0, plast}];  
  
WriteMatrix["UpperPwrInput.txt", UpperPwrInput];
```

### ▼ Lower Source, Power Input Function (Transient)

```
LowerPwrInput = Table[{t[p], qelecH}, {p, 0, plast}];  
  
WriteMatrix["LowerPwrInput.txt", LowerPwrInput];
```

# Compute Stability Criteria

```

ComputeStabilityCriteria :=
Module[ {},
  Tstability = Tilast1-1,UpperRadiantSurface,p;
  Tcriteria = Tilast1-1,UpperRadiantSurface,p-1;
  ΔxE =  $\frac{\Delta x_{ilast1-1} + \Delta x_{ilast1}}{2}$ ;
  ΔxW =  $\frac{\Delta x_{ilast1-1} + \Delta x_{ilast1-2}}{2}$ ;
  ΔyN =  $\frac{\Delta y_{UpperRadiantSurface} + \Delta y_{UpperRadiantSurface+1}}{2}$ ;
  R1 = (CrucibleEndThk *
    0.0254 / (Cruciblek[Tstability] * Δxilast1-1 * ΔyUpperRadiantSurface));
  R2 = (CrucLidInsulThk *
    0.0254 / (Salik[Tstability] * Δxilast1-1 * ΔyUpperRadiantSurface)) +
    (1 / (2 * heffective * Δxilast1-1 * ΔyUpperRadiantSurface));
  Capacity = ρilast1-1,UpperRadiantSurface * Δxilast1-1 *
    ΔyUpperRadiantSurface * CPilast1-1,UpperRadiantSurface;
  ConductanceE =
    (2 * kilast1-1,UpperRadiantSurface * kilast1-1+1,UpperRadiantSurface) /
    (  $\frac{\Delta x_{ilast1-1}}{\Delta x_E} * k_{ilast1-1+1,UpperRadiantSurface} +$ 
       $\frac{\Delta x_{ilast1-1+1}}{\Delta x_E} * k_{ilast1-1,UpperRadiantSurface}$  );
  ConductanceW =
    (2 * kilast1-1,UpperRadiantSurface * kilast1-1-1,UpperRadiantSurface) /
    (  $\frac{\Delta x_{ilast1-1}}{\Delta x_W} * k_{ilast1-1-1,UpperRadiantSurface} +$ 
       $\frac{\Delta x_{ilast1-1-1}}{\Delta x_W} * k_{ilast1-1,UpperRadiantSurface}$  );
  ConductanceN =
    (2 * kilast1-1,UpperRadiantSurface * kilast1-1,UpperRadiantSurface+1) /
    (  $\frac{\Delta y_{UpperRadiantSurface}}{\Delta y_N} * k_{ilast1-1,UpperRadiantSurface+1} +$ 
       $\frac{\Delta y_{UpperRadiantSurface+1}}{\Delta y_N} * k_{ilast1-1,UpperRadiantSurface}$  );
  TimeStepMax = Capacity / ( (  $\frac{1}{R1 + R2}$  ) + σ * F * Δxilast1-1 * Tcriteria3 +
    ConductanceE + ConductanceW + ConductanceN )
];

```

ComputeStabilityCriteria

# Appendix I

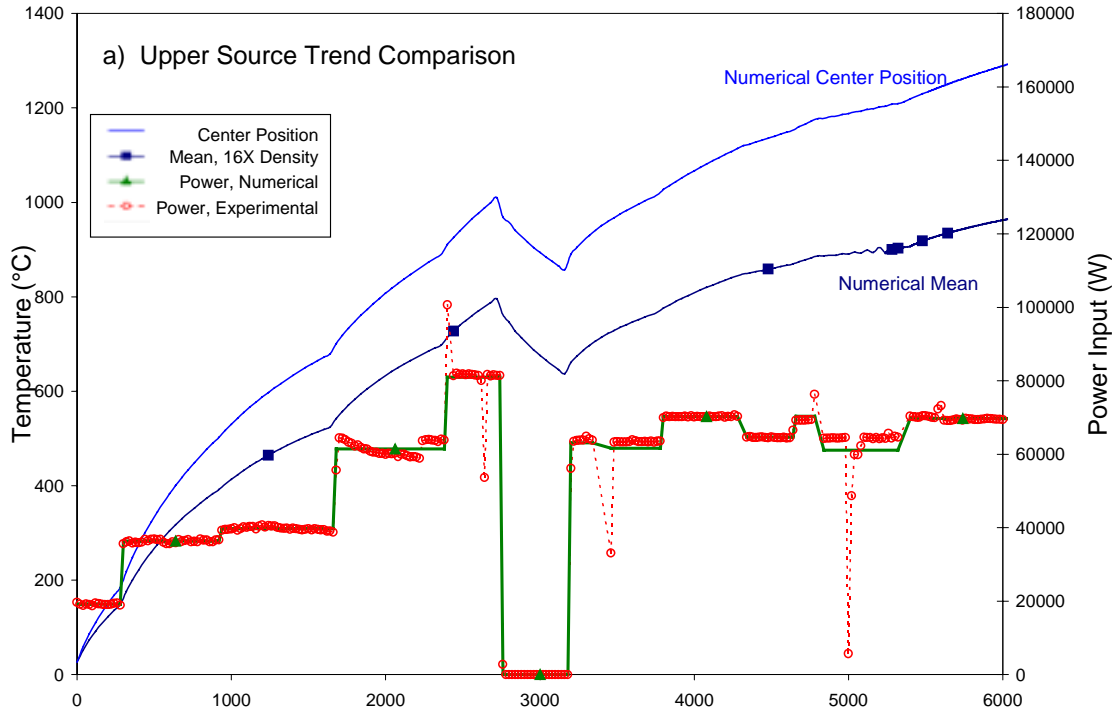
## Mean Temperature and 16X Density

### Transient Responses

Panel a) of Figure I1 illustrates the transient mean-temperature response of the upper heat source subject to the input of Data Set II. The purpose for this inclusion is the illustration of the uniformity in response trend between the point temperature response of *Transient Response, Data Set II, Center Position, Upper Source* and a representative average response.

Note also, panel b) depicting the numerical 16X grid density response compared the experimental response of Data Set II.

Transient Response: Data Set II,  
Center Position and Mean



Transient Response: Data Set II, Center Position

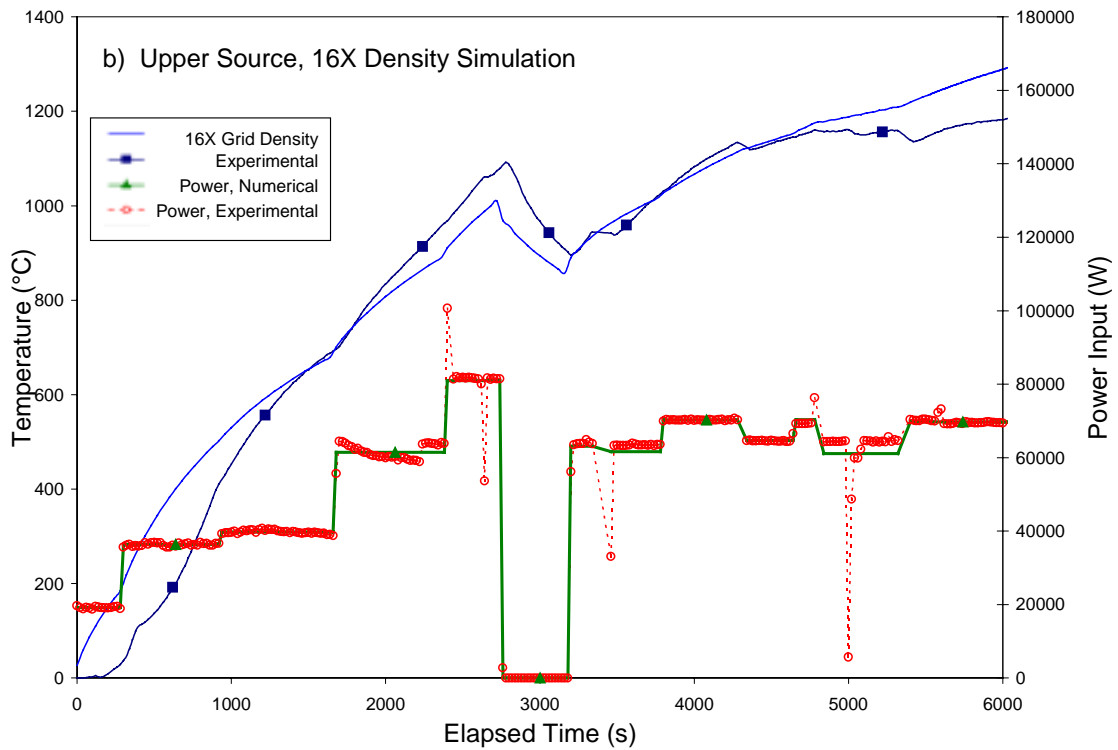


Figure II Mean and 16X Grid Density Transient Responses

# Vita

## Brian Vincent Nutter

Life began, for the author of this work, on 12 May 1972, in Henrico, Virginia. In his first year, his parents moved their home to Powhatan, Virginia, where they presently reside. It was here that the author spent his formative years. An old-fashioned upbringing afforded the strong moral and ethical traits that he cherishes today. Numerous toys, clocks, gadgets and bicycles were sacrificed in the thirst for mechanical knowledge.

Graduating from Powhatan High School in 1990, the author moved on to Virginia Tech to pursue a degree in mechanical engineering. In Blacksburg, he would attend the state's premier engineering program, while enjoying the beautiful experiences of the surrounding mountains. Upon graduation in 1994, the author began his graduate study in mechanical engineering at Virginia Tech. Following the completion of his course work, in light of unavailable research funding, in 1995 he left Virginia Tech and his graduate studies to find work as a mechanical engineer.

Not long thereafter, he began employment as Mechanical Engineer for his current employer. Over time, the opportunity for the research detailed in the preceding work arose. Still lacking the research and thesis portion of his Master's degree requirements, he obtained permission to conduct the foregoing investigation.

The author defended this work on 8 December 2000. Following, this defense, he plans to spend time recouping numerous lost hours of quality-time with his lovely wife of three years. Having received approval to take the Principles and Practice of Engineering exam, the author hopes to soon obtain his license as a professional engineer in the state of Virginia.

---

Brian V. Nutter